Fluidization and fluctuations in granular systems

Nichol, K.M.

Citation
Nichol, K. M. (2011, October 4). *Fluidization and fluctuations in granular systems*. *Casimir PhD Series*. Retrieved from https://hdl.handle.net/1887/17889

Version:	Not Applicable (or Unknown)
License:	Leiden University Non-exclusive license
Downloaded from:	https://hdl.handle.net/1887/17889

Note: To cite this publication please use the final published version (if applicable).

Fluidization and Fluctuations in Granular Systems

PROEFSCHRIFT

Ter verkrijging van
de graad van Doctor aan de Universiteit Leiden,
op gezag van de Rector Magnificus
Prof. mr. P.F. van der Heijden,
volgens besluit van het College voor Promoties
te verdedigen op 4 oktober 2011
klokke 13.45 uur
door

Kiri Nichol
geboren te Calgary
in 1981

Promotiecommissie:

Promotor:	Prof. dr. M.L. van Hecke
Overige leden:	Prof. dr. E. Eliel
	Dr. Karen Daniels (*North Carolina State University*)
	Prof. dr. O. Pouliquen (*Universite Aix Marseille*)
	Prof. dr. T. Oosterkamp

Casimir PhD Series, Delft-Leiden, 2011-16
ISBN 978-90-8593-105-8

Dit werk maakt deel uit van het onderzoeksprogramma van de Stichting voor Fundamenteel Onderzoek der Materie (FOM), die financieel wordt gesteund door de Nederlandse Organisatie voor Wetenschappelijk Onderzoek (NWO).

In the time of my confession, in the hour of my deepest need
When the pool of tears beneath my feet flood every newborn seed
There's a dying voice within me reaching out somewhere,
Toiling in the danger and in the morals of despair.
Don't have the inclination to look back on any mistake,
Like Cain, I now behold this chain of events that I must break.
In the fury of the moment I can see the Master's hand
In every leaf that trembles, in every grain of sand.

Bob Dylan

For Mrs. Martin
and
Mr. Wereley

Contents

1 Introduction **1**

1.1 Previous work on flow and fluctuations in granular systems 3

1.1.1 The split-bottom geometry 4

1.1.2 Shallow flows 5

1.1.3 Deep flows 7

1.1.4 Dilation in sheared systems 8

1.1.5 Fluctuations in granular materials 9

1.1.6 Rheology of driven granular matter 12

2 Shear creates a granular liquid **15**

2.1 Introduction 15

2.2 Agitation of grains through flow 17

2.2.1 Experimental setup and procedure 17

2.2.2 Phenomenology 20

2.3 Archimedes' law in a granular fluid 21

2.4 Viscous drag in a granular fluid 24

2.4.1 Equation of motion 24

2.4.2 How the viscosity depends on the ambient humidity, Ω, H, z, M and R 28

2.4.3 Does the local flow rate set the viscosity? 34

2.5 Conclusion 36

2.6 Appendix: Fitting the probe position as a function of time . 38

3 Fluctuations in a granular liquid **39**

3.1 Introduction 39

3.2 Describing the fluctuations 41

3.2.1 Parameterizing the fluctuations using the probability distribution function 42

3.2.2 Parameterizing the fluctuations using the mean square displacement 43

3.3 Tuning the fluctuations with experimental parameters . . . 45

3.3.1 Tuning the fluctuations by changing the disk speed . 45

3.3.2 Tuning the fluctuations by changing the filling height 47
3.3.3 Tuning the fluctuations by changing the probe depth 49
3.3.4 Tuning the fluctuations by changing the probe mass 52
3.3.5 Tuning the fluctuations by changing the probe radius 53
3.3.6 Tuning the fluctuations by changing the particle size 54
3.3.7 Moving the probe away from the centre of the cell . 55
3.4 Conclusion 56
3.5 Appendix: Describing the motion of the probe 58
3.6 Appendix: What causes the fluctuations? 59
3.6.1 The effect of the disk surface on the fluctuations . . 59
3.6.2 The effect of the driving mechanism on the fluctuations 60
3.6.3 The effect of probe rotation on the fluctuations . . . 61
3.6.4 The effect of tilting the probe on the fluctuations . . 62
3.6.5 The influence of bead surface properties on the fluctuations 62

4 Oscillatory shear in a granular system 65
4.1 Apparatus 66
4.2 Probing dilation and compaction 67
4.2.1 Short time-scale behaviour 68
4.2.2 Long time-scale behaviour 68
4.2.3 Role of grain preparation 70
4.2.4 The final density and the oscillation amplitude . . . 70
4.3 Describing the motion of a heavy sinking probe 71
4.3.1 Annealing time 73
4.4 The effect of A and Ω on the sinking speed of a heavy probe 74
4.4.1 The sinking speed of a heavy probe is proportional to Ω 75
4.4.2 The sinking speed of the probe is proportional to A at small amplitudes 76
4.5 Angular response under oscillatory driving 77
4.5.1 The effect of Ω on the rheometer trajectory 78
4.5.2 The effect of A on the rheometer trajectory 79
4.5.3 The effect of z on the rheometer trajectory 79
4.6 Conclusion 80

5 Equipartition in a 2D granular gas **83**
5.1 Introduction 83
5.2 Apparatus 85
5.2.1 Particle properties and moments of inertia 87
5.2.2 Particle tracking 89
5.3 Velocity distributions 91
5.4 Behaviour of particles in contact 94
5.5 Energy injection 96
5.6 Equipartition 97
5.7 Equation of state 99
5.8 Fluctuation-dissipation temperature 102
5.9 Conclusion 104

Bibliography **107**

Summary **115**

Samenvatting **119**

Publication List **123**

Curriculum Vitae **125**

Acknowledgements **127**

Chapter 1

Introduction

Figure 1.1: Sulphur heaps in the harbour in Vancouver.

As an undergraduate, I was intrigued by the conical shape of the enormous sulphur piles in the harbour in Vancouver: why did the heap form at that *particular* angle? And why did the granules flow in the pipe and solidify as they trickled down the heap? I tried to calculate the angle of repose, but I soon realized that the problem was intractable: because the pile was *disordered*, it was impossible to describe the whole system by examining the behaviour of only a few granules - and the heaps contained so many particles that even a computer would never calculate all the forces acting on each of the grains! Moreover, an understanding of Newton's laws could not illuminate the difference between the flowing and stationary particles. Like other many-body systems, the properties of a granular heap were determined by emergent behaviour which could not simply be understood from a description of the interaction between the individual grains.

In some ways, granular materials are the simplest possible many-body system. Unlike atomic or colloidal particles, grains interact only through friction and mechanical repulsion when one particle is in contact with another. Granular materials are also *athermal*: the change in the gravitational energy of a sand grain lifted 1 mm exceeds $k_B T$ by 14 orders of

magnitude. Developing a better understanding of the properties of granular materials is therefore likely to provide insights into the fundamental characteristics of other disordered many-body systems.

Understanding the behaviour of granular systems is a problem that has been tackled by both engineers and physicists. A description of the yielding and flowing behaviour of granular materials is necessary for controlling and managing phenomena such as avalanches or subsidence during earthquakes. However, describing the bulk properties of granular materials is a difficult problem because the properties of driven granular systems often depend strongly on how the grains are excited - tapping, vibration, shear and gas-fluidization generate states which respond differently to external stresses [1–6].

Much of the earlier work on granular systems focuses primarily on a solid-like, "jammed" regime, in which particles are packed tightly together [7], and a kinetic regime, in which violent agitation causes the particles to bounce around, colliding ballistically with other particles and the walls of the container [8]. Like the yellow sulphur granules, steel beads poured on a heap illustrate some of the different phases of granular matter (Fig 1.2).

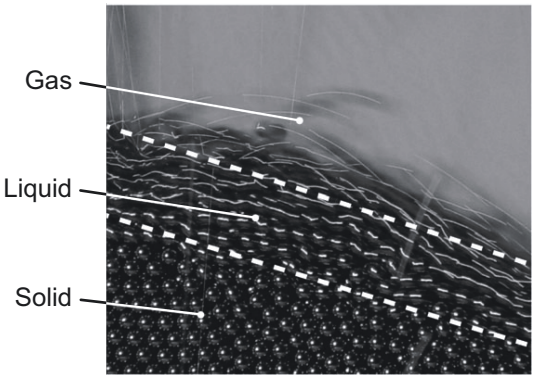

FIGURE 1.2: Steel beads poured on a pile illustrate the three distinct phases of granular matter. Figure adapted from [2].

At the surface of the pile there is a gaseous regime where particles move rapidly and collide ballistically, while far away from the surface of the heap there is a solid-like phase in which the particles are packed

together densely and do not undergo rearrangements. In between the gaseous and solid-like regimes there is a region where the particles have enduring frictional contacts, but are still able to rearrange and slide past one other. It is this flowing regime which is hardest to describe, and which is the main subject of this Thesis.

To what extent do granular phases mimic their atomic analogues? How can we adapt the tools of statistical mechanics and rheology to describe the behaviour of a granular system? In this Thesis we will examine and characterize the fluid-like qualities of a granular system excited by shear, as well as the gas-like qualities of pucks on an air hockey table driven by bumpers.

We will begin with a short introduction to previous work on fluctuations and fluidization in granular systems. In the subsequent Chapters we will describe the results of experiments on both the microscopic and macroscopic fluid-like characteristics of driven granular matter. In Chapter 2 we characterize the motion of an object moving in a sheared granular material. We find that this system has many of the characteristics of an ordinary liquid: light objects obey Archimedes' Law, while sinking and rising objects behave much as though they are in a viscous fluid. In Chapter 3 we examine how the properties of this sheared granular liquid are related to fluctuations in the system. Finally, we complete our investigation of shear-fluidized granular media by examining the behaviour of grains excited by oscillatory shear (Chapter 4).

In Chapter 5, we describe an experiment on a model granular gas which was performed during a three month stay in the group of Karen Daniels at North Carolina State University. In this study, we track the translational and rotational motion of particles on an air hockey table which are excited by bumpers mounted along the sides of the apparatus. We find that there is equipartition of translational and rotational energy and that the system can be described with a van der Waals-like equation of state.

1.1 Previous work on flow and fluctuations in granular systems

When stress or strain is applied to a granular material, the system typically responds in a non-uniform - and non-trivial - manner. A system un-

der constant *stress* can be created using an inclined plane; the grains will flow when the plane tilted above a critical angle. However, when the angle is reduced below the critical value, the flow will stop and the packing will jam: there is both a critical stress required to cause flow and a minimum possible flow rate for stress-controlled flows. Very slow flows must therefore be created by placing a system under constant *strain* - which can be accomplished by using a container with a moving boundary.

Several geometries allow excitation with constant strain. In the planar geometry, granular material is sheared between two parallel plates, while in a Couette cell, shear is generated between an inner and an outer cylinder as one of the cylinders rotates. In slow chute flows, the flow is generated by slowly lowering the bottom plate on which the grains rest [9].

In each of these geometries the flow is localized near a boundary in a *narrow shear band* - a region where the flow speed changes rapidly in the direction perpendicular to the flow. In the Couette geometry, shear bands typically have a thickness of five to ten grain diameters and form near the central cylinder. The location of the shear band is the same for both 2D and 3D systems and for different driving rates [10, 11]. Away from the shear band the gradient in the flow is very small and similar shear localization can be observed in slow chute flows.

In this Thesis we study the behaviour of grains sheared in a split-bottom cell. As we will discuss below, this allows us to create shear zones that are much wider than the typical 5-10 grain diameters observed in other geometries. In addition, the shear zones in a split-bottom setup are pinned away from the boundaries, allowing us to probe the bulk behavior of the system.

1.1.1 The split-bottom geometry

A relatively novel experimental system which imposes strain at a constant rate is the split-bottom geometry. In this setup the grains are driven by a rotating disk with radius R_S in the bottom of the container. Alternatively, the disk can be fixed while the container rotates (Fig 1.3). The diameter of the disk is less than the diameter of the container so that a discontinuity in the flow is introduced away from the walls.

Unlike in Couette flows, chute flows and planar flows, the shear band induced in the split-bottom geometry is very wide. The resulting grain flows are smooth and constant in time, so flow profiles in the cylindrical

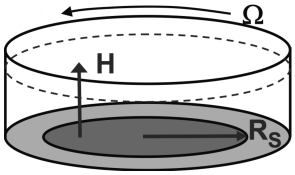

FIGURE 1.3: A split-bottom cell. A disc with radius R_s revolves at a rate Ω in the bottom of the container. Grains fill the system to a depth H. (The outer cylinder can also be made to rotate while fixing the inner disc.) Figure excerpted from [12].

split-bottom geometry can be completely characterized by the radius of the spinning disk, R_S, the depth of the grains, H, and the disk rotation rate, Ω. The azimuthal velocity of the grains, ω, can be determined as a function of the height above the disk, z and the radial distance from the centre of the disk, r. For $\Omega < 0.1$ s^{-1}, the flow speed, $\omega(r, z)$, is simply proportional to Ω. Since centrifugal forces are negligible for $R_s \approx 10$ cm, the flow profiles obtained for geometries with a rotating disk and fixed container are the same as for geometries with a rotating container and a fixed disk [13–15].

There are three flow regimes in a split-bottom setup, the choice of which is determined exclusively by the depth of the grains, H, and the radius of the spinning disk, R_S [13–15]. In shallow flows ($H/R_S < 0.45$), the shear band extends to the surface forming a trumpet-shaped region where the grains rotate with the spinning disk. In deep flows ($H/R_S > 0.65$), the shear band forms a dome and the grains at the surface precess much more slowly than the spinning disk. For flows with $0.45 < H/R_S < 0.65$, the behaviour of the system incorporates elements of both shallow and deep flows (Fig 1.4).

1.1.2 Shallow flows

At low filling heights a narrow shear zone forms at the edge of the disk and propagates upwards in the grains. As H increases, the shear band widens and shifts away from R_S towards the center of the shear cell. Experiments and numerical simulations have examined both the flow at the surface and the flow in the bulk. Profiling the flow of grains beneath the surface of the split bottom cell is experimentally challenging because it is difficult to image particles in the interior of the system. However, burying and excavating coloured beads [14], MRI [16, 17] and numerical simulations

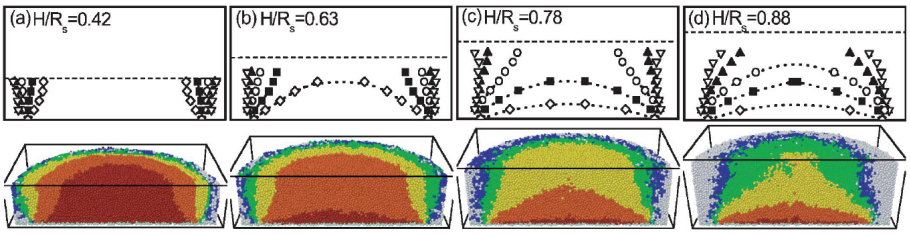

FIGURE 1.4: Contours of constant angular velocity ω, for different filling heights, H. Upper panels: MRI experiments: $\omega = 0,84$ (diamonds), 0.24 (squares), 2.4×10^{-2} (circles), 2.4×10^{-3} (triangles), and 2.4×10^{-4} (inversed triangles). Dashed lines indicate H and dotted lines are guides to the eye. Lower panels: simulations. Color is used to identify velocity ranges: dark red, $\omega \in [0.84, 1]$; orange, $\omega \in [0.24, 0.84]$; yellow, $\omega \in [2.4 \times 10^{-2}, 0.24]$; green, $\omega \in [2.4 \times 10^{-3}, 2.4 \times 10^{-2}]$; blue, $\omega \in [2.4 \times 10^{-4}, 2.4 \times 10^{-3}]$; grey, $\omega \in [0, 2.4 \times 10^{-4}]$. Figure from [16].

[16, 18–20] allow flow in the bulk to be studied.

At the surface, the flow speed, ω, can be expressed as a function of, the distance from the centre of the cell (r), the width of the shear band (W), and the position of the center of the shear band, (R_C such that $\omega(R_C) = 0.5$):

$$\omega(r) = \frac{1}{2} + \frac{1}{2} erf(\frac{r - R_c}{W}), \tag{1.1}$$

The centre of the shear zone, R_C, is independent of the material from which the particles are made [14], so R_C is completely determined by H and R_S:

$$(R_S - R_C)/R_S = (H/R_S)^{5/2}. \tag{1.2}$$

Like the surface flow, the flow rate at a distance z beneath the surface has the form of an error function. The position of the shear zone in the bulk is predicted by a simple argument introduced by Unger *et al.* in which the bulk flow profile is completely determined by the position of the shear band at the surface, $R_C(R_S, H)$. The system can be separated into two segments, one extending from the bottom of the container to the surface (height H) and the second extending from z to H with height ($H - z$). Since the position of the centre of the shear band at the surface is the same for both systems, the centre of the shear band, r at z can be determined by solving $R_C(R_S, H) = R_C(r, H - z)$ [21]. This gives:

$$z = H - R_c \left[1 - R_c/R_s(1 - H/R_s)^{2.5})\right]^{1/2.5} \ . \tag{1.3}$$

Although the shape and surface properties of the particles do not affect the position of the centre of the shear band, the width of the shear band, W, is determined exclusively by the size, shape and surface properties of the grains [14]. The width of the shear band at the surface, $W(H)$, is $\sim (H/d)^{2/3}$, where d denotes the particle diameter. The width of the shear bands as a function of the depth in the system ($W(z)$) is more difficult to measure; however, available data suggest that $W \sim z^{\alpha}$, where $0.5 > \alpha > 0.25$ [14, 22]. Meanwhile, simulations [19] indicate that $W(z) = W(z = H)\sqrt{1 - (1 - z/H)^2}$.

1.1.3 Deep flows

When $H/R_s > 0.65$, the shear band no longer extends to the surface of the system; instead, a stationary dome-shaped region forms over the disk while the remainder of the system revolves [15–17, 21]. (If the disk is driven while the container is stationary, the symmetric case occurs: the dome precesses and there is very little rotational motion at the surface.) Cheng *et. al.* [16] found that the axial velocity profile $\omega(z)|_{r=0}$, can be described by a Gaussian:

$$\omega(z, r = 0) = \omega_p + (1 - \omega_p) \exp(-z^2/(2\sigma^2)) \ , . \tag{1.4}$$

Here, the bottom disk is fixed and the outer part of the container rotates with velocity Ω. The rotation rate at the surface at $r = 0$, ω_p, decreases exponentially with H. The width of the bulk Gaussian velocity profile, σ, is approximately $R_S/5$ [16]. Finally, the width of the shear band, W, is approximated by the scaling law $W/d \sim (H/d)^{2/3}$, where d denotes the particle diameter.

In the intermediate regime where $0.45 < H/R_s < 0.65$, the dome over top of the disk has not yet completely closed. The surface velocity profiles, $\omega(r)$, can be described by modifying Eq. 1.1:

$$\omega(r) = \frac{1}{2} + \frac{1}{2} erf(\chi(r)) \ , . \tag{1.5}$$

The polynomial correction, $\chi(r)$, has the form $a_0 + a_1\ r + a_3\ r^3$ [15]. For shallow layers, $a_3 \to 0$, while a_0 and a_1 can be determined from Eq. 1.2 and the scaling law $W(H) \sim (H/d)^{2/3}$.

In Chapter 2 we report on additional measurements of flow profiles in the split-bottom setup in which we use a rheometer to measure the local flow at different depths in the system.

1.1.4 Dilation in sheared systems

Another property of sheared granular systems is that the applied strain causes the system to dilate. This is because the particles can rearrange more easily when additional free volume is available in the system: In the Couette geometry, the system dilates a greater amount closer to the driving wall than further away [10, 23, 24]. Dilation is also observed in rate independent chute flows [25].

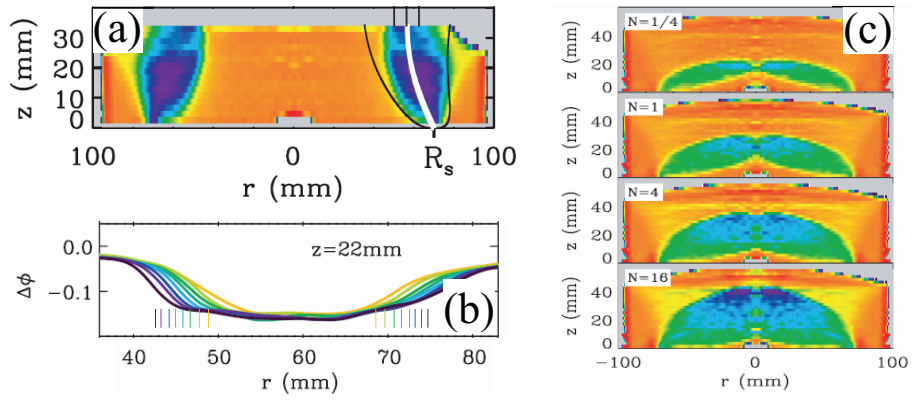

FIGURE 1.5: Evolution of dilatancy. (a) Color map of relative density change (light blue corresponds to -10%) for $H/R_s = 0.51$ after 4 rotations of the bottom disk. (b) Spread of dilated zone for vertical shear observed in the bulk at $H/R_s = 0.51$ at $z = 22$ mm ($H = 36$ mm), for $N = 1/2, 1, 2, \ldots, 64$, compared to estimates where, after N turns, the local strain equals one. (c) Spread of dilatancy for dome-like flow observed at $H/R_s = 0.77$, for the number of disk rotation N as indicated. Figure from [17].

Direct measurements of the evolution of the local packing density of the shear flow in the split bottom geometry have been performed by using Magnetic Resonance Imaging to examine poppy seeds [17]. When strain is applied to the system the shear zone begins to dilate, gradually expanding to the steady state after several revolutions of the container (Fig. 1.5). In

the steady state the shear band dilates 10-15 % relative to the undriven state. Although local strain rates vary over several decades, the density across the shear band is fairly constant, suggesting that the density of the flowing material is a function of the total strain, rather than the strain rate. This observation is corroborated by Kabla [26] in X-ray studies of a linear shear cell.

1.1.5 Fluctuations in granular materials

Fluctuations in granular systems are manifested in several ways: in a dense system there are fluctuations in the contact forces between particles, while in more dilute systems there are fluctuations in the particle positions and velocities.

These fluctuations are interesting for several reasons. First, it is still not clear whether or how conventional thermodynamics might be modified to describe granular systems. Fluctuations in thermodynamic quantities in non-dissipative systems can be used to determine the temperature: but do fluctuations in similar quantities in granular systems may also behave in a temperature-like manner? [27] Investigating the character of fluctuations in granular materials may also provide insight into the behaviour of other out-of-equilibrium systems, such as glasses.

Second, developing a description of fluctuations in granular materials is important for understanding how the microscopic behaviour influences the macroscopic properties of the system. For example, the distribution of force fluctuations can indicate the anisotropy of contact and force networks which encodes the flow history. Moreover, developing a better understanding of the jamming transition - and critical behaviour in general - requires a good description of both the microscopic and macroscopic properties of ensembles near the jamming point. Many granular phenomena have an intrinsically small length scale (such as the shear bands discussed above), and it is simply not possible to go to a continuum limit - there is no separation of length scales and it is not clear what happens to these length scales close to jamming. Studies of fluctuations in very dense systems have therefore been undertaken to try to understand what happens near the jamming transition and to develop more insight about how to describe both jammed and unjammed systems.

There are several experiments and simulations which examine granular analogues of Brownian motion. These systems typically consist of

driven particles which interact with a larger probe particle whose motion can be tracked. Alternatively, it is also possible to track the motions of all the particles if the system is two-dimensional or clever imaging techniques (MRI, immersion in an index matched fluid) are used.

In order to determine whether the motion of individual particles is diffusive, it is necessary to examine under which conditions the probability distribution of particle displacements is Gaussian, and to determine if the second moment of this distribution grows linearly with time. Fluctuations in granular media are often not normally distributed: fluctuations in the forces in a dense, flowing system have an asymmetric distribution [28], while in granular gases the velocity distributions are typically observed to have the form of a stretched exponential, $e^{-(v/\alpha)^\beta}$, where $1 \geq \beta \geq 2$ [29–33]. In sheared foams, the distribution of particle positions exhibits fat tails on short time scales, exponential tails on intermediate time scales, and Gaussian behaviour on long time scales. Concomitant with these transitions are crossovers from super-diffusive behavior at early times to diffusive behavior at long times [34]. Similar complex behavior can be seen in colloidal glasses. On short time sales there is a diffusive or superdiffusive regime where particles explore the region between neighbouring particles. On longer time scales there is a characteristic plateau in the mean square displacements where particles are trapped in a “cage" produced by neighbouring particles. Finally, on very long time scales the system exhibits diffusive behavior again as the cages break and particles rearrange (alpha-relaxation) [35]. Similar caging behaviour has also been observed in granular systems: Reis *et. al.* examined the trajectories of vertically vibrated particles in a quasi-2D system [36]. The mean square displacements of the particles are diffusive on short time scales but exhibit the plateau characteristic of caging on longer time scales (Fig 1.6).

Fluctuations in particle positions have also been measured in granular systems. d’Anna *et. al.* have probed the rotational fluctuations of a torsional probe in a vibrated granular system [37]. The system is driven by white noise vibrations while the motion of a freely-rotating conical probe attached to a torsional spring and submerged to a depth of 1 cm is observed. The probe motion appears to be Brownian, and the authors cast the dynamics of the probe in the form of the Langevin equation; this allows an effective temperature to be determined. d’Anna et. al. also measure the viscosity of the system by applying a constant force to the

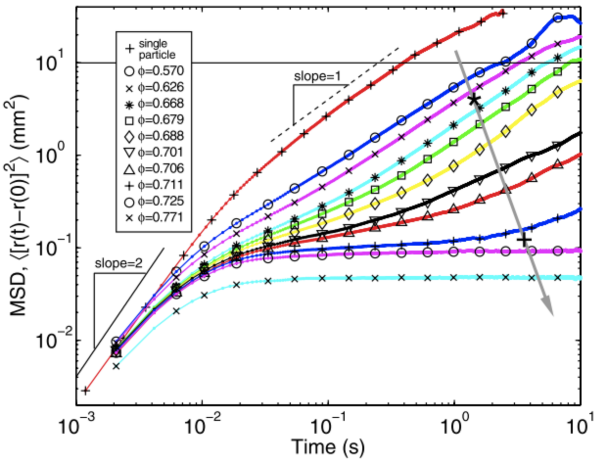

FIGURE 1.6: Mean square displacement curves of vertically shaken grains. The behaviour of a single particle in the cell is indicated by + symbols. The arrow points in the direction of increasing ϕ. The horizontal line at 9.954 mm^2 corresponds to the square of $1/4$th of the linear dimension of the imaging window, above which finite system size effects become important. Figure from [36].

probe and observing the resulting rotation. They find that the temperature and viscosity are described by the Einstein relation, suggesting that the fluctuations in this system are thermal-like. There is, however, a serious problem with the experimental setup: because the probe is vertically fixed while the grains are shaken, mechanical noise is generated when the grains slide past the probe. It is far from clear whether the measured noise is intrinsic to the system - or merely indicative of stick-slip motion. It is therefore still an open question whether the fluctuations of the probe can be thought of as strictly analagous to Brownian motion.

Numerical simulations of a colliding grains and an additional particle which is much more massive than the others have been performed by Sarracino et. al. [38] The particles are coupled to a thermostat-like energy source, with a typical interaction time which is larger than the interparticle collision time. The massive probe particle undergoes non-equilibrium Brownian motion which can be described with the Langevin equation provided that the mass of the intruder particle is much greater than that of the other particles, that the packing fraction of the gas is low (< 0.08 and that

the collisions are elastic enough that non-Gaussian corrections to the forcing distributions can be disregarded. The temperature of the system can be determined from the width of the distribution of the forces imparted on the probe particle during collisions. The authors also find that the velocities of colliding particles are uncorrelated, indicating that molecular chaos is valid in their system. Note, however, that for all but the most energetic excitations, the packing fractions in typical granular systems are much larger than those probed here.

Fluctuations in particle positions in a dense systems appear to exhibit unusual behaviour close to jamming. Experiments performed with a system of horizontally vibrated, bidisperse grains indicate that when the density of the system is close to ϕ_J, fluctuations in the positions of the particles are superdiffusive. [39], [40]. The particles undergo jumps that are random in time but correlated in space, which suggests that the system exhibits micro-crack events at all scales. As the volume fraction departs from the critical jamming density, the distribution of particle displacements is truncated at a smaller and smaller jump size, inducing a crossover towards standard diffusive motion at long times.

In Chapter 3 of this Thesis we will examine the character of fluctuations of a probe floating in a sheared granular fluid, while in Chapter 5 we will examine the translational and rotational velocity distributions of particles floating on an air hockey table and enquire if the fluctuation-dissipation theorem can be be used to describe the fluctuations of a piston enclosing the two-dimensional granular gas .

1.1.6 Rheology of driven granular matter

In vigorously-driven granular systems, particles undergo ballistic collisions and do not stay in contact for long periods of time. However, in more gently-driven experiments the particles remain in contact and the system typically begins to exhibit the characteristics of liquids or visco-plastic materials. In driven granular systems there is often a flow threshold: if the system is not excited vigorously enough the beads exhibit a yield stress. Above this threshold the yield stress disappears. In addition to the absence of a yield stress, another characteristic of a liquid-like system is the presence of a linear relationship between the force on a test particle and the resulting velocity of the particle. In the following paragraphs we will discuss several experiments in which the viscosity of a liquid-like granular

system is examined.

Caballero-Robledo *et. al.* [41] determined the viscosity of a weakly vibrated granular packing under a constant confining pressure by measuring the force needed to drag a wire along its length at constant velocity. The wire is held in tension by masses suspended over pulleys at either end. By varying the masses, the force on the bead can be modified; the wire is free to move in the direction parallel to length of the wire. As the driving vibration energy is increased, the yield stress vanished and the effective viscosity decreased dramatically. When the system is vigorously driven and the wire velocities are small, the system behaves in a liquid-like manner and the force on the test wire is proportional to the velocity. The experimenters also examined what happens when a bead is attached to the wire. It was found that the drag force on the bead scales linearly with the diameter of the bead; this scaling behaviour is also a property of spheres moving in a viscous liquid.

The motion of an intruder particle in a vibrated system has also been used to study the transition from a liquid-like state to a jammed state [42]. In this experiment, a probe particle is dragged with a constant force through a horizontally vibrated monolayer of grains. At moderate packing fractions the intruder moves rapidly as soon as the force, F, is applied, while above a threshold density the motion of the probe becomes intermittent. The fluctuations in the probe trajectory are also observed to exhibit critical behaviour at the jamming transition. Below the jamming transition $F \propto v$, while above the jamming transition $F \propto ln(v)$. Other experiments in which a probe particle is dragged through vertically vibrated grains also indicate that there is a transition to a liquid-like regime where $F \propto v$ when the maximum acceleration imparted by the driver is $\approx$ 1g [43].

The rheological behaviour of a system of glass beads excited by piezoelectric transducers has also been studied [44]. The transducers inject energy to the system in a disordered manner with accelerations that are much smaller than gravity. The system responds by compacting slowly without convection. Cabellero *et. al.* characterize the system by dragging a probe particle through the grains at constant velocity. They find that the drag force on the probe depends significantly on the vibration intensity and that the drag force increases logarithmically with the particle velocity. This unliquid-like behaviour may occur as a result of compaction in

the system: the liquid-like behaviour observed in [41] suggests a more energetic excitation is required to dilate the system and induce fluidization.

Drag forces on particles excited by shear in a Couette cell [45] are also observed to scale with $ln(v)$. In addition, there is a power law relationship between the reduced packing fraction, $\phi - \phi_c$, and the drag force: $F_{dr} \propto (\phi - \phi_c)^{1.5}$. A second unliquid-like feature of the system is that the mean drag force depends nonlinearly on the diameter of the tracer particle.

Driving an intruder into stationary grains is another way to cause localized fluidization in a granular material [46]. Drag forces on intruders slowly plunging into and withdrawing from shallow beds of monodisperse smooth glass beads scale with the immersion depth, z, and narrowest dimension, l, of the intruder. The pressure exerted on the surface of the intruder scales as $z^{1.3}l^{-0.3}$ for a descending probe, $z^{1.8}l^{-0.8}$ for an ascending probe and z^1 for a horizontally moving probe. Of course, for a simple liquid the pressure exerted on the surface of the intruder should scale as z^1. The force require to drive the intruder in to the system is always larger than the force required to withdraw the intruder; in order to insert the intruder the force has to be large enough to evacuate grains from the path of the probe.

The range of liquid-like and unliquid-like behaviours exhibited by the above experiments indicate that the properties of a driven granular system depend strongly on the excitation method. In this Thesis we will study another driving mechanism: shear in a split-bottom cell. Compared to the above systems, our experiment is very liquid-like: there is no yield stress and objects sinking in the grains experience viscous drag (Chapter 2). We also examine the more complex behaviour which results when the system is driven by oscillating the disk (Chapter 4).

The experiments described above focus on the *bulk* properties of a granular system; however, far less is known about the *microscopic* origins of liquid-like behaviour in granular media. We have therefore investigated the relationship between fluctuations experienced by a floating probe and the fluid-like behaviour in our continuously sheared granular system. In addition, we also examine the relationship between the distributions of particle velocities, the fluctuations of a piston and the gas-like behaviour observed in a horizontal bumper-driven system (Chapters 3, 5).

Chapter 2

Shear creates a granular liquid

2.1 Introduction

What governs the flow of granular media? At the grain level, interactions are mediated by collisions and contacts [47]. While rapid flows in which collisions dominate can be described by advanced kinetic theories [8], and the understanding of flows where both contacts and collisions are important has recently advanced tremendously [9, 48], it remains difficult to describe slow flows where enduring contacts dominate the interactions.

The character of such slow grain flows can be described by a frictional rheology in which the friction laws acting at the grain scale are translated to effective friction laws for the stresses acting at a macroscopic level [7, 49, 50]. In such a Mohr-Coulomb picture, granular media remain jammed when the ratio of shear (τ) to normal stresses (P) is below a critical value given by an effective friction coefficient (μ), while slowly flowing grains exhibit stresses close to the yielding criterion: $\tau/P \gtrsim \mu$.

However, this framework is not complete. The combination of rate independence and a sharp yielding criterion suggests that flow should be localized in shear bands of vanishing width and that there should be a corresponding sharp separation between stationary zones and flowing zones [7]. However, in experiments, shear bands are found to be of finite width and the boundary between flowing and stationary zones is not sharp, with creep flow occurring even far away from the main shear band [10, 13, 16, 51–53]. The first key question is therefore: what is the nature of the nearly-stationary zones far away from the main flow? A second key question is motivated by the observation that, for slow flows, the flow rate is independent of the stresses. But if the flow rate is not determined by the stresses, what then is the physical mechanism that sets the flow rate of slow granular flows? [7, 48, 49].

In the experiments described in this Chapter, we address these questions by locally stirring glass beads in a split-bottom shear cell while prob-

ing the mechanical response of the essentially quiescent regions outside the shear band. Details of the setup can be found in Sec 2.2.1.

In the absence of stirring, the grains exhibit the usual physical properties of a static sand pile and will support an object of moderate mass placed on the surface: *collectively*, the beads exhibit a yield stress. However, when a spinning disk is placed in the bottom of the container, an intruding object will immediately begin to sink into the beads. An object which is denser than the mixture of beads and air in the container will continue to sink until it is completely submerged. Meanwhile, a low-density object placed in the beads while the disk is rotating will rise or sink until it floats at an equilibrium depth given by Archimedes' law.

That these behaviours are surprisingly liquid-like motivates us to treat the granular medium as a fluid and posit questions about the macroscopic properties of the system. Does the granular medium exhibit a yield stress? What parameters determine the speed at which a probe sinks? And what physical mechanism causes the probes to sink and float?

First, we will establish that the equilibrium depth of a low-density object *rising* in the grains is equal to the equilibrium depth of that same object *sinking* in the grains. This demonstrates that our granular liquid does not exhibit a yield stress. If there were a finite flow threshold, sinking probes would get stuck at a different depth than rising probes. Moreover, we find that the equilibrium depth of the probe can be predicted from the density of the granular medium and the dimensions of the probe: objects floating in the grains obey Archimedes' rule.

Second, we have found that probes sinking or rising towards equilibrium have a trajectory which is exponential in time. Since the sum of the gravitational and buoyant forces is linear in the deviation from the equilibrium position, the exponential relaxation strongly suggests that the drag forces on a moving probe are linear in velocity - just as for viscous drag. From the gravitational force, buoyant force, and the vertical position of a sinking (or rising) object as a function of time, we define and measure an effective viscosity. We find that hat the viscosity depends weakly on the vertical position of the probe and that the viscosity increases when the shear cell is filled to larger heights. In addition, we observe that the viscosity is inversely proportional to the disk rotation rate and that, unlike a Newtonian liquid, the viscosity also depends on the radius (R) and mass (M) of the probe: although we are limited to studying probes with a small

range of radii and mass, our observations suggest that the viscosity scales inversely with $(M/R^2)^2$.

Third, we have investigated whether the local flow rate under the probe sets the effective viscosity. Using a rheometer, we have measured the local flow rate along the central axis of the rotating disk for several different filling heights; we compare this rate to the local viscosity as determined from sinking probe experiments. We find that the local strain rate and viscosity are very poorly correlated: the flow rate can decrease by a factor of 1000 while the viscosity changes by less than a factor of three. This result suggests that the effective viscosity is determined by agitations produced by distant flow rather than by the local flow near the probe.

In conclusion, we find that although there is a linear relationship between the drag force and the sinking speed of the probe, the viscosity is also dependent on the pressure exerted by the probe: the granular medium cannot be a simple Newtonian liquid. We also find that the relation between the applied stress and observed strain rate in one location is poorly correlated with the local strain rate and instead depends on the strain rate in another location. Descriptions of the complex rheology and novel behaviour we observe are therefore crucial for the development of better models of slow granular flows [18, 22, 54–56].

2.2 Agitation of grains through flow

We induce shear flow in a container of glass beads by rotating a disk in the bottom of the vessel - a split bottom setup. The fluid-like characteristics of the beads can then be probed by observing the motion of a low-density object sinking (or rising) in the grains. Here we discuss our setup, experimental procedure and main phenomenology.

2.2.1 Experimental setup and procedure

In this experiment, a split bottom cell (Fig.2.1) is filled with 1 mm glass beads to a depth (H) ranging from 45 to 80 mm. The sidewalls are roughened by teeth of length 2 mm and height 2.5 mm which are machined into the walls of the container. Because of these teeth, the radius of the container varies between $R_C = 80$ and $R_C = 82.5$ mm. The bottom disk has a radius of $R_D = 60$ mm and is roughened by hemispherical dimples with

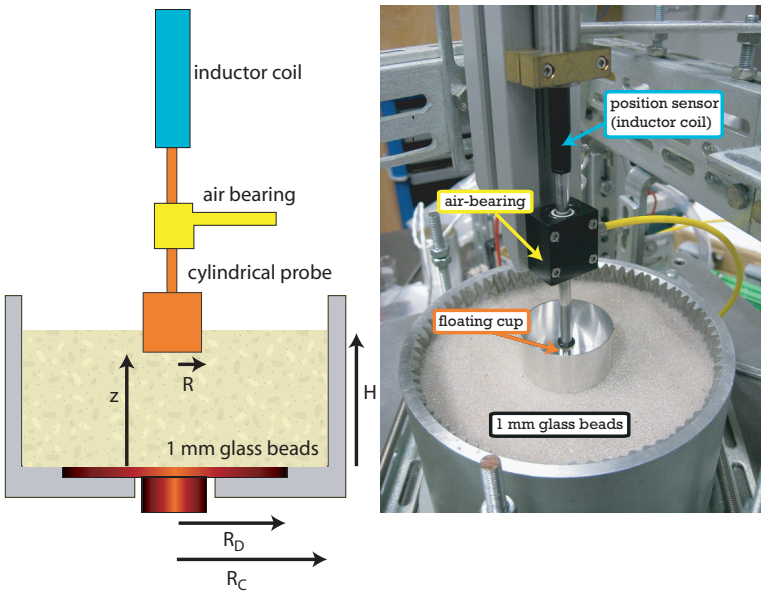

FIGURE 2.1: The spinning disk (radius $R_D = 60$ mm) revolves in the bottom of a cylindrical container (radius $R_C = 80$ mm) which has been filled to a height (H) with 1 mm glass beads. The distance between the spinning disk and the bottom of the probe is denoted by z. The hollow cylindrical probe has mass, M and radius, R. A photo of the experimental setup is on the right.

a diameter of 3 mm. The disk is driven at a rate Ω, with either a stepper motor attached to a belt or directly by a stepper motor - the precise driving mechanism only has a negligible effect on the behaviour of the system, and we conclude that there are no spurious vibrations introduced when the motor drives the disk directly. The humidity of the system is controlled by placing the apparatus in a small plastic tent and allowing dry air escaping from the air-bearing (see Fig. 2.1) to flow over the grains. The humidity is maintained at $7 - 9\%$ at room temperature. This setup produces granular shear flows which have already been described in detail [12–16, 21, 57].

In order to investigate the rheological properties of the system we observe the motion of a probe moving vertically in the grains. The probe consists of a hollow closed cylinder attached to a shaft which passes through an air-bearing and into a DC Fastar FS1K LVDT sensor (Fig.2.1). The air-

bearing fixes the horizontal position of the probe while allowing the cylinder to rotate and to move freely in the grains in the vertical direction. Cylinders immersed in the beads have radii ranging from 7 mm to 30 mm, and the mass of the probe (M) can be varied by adding additional weights to the cylinder. The position of the probe is measured by the LVDT sensor, which has a resolution of 0.002 mm and a range of 51 mm with a linearity of $\pm 0.15\%$. Electronic noise in the signal is reduced by sampling at a rate of 250 Hz and then averaging over 10 points.

The filling height, H, (Fig.2.1) is not measured directly because the volume changes as the grains compact and dilate - packing fraction is not a constant in a granular medium. Although we report the filling height, H, we control the total mass of the grains in the container. A filling height of $H = 60$ mm measured prior to shearing the system corresponds to 2.4 kg of grains and each 5 mm increment in the filling height requires the addition of 200 g of grains.

Given that the average radius of the shear cell is 81.5 mm, we estimate that the packing density is $\rho \approx 1.92$ g/cm^3. Since grains pack less densely near the walls of the container [58], we can also obtain the density of the medium by measuring the volume of the grains placed in beakers of increasing radius and extrapolating to infinite radius. The density of well-compacted grains obtained with this method is 1.92 ± 0.05 g/cm^3. Of course, the beads dilate as they are sheared and the filling height of the sheared beads, $H(0)$, is typically 1 to 2 mm larger than the static filling height. When this dilation is taken into account, the typical densities encountered in our experiment are 1.86 ± 0.1 g/cm^3.

Protocol — In order to minimize memory effects, the grains are stirred with a rod prior to beginning a measurement. The surface of the granular medium is leveled by smoothing it with a flat plate while spinning the disk at a rate of 0.5 rps for 20 s. Exploring other initial procedures yields no evidence that the initialization process influences the long-time dynamics of the probe: the random run-to-run variation in the probe motion is larger than variation observed for different preparation methods.

At the start of a sinking probe experiment, the probe is held at a position just above the surface of the grains ($1 - 2$ mm) and then released when the disk at the bottom of the container begins spinning. Prior to beginning an experiment with a rising probe, the probe cylinder is immersed (but not completely submerged) in the beads.

2.2.2 Phenomenology

In our experiment, shear flow is generated in a container of glass beads by rotating a disk in the bottom of the vessel (Fig. 2.1). In the absence of shear, objects placed on the surface of the granular medium will become stuck after sinking a short distance (a few mm for probes with a large mass and small area). In other words, the undriven granular system exhibits a yield stress.

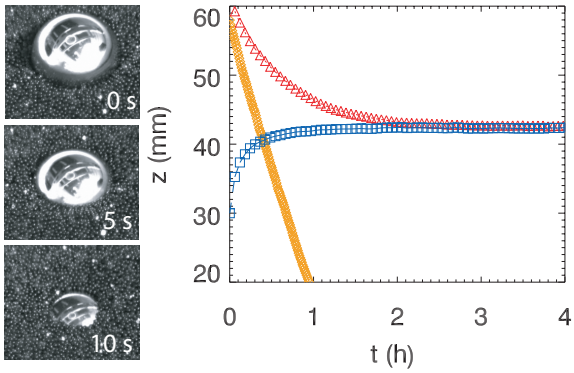

FIGURE 2.2: Examples of probe motion for filling height H=60 mm and disk rotation speed $\Omega = 0.1$ rps. Left: snapshots of a steel ball (diameter 25 mm, mass 64 g), as it sinks in the grains. When the disk is not rotating, the ball remains resting at the surface, as shown in the top panel. Right: trajectories of probes moving in the fluidized grains. The orange line denotes the motion of a high-density probe ($M = 48$ g, $R = 9$ mm). A second, low-density probe ($M = 40$ g, $R = 20$ mm) floats in the grains. This probe sinks if initially placed above the equilibrium depth (red) and rises if placed below the equilibrium depth (blue).

However, the behaviour of the grains changes dramatically when the beads are sheared by the rotating disk: a heavy object placed at the surface will immediately begin sinking and will continue sinking until it is submerged. The images of a heavy steel ball sinking over a period of 10 s (Fig. 2.2a) are a dramatic example of this phenomena. Meanwhile, low-density objects either sink or rise until they are floating in the grains (Fig.2.2). In the remainder of this Chapter, we will examine how the vertical motion of the probe ($z(t)$) depends on the rotation speed of the disk (Ω), the filling height of grains in the container (H), the probe mass (M) and radius (R).

Note that for most of our experimental conditions, the amount of surface flow that we detect in the absence of a probe is very small: at $H = 60$ mm, the residual flow at the surface is more than three orders of magnitude slower than the disk rotation rate [15, 16]. For the sample probe trajectory shown in Fig. 2.2a the residual flow at the surface is approximately one rotation per three hours. We will discuss the role of local flow rate in more detail in Section 2.4.3 below.

2.3 Archimedes' law in a granular fluid

As shown in Fig. 2.2b, low-density probes sink or rise to a well-defined equilibrium depth, z_{eq}. The probe position as a function of time for several rising and sinking experiments at $H = 60$ mm and $H = 50$ mm is plotted in Fig 2.3a and Fig.2.3c. These trajectories illustrate that probes of a given mass reach the same equilibrium depth in sinking and rising experiments for a wide range of parameters, and that when the mass of the probe is increased, the probe descends to a lower equilibrium position.

Examining a brief segment of the probe trajectory near z_{eq} reveals that $z(t)$ exhibits tiny, Gaussian fluctuations around the mean position (Fig. 2.3b). Variations in the value of z_{eq} achieved in different experimental runs are small and of the order of 0.2 mm (one-fifth of a grain diameter).

That the equilibrium position does not depend on whether the probe is initially below or above z_{eq} suggests that our granular system does not exhibit a yield stress - if there were a finite flow threshold, sinking probes would get stuck at a shallower depth than rising probes. This observation, together with the the observation that heavier probes have a deeper equilibrium depth (see Fig. 2.3c), motivates describing the probe behaviour using Archimedes' law, in which the equilibrium depth is predicted by the balancing the buoyant force and the gravitational force.

Let us now propose that a cylindrical probe floats at an equilibrium depth, $z = z_{eq}$. For an infinite container, and in the absence of any granular and dilatancy effects, Archimedes' law reads:

$$-Mg + \pi R^2 \rho g (H(0) - z_{eq}) = 0 \,, \tag{2.1}$$

where ρ denotes the effective density of the granular medium, and $H(0)$ is the filling height of the container prior to the introduction of the probe (note that the medium dilates during shear, so that $H(0)$ is typically 1 mm

larger than the initial filling height H). The change in the filling height due to dilation of the beads can be estimated by dropping a probe on to the surface of the granular system and finding the position at which the probe slows as it strikes the grains.

There are several corrections that we need to take into account in order to invoke Archimedes' law. First, since the container has a finite radius, R, immersion of a probe will displace grains and raise the height of the 'fluid'. We have therefore calculated the height of the beads in the container, $H(z)$, as a function of the depth reached by the probe, z. We assume that the beads are not dilated or compacted when the probe is immersed so that the total volume of the beads is conserved:

$$R_C^2(H(z) - H(0)) = R^2(H(z) - z) \; . \tag{2.2}$$

Solving for $H(z)$ in terms of $H(0)$ and z and replacing $H(0)$ in Eq. (2.1) with $H(z)$ yields

$$-mg + \pi R^2 \rho g \frac{R_C^2}{R_C^2 - R^2}(H(0) - z_{eq}) = 0 \; . \tag{2.3}$$

There are two additional corrections to the equilibrium depth which stem from the fact that grains pack less efficiently close to boundaries. This observation suggests that the effective radius of the probe, $\tilde{R}$, may be somewhat larger than the real value: $R < \tilde{R} < R + R_{grain}$. Similarly, grains pack less densely against the bottom of the probe than in the bulk, so the measured equilibrium depth is higher than expected. The magnitude of this correction, δH is approximately one grain diameter. When these finite size corrections are taken into account, z_{eq} is given by:

$$z_{eq} = H - \delta H - \frac{M}{\pi R^2 \kappa \rho} \; , \tag{2.4}$$

Here, all finite size corrections are combined in the effective parameters δH and $\tilde{R}$, while $\kappa = 1 + (\tilde{R}/R_C)^2$ describes the change in $H(z)$ as the probe sinks and displaces beads. The value of δH is approximately 1 mm, while for a probe of $R = 20$ mm, $1 + (R/R_C)^2 \approx 1.06$ and $1 < (\tilde{R}/R)^2 < 1.05$. The value of κ should therefore lie between 1.06 and 1.11.

The equilibrium position is calculated by fitting the probe position as a function of time to a sum of exponentials, as described in Section 2.6. In

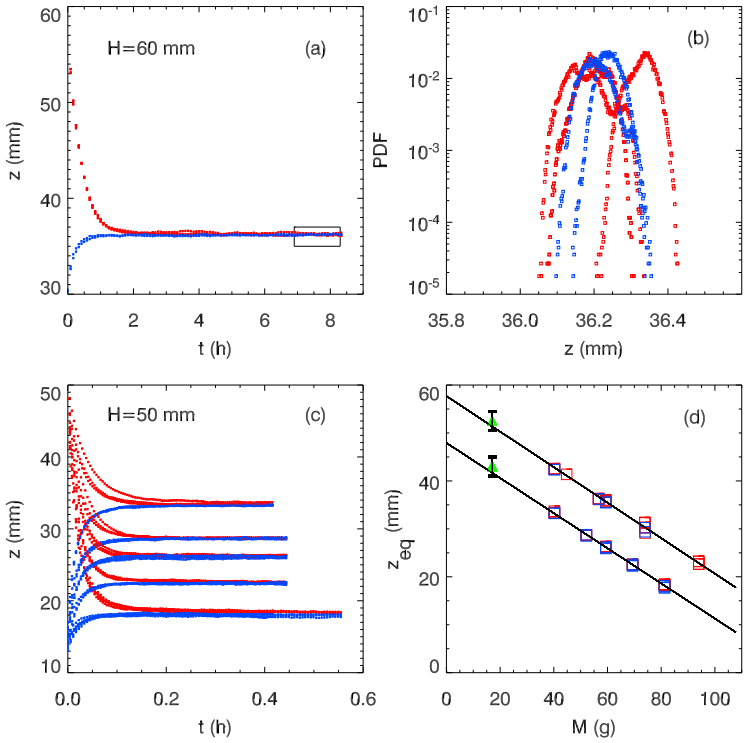

FIGURE 2.3: Floating probes behave according to Archimedes' law. All experiments are conducted with a probe of radius $R = 20$ mm and at a disk rotation speed of $\Omega = 0.1$ rps. (a) Examples of probes sinking and rising to their equilibrium depth. ($H = 60$ mm $M = 57$ g). (b) Probability densities of the probe position near equilibrium (the last 15% of each data set) for three observations of a sinking probe (red) and three observations of the same probe as it rises in the grains (blue) ($M = 57$ g, $z_{eq} \approx 36$ mm). (c) Sinking and rising probes for $H = 50$ mm - note the different time scales here and in panel (a). (d) The equilibrium depth as a function of probe mass for $H = 60$ mm (upper data set, y-intercept 56.89 mm, slope -0.358 mm/g) and $H = 50$ (lower data set, y-intercept 47.93mm, slope -0.366 mm/g). The green data points are obtained by imaging the position of a very light probe with a camera.

Fig. 2.3d, we plot the equilibrium depths of rising and sinking probes as function of probe mass for both $H = 50$ mm and $H = 60$ mm. The green data points are obtained for very light probes which, in order to reduce the mass of the probe, are not attached to an inductor rod. The equilibrium

position of the probe is therefore obtained (with less accuracy) by taking photos at intervals as the probe sinks into the grains.

As illustrated in Fig. 2.3d, the equilibrium depths can be described by Eq. (2.4). The slope of both fits is given by $(\pi R^2 \kappa\rho)^{-1}$ and is consistent with the density of the grains and our previous estimate of κ. From the fit for $H = 60$ mm data, we find that $\kappa\rho = 2.05 \pm 0.05$ g/cm^3, while from the fit for $H = 50$ mm data, we find $\kappa\rho = 2.04 \pm 0.02$ g/cm^3. From our estimate of the density (1.86 ± 0.1 g/cm^3), it follows that $\kappa \approx 1.1 \pm 0.05$, which lies within the expected range. The finite size correction δH is 2.1 mm for $H = 50$ mm and 3.1 mm for $H = 60$ mm. This correction is on the order of a grain diameter.

We conclude that Archimedes' law describes the equilibrium depths of our probes accurately, provided that the dimensions of the container and finite size effects are properly taken into account. Note that Archimedes' law has also been observed in a granular system in which the lateral boundaries are vibrated [59] — but this driving appears far more vigorous than in our system.

2.4 Viscous drag in a granular fluid

Now that we have established which forces act on stationary probes, we turn our attention to the probe dynamics — the motion of probes as they are sinking or rising. We will first establish that the approach of probes towards the equilibrium depth is exponential, which allows us to define an effective viscosity, η. We will then measure how η varies with the filling height, H, the disk rotation speed, Ω, the probe depth z, the probe mass M and the probe radius R. We will explore the effect of placing the probe off-centre and the effect of humidity on the probe. Our main conclusion is that although the drag forces on moving probes are approximately linear in the probe velocity, the drag forces depend strongly on the pressure exerted by the probe and the filling height — there is not a single simple effective viscosity in our fluid.

2.4.1 Equation of motion

As Fig. 2.3c suggests, the trajectory of a probe approaching the equilibrium depth is exponential in time. To make this more precise, we plot

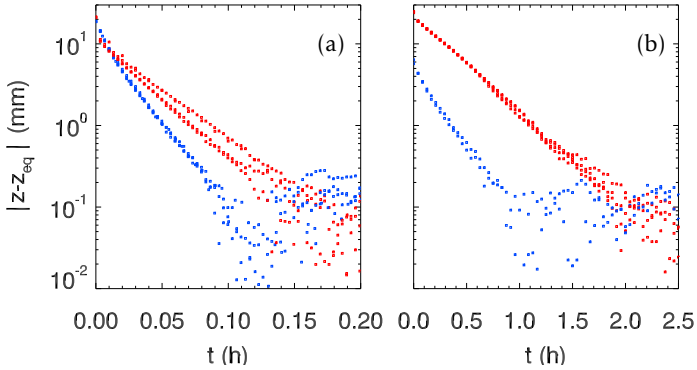

FIGURE 2.4: Log of $z - z_{eq}$ as a function of time. The approximately linear behaviour is suggestive of viscous drag. (a) $H = 60$ mm. (b) $H = 50$ mm. Red denotes experiments in which the probe sinks, while blue denotes experiments for which the probe rises.

the log of $z - z_{eq}$ vs time (Fig. 2.4). The linear nature of this relationship demonstrates the exponential character of the probe motion for both sinking and rising probes. Because the sum of the gravitational force and the buoyant force on the probe is proportional to $z - z_{eq}$, the exponential approach to equilibrium implies that the probe experiences a drag force proportional to its velocity: the probe experiences viscous drag.

The observation of Archimedes' law and of exponential probe trajectories close to equilibrium suggests that three forces act on the probe: gravity (mg), buoyancy ($\pi r^2 \rho g \frac{R_C^2}{R_C^2 - R^2}(H - z_{eq})$), and a dissipative force analagous to viscous drag, $2\eta R \frac{dz}{dt}$. Although Eq. (2.4) takes the corrections to the effective radius and variation of the packing density near the probe into account, these corrections are small and we will exclude them from our subsequent analysis.

If we assume that inertial effects can be ignored so that the motion of the probe is overdamped, it is possible to extend Eq. (2.3) to describe the motion of the probe away from equilibrium:

$$-Mg + \pi R^2 \rho g \frac{R_C^2}{R_C^2 - R^2}(H(0) - z(t)) - 2\eta r \frac{dz}{dt} = 0\,. \tag{2.5}$$

Determining viscosities

With the position of the probe as a function of time, $z(t)$, we can determine the viscosity as a function of the parameters M, R, Ω, H and z (Eq. (2.6). We can also determine whether the viscosity varies with the probe depth, z: there is no a-priori reason for the effective viscosity to be constant throughout the entire system. Although we previously observed that $z(t) - z_{eq}$ is exponential (Fig. 2.4), it is important to stress that the main implication of the *approximately* exponential form of this relaxation is that it rules out, for example, a power law relationship between the drag force and probe motion - in leading order, the drag force must be is linear in the probe speed. In fact, we do observe spatial gradients in η, although the variations are rarely larger than a factor of two over the entire trajectory of the probe and are much smaller than the variations in local strain rate (see Section 2.4.3).

To calculate the probe velocity, dz/dt, we numerically differentiate $z(t)$ over a time interval δ:

$$v(t) = (x(t + \delta/2) - x(t - \delta/2))/\delta \; . \tag{2.6}$$

The time scales of the motion of the probes vary by several orders of magnitude when M, R, H or Ω are changed. The total duration of each run is long enough to observe the probe until it is nearly submerged or until it is well equilibrated. The time interval δ is also adjusted to minimize noise: δ is proportional to the total duration of the data set.

The filling height of the sheared beads prior to the introduction of a probe ($H(0)$) is typically 1 to 2 mm larger than the static filling height. As described previously (Sec 2.2.1) this dilation can be measured by observing the position at which a light falling probe slows dramatically - the point at which the probe contacts the grains. For heavy probes the point at which the probe contacts the grains is harder to discern, so $H(0)$ is simply set to the static filling height, H, plus 1 mm.

Extracting reliable values of the viscosity close to the equilibrium depth of floating probes is complicated by two factors. First, fluctuations dominate the motion of the probe in this region: close to z_{eq}, both $v(t)$ and $z(t) - z_{eq}$ go to 0 and so the error in the viscosity, which is proportional to $(z(t) - z_{eq})/v(t)$ diverges. We therefore ignore the calculated viscosities within 1 mm of the equilibrium depth. Secondly, extracting reliable values of the viscosity close to equilibrium is only possible if the bead density

and filling height are such that the buoyant force and gravitational force are equal and opposite at equilibrium. To minimize this problem, we use the fitted value of z_{eq} (Eq. 2.8) to calculate the best estimate of the density. For probes too heavy to float in the grains, this problem does not arise and the measured density of 1.92 ± 0.05 g/cm^3 is used.

Sinking and Rising

Closer inspection of Fig. 2.3c suggests that for $H = 60$ mm, the probe appears to rise more quickly than it sinks. This is also apparent in the plots of $ln(z(t) - z_{eq}$ in Fig. 2.4a. (Note that near the equilibrium depth, $ln(z(t) - z_{eq}$ is very sensitive to the value of z_{eq}.) Surprisingly, the difference between sinking and rising probes appears to be less pronounced for $H = 50$ mm (Fig. 2.4b).

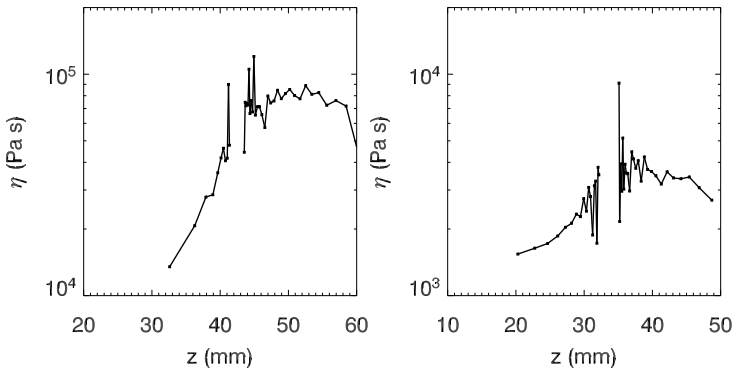

FIGURE 2.5: Viscosity as a function of probe position for filling height $H = 60$ mm (left) and $H = 50$ mm (right) for $\Omega = 0.1$ rps. The probe has a radius $= 20$ mm and mass 40 g.

To investigate the difference between the behaviour of rising and sinking probes, we plot the viscosity ($\eta(z)$) as a function of probe depth for $H = 50$ mm and $H = 60$ mm (Fig.2.5). For sinking probes which are light enough to float, we find that the viscosity is constant and independent of the probe depth. In contrast, the viscosities obtained for rising probes are not constant: the viscosity increases as the probe rises. As the rising probe nears the equilibrium depth, the viscosity approaches that experienced by the sinking probe.

Because the probe is never completely submerged in the grains, the processes of sinking and rising are asymmetric: a sinking probe compresses the grains below it, while a rising probe moves upward and allows the grains beneath to dilate. Because loosely-packed grains rearrange more easily than densely-packed grains, the motion of a sinking probe is impaired as the beads underneath the probe compact, while the motion of a rising probe is effected more easily as the beads under the probe dilate. In the remainder of this Chapter we will examine the motion of sinking probes.

2.4.2 How the viscosity depends on the ambient humidity, Ω, H, z, M and R

Because the drag force on a moving probe scale linearly with the probe speed, we are able to define an effective viscosity for the granular liquid. In this Section we describe the results of a series of experiments where we use the probe trajectory, $z(t)$, to determine the effective viscosity $\eta(z)$ for widely ranging values of the control parameters M, r, H and Ω. Unlike ordinary Newtonian fluids, where the viscosity is independent of the diameter and the mass of the sinking object, we find that the effective viscosity of our granular system depends on M and r.

The relationships between the viscosity and the control parameters are summarized here and and discussed in detail in the following Sections. First, we find evidence that the humidity and surface properties of the beads contribute to run-to-run variation in the probe trajectories, but do not have a significant effect on the viscosity. Second, we find that the viscosity scales as Ω^{-1} over several orders of magnitude (Section 2.4.2). We also find that the viscosity of the granular liquid depends on the filling height, H: increasing the amount of beads in the container strongly increases the viscosity of the beads. In addition, we observe that the viscosity varies weakly with the vertical position of the probe, z, and that the character of this variation depends on the filling height (Section 2.4.2). In Section 2.4.2 we investigate how the viscosity depends on the mass (M) and radius (R) of the probe. While it is not possible to vary the probe mass and radius over several decades, our observations are consistent with a scaling law: $\eta \sim R^4 M^{-2}$.

How the viscosity depends on ambient humidity

Since the humidity and the surface properties of the beads play a role in the microscopic interactions between individual particles, it is useful to investigate how these factors affect the viscosity of the system. However, the viscosity does not appear to depend systematically on the humidity (Fig. 2.6).

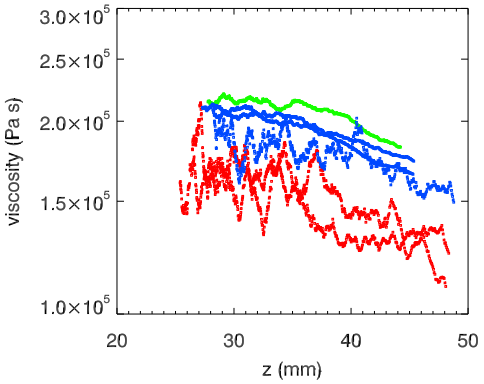

FIGURE 2.6: Changing the surface properties of grains by tuning the humidity or by smoothing the surface of the beads with long-term use has a weak effect on the viscosity observed by a sinking probe. Green: dry beads after long-term use. Blue: humid beads after long-term use. Red: humid, unused beads. All these experiments were conducted on the same day. ($H = 50$ mm, $R = 15$ mm, $M = 60$ g, $\Omega = 0.01$ rps)

The trajectory of the probe is smoother when old beads are used than when new beads are used. This is presumably because the new beads are rougher, while older beads (which have been used in the experiment for a long period of time) are smoother.

Viscosity scales inversely with the disk rotation rate

The observation that there is no probe motion when the disk is stationary invites questions about how the viscosity changes as the disk rotation rate is decreased. Is there a transition from liquid-like behaviour to solid-like behaviour at a small — but finite — disk rotation rate?

We have investigated this question by measuring the probe velocity for probes of different mass and diameter at different disk rotation speeds. We focus here on the speed of these probes in a small region ($10 > H - z > 15$ mm). As Fig. 2.7 shows, the probe velocity is proportional to Ω over a wide range of driving rates, irrespective of filling height, probe area and mass. Even when the probe is moved off-center the linear relationship between the probe velocity and Ω persists.

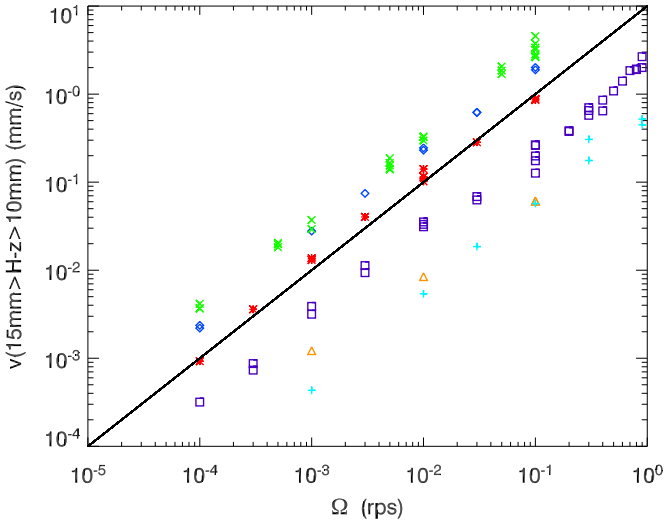

FIGURE 2.7: Probe velocity, $v(H - 15\text{mm} < z < H - 10\text{mm})$, as a function of disk rotation rate. Red $\star$: $H = 60$ mm, $M = 77$ g, $R = 9$ mm. Blue $\diamond$: $H = 50$ mm, $M = 46$ g, $R = 9$ mm. Purple $\square$: $H = 60$ mm, $M = 48$ g, $R = 9$ mm. Green $\times$: $H = 60$ mm, $M = 86$ g, $R = 9$ mm. Orange $\triangle$: $H = 60$ mm, $M = 46$ g, $R = 9$ mm with a probe immersed at a radius of 15 mm away from the center. Light blue $+$: $H = 70$, $M = 145$ g $R = 15$ mm. The black line denotes a linear relation.

Because the probe velocity is inversely proportional to the disk rotation speed over several orders of magnitude (Fig. 2.7), we conclude that the viscosity is inversely proportional to $\Omega : 1/\Omega$ selects the time scale for the probe motion. In other words, the displacement of a sinking probe only depends on the total strain applied, not on the strain rate: a probe will sink the same distance in one revolution of the disk, no matter how quickly the disk is moving.

How the viscosity depends on H and z

Adding grains to the container significantly increases the viscosity: increasing H by one centimeter increases the viscosity by an order of magnitude. Meanwhile, the viscosity varies weakly with the depth: in Fig. 2.8 we plot $\eta(z)/\eta(H - 5 \text{ mm})$ for filling heights of $H = 50$, 60 and 70 mm. For $H = 50$ mm, the viscosity is larger when the probe is closer to the rotating disk than at the surface, while for $H = 70$ mm, the viscosity is larger when the probe is closer to the surface than near the rotating disk. Meanwhile, the viscosity is fairly constant for all depths reached by the probe at a filling height of $H = 60$ mm.

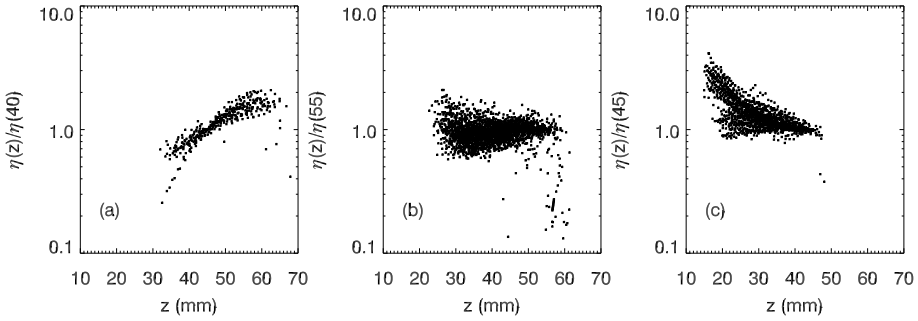

FIGURE 2.8: Rescaled viscosities for different filling heights. (a) $\eta(z)/\eta(40)$, $H = 70$ mm. (b) $\eta(z)/\eta(55)$, $H = 60$ mm. (c) $\eta(z)/\eta(45)$, $H = 50$ mm.

Note that the heaviest probes experience the greatest viscosity increase as they sink in a system with $H = 50$ mm. This might indicate that the heavy probes are compressing the grains in the region directly above the spinning disk, making it more difficult for the grains beneath the probe to evacuate and allow the probe to sink. Conversely, at $H = 70$ mm, the viscosity for light and heavy probes is slightly greater at the surface than deeper in the material. Note that at $H = 70$ mm, a probe with a length of 4 cm cannot probe deeper than $z = 30$ mm - well above the dome of beads co-rotating with the disk. At $H = 70$ mm, a probe nears the shear band as it sinks: if the shear band generates the fluctuations which causes the grains to fluidize then a probe might be expected to experience a lower viscosity closer to the shear band than at the surface. Testing these hypotheses requires information about how individual particles move - a measurement might be accomplished with a 3D scanner.

Because the way that the viscosity changes as a function of depth for $H = 60$ and 70 mm is the same for all probe masses and radii, we can express the viscosity as the product of separable functions which depend on the experimental parameters: $\eta = (1/\Omega)\ F(H, z)\ G(M, r)$. For $H = 60$ mm, F is essentially a constant for all z, while for $H = 70$ mm it only varies over a factor of two. Because the viscosity increases more for heavy probes than for light probes as they sink from the surface at $H = 50$ mm, we cannot express the viscosity as a product of separable functions. Since the probe is well within the shear band as it when it is nearly submerged at $H = 50$ mm, we will focus our subsequent analysis on the behaviour of probes at larger filling heights.

How the viscosity depends on M and R

In this Section we explore how the effective viscosity varies with the mass and radius of the probe for $H = 60$ and $H = 70$ mm. We find that the viscosity decreases strongly with M and increases strongly with R. During experiments in which we examine how the viscosity is affected by M and R, we select disk rotation rates (Ω) such that the probes do not not require onerous amounts of time to sink. Because the viscosity is known to scale as $1/\Omega$ (Section 2.4.2), we can compare runs at different rotation speeds by examining the product $\Omega\eta$.

Examples of $\eta(z)$ for a range of masses are given in Fig. 2.9a ($H = 60$ mm) and Fig. 2.9d ($H = 50$ mm). Since η does not vary strongly with z for $H = 60$ mm, we can plot the rescaled viscosities $\Omega\eta(z = H - 20$ mm) as a function of M for different probe radii (Fig. 2.9b,e). Although there clearly is substantial scatter in the data, and the range of M is limited, the relationship between the viscosity and the probe mass is consistent with a simple scaling law: $\Omega\eta \sim M^{-2}$.

It is difficult to measure how the viscosity depends on the probe radius because the probes must be smaller than the container and bigger than the grains. As Fig. 2.9b,e demonstrate, measurements for probes with $9 < R < 30$ mm suggest that the relationship between the viscosity and probe radius is consistent with a power law where the viscosity is proportional to R^4.

Since the viscosity is roughly proportional to M^{-2} and R^4, the viscosity experienced by sinking probe appears to scale inversely with the square of the pressure exerted by the probe: for $H = 60$ mm, $\eta \approx 1.9 \times$

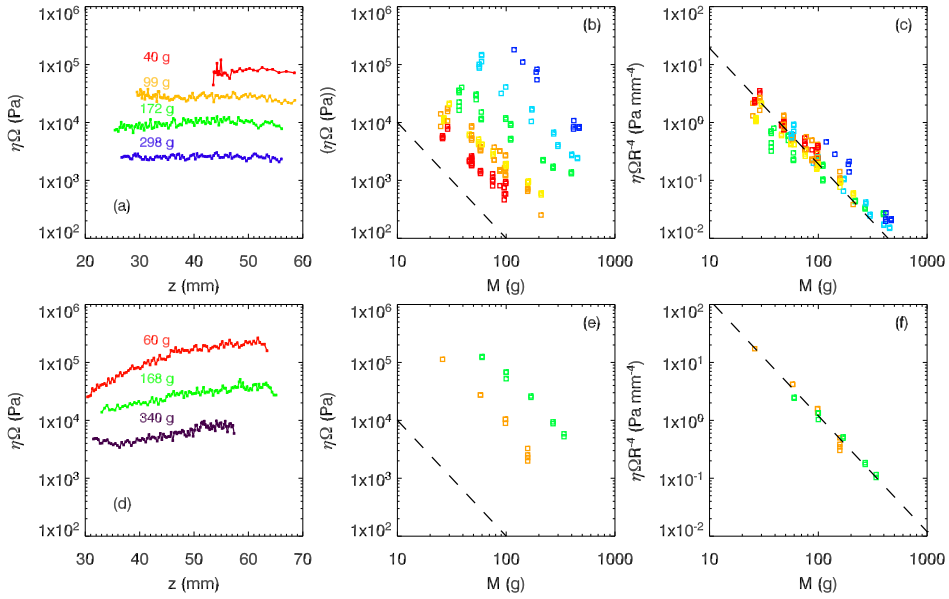

FIGURE 2.9: Scaling of the viscosity with M and R. (a-c) $H = 60$ mm. (a) $\eta(z)$ for a range of probe masses for $R = 20$ mm. (b) Rescaled viscosity $\Omega\eta(z = H - 20)$ as a function of mass for several probe radii (red: $R = 7$ mm; orange: $R = 9$ mm; yellow: $R = 10$ mm; green: $R = 15$ mm; cyan: $R = 20$ mm; blue: $R = 25$ mm). In panels (b), (c), (e) and (f) the dashed line is a guide to the eye and has slope -2. (c) The rescaled viscosity, $\Omega R^{-4}\eta(z = H - 20)$, scales as $(1.9 \times 10^3 \pm 7 \times 10^2)$ Pa/mm$^4 M^{-2}$. (d-f) $H = 70$ mm. (d) $\eta(z)$ for a range of probe masses for $R = 25$ mm. (e) Rescaled viscosity $\Omega\eta(z = H - 20)$ as a function of mass for a range of R (same colours as panel (b)). (f) The rescaled viscosity, $\Omega R^{-4}\eta(z = H - 20\text{mm})$, scales as $(1.2 \times 10^4 \pm 3 \times 10^3)$ Pa/mm$^4 M^{-2}$.

$10^3 \pm 7 \times 10^2$ Pa g^2/mm^4 $\Omega^{-1} m^{-2} r^4$, while for $H = 70$ mm, $\eta = 1.2 \times 10^4 \pm 3 \times 10^3$ Pa g^2/mm^4 $\Omega^{-1} m^{-2} r^4$ (Fig. 2.9c,f).

Using the motion of sinking probes, we have measured the viscosity of a granular system excited by shear. We find that the viscosity increases as the filling height of the grains in the container is increased. The viscosity is of a sinking probe is constant for $H = 60$ mm and decreases slightly as the probe sinks in a system with $H = 70$ mm. The viscosity experienced by a sinking object can be related to the mass and radius of the object and the rotation rate of the disk with a simple power law: $\eta \propto \Omega^{-1} r^4 m^{-2}$.

2.4.3 Does the local flow rate set the viscosity?

Even though the flow at the surface is very slow, it is not zero [13], [16], [50]. It is therefore natural to ask whether the probe motion is determined by the local strain rate or the flow rate near the probe. We can examine this question by comparing the way in which the local flow and strain rates vary with r and z to the spatial variation of the effective viscosity.

We focus first on the case of probes immersed in the center ($r = 0$) of the system and examine how the flow speed varies with z and H. For dome-like shear bands, the strain in the region above the center of the disk is torsional [16], and so the strain rate varies as $(\partial_z \omega|_{r=0})$. In Fig. 2.10 we compare the viscosities and local strain rates.

We measure the precession rate, $\omega_p(z) := \omega(z)|_{r=0}/\Omega$, by inserting a vane in the center of the grain flow and observing the rotation of the probe with an Anton Paar DSR 100 rheometer. The vanes consist of four rectangular blades of height 10 mm and radius 5 mm mounted on a smooth rod. By removing the blades from this rod we have established that the torques exerted on the rod are two orders of magnitude smaller than those exerted on the vane, guaranteeing that the measured rotation of the vane corresponds to the flow near the vane and is insensitive to the rest of the rod which is submerged in the grains. In addition, we find that varying the dimensions of the vane does not result in any systematic changes in the measured precession rates.

The resulting vane precession rates, $\omega_p(z)$, for $H = 50, 60$ and 70 mm (Fig. 2.10a) are in reasonable qualitative agreement with earlier MRI measurements and simulations [16]. Because our measurements of the precession rates are made over a larger range than previous measurements, we can establish that $\omega_p(z)$ approaches the surface precession rate, $\omega_p(z = H)$, more quickly than an exponential but more slowly than a Gaussian. The resulting flow profiles are described by an expression of the form

$$\omega_p(z) - \omega_p(z = H) = \omega_p(z = 0) \exp(-(z/\xi)^{1.5}) \,, \tag{2.7}$$

where $\omega_p(z = 0)$ captures slip near the bottom disc and the characteristic length scale ξ is on the order of 10 mm.

The strain rates $(\partial_z \omega|_{r=0})$ are plotted in Fig. 2.10b. Data obtained by numerically differentiating the measured ω are indicated by individual points, while the curves are obtained by directly differentiating the fit in Eq. (2.7). These two estimates for the strain rate are in excellent agreement

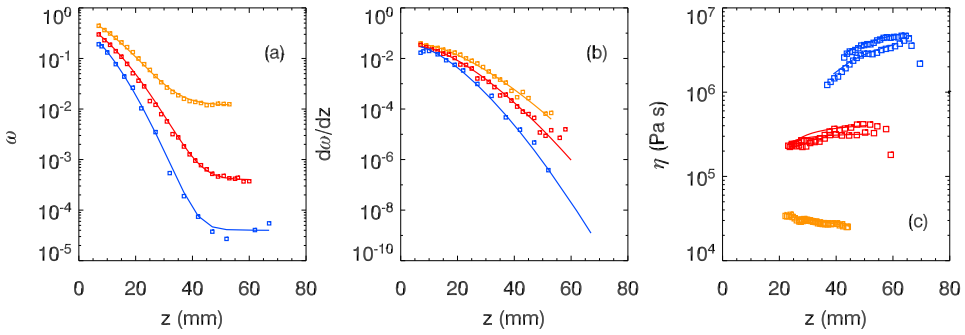

FIGURE 2.10: (a) ω_p as a function of the height above the spinning disk. Curves are of the form $\omega_p(z) - \omega_p(z = H) \sim \exp(-(z/\xi)^{1.5})$, with $\xi = 9.5, 11.5$ and 13 mm respectively. Note that the plateaus in $\omega_p(z)$ for $z \to H$ correspond to the precession rates measured at the free surface using video imaging [15]. (b) The corresponding variation of the strain rate ($\partial_z \omega_p$) with z for $H = 50, 60$ and 70 mm. (c) Viscosity as a function of probe position for a probe with $M = 59$ g, $R = 15$ mm and $H = 50, 60$ and 70 mm (lower orange curve, middle red curve and upper blue curve respectively).

and demonstrate that the local strain rate decreases by several decades as the probe is moved from the disk to the surface of the grains.

In Fig. 2.10c we show three examples of the local viscosities for a single probe at filling heights of 50, 60 and 70 mm. Clearly the local strain rate and $\eta(z)$ are very poorly correlated: the local strain rate changes over four decades for $H = 70$ mm, while $\eta(z)$ changes over less than half a decade. This suggests that the liquid-like behaviour of a granular system fluidized by shear is not caused by local flow near a sinking object.

What happens when the probe is moved from the center of the setup?

We have also examined how the viscosity is affected by moving the probe away from the centre of the setup. Away from the centre, the material continues to behave as a viscous fluid and demonstrates no yield stress; however, the effective viscosity increases away from the centre of the cell. This is illustrated in Fig. 2.7 where we compare the velocity of a sinking probe of radius 9 mm in the center of the system to the velocity of an identical sinking probe displaced 15 mm from the centre: the sinking speed of the latter probe decreases by about a factor of four.

That the local flow speed *increases* with the radial distance, r, while the viscosity experienced by a sinking object *decreases* with r suggests that the local flow past the probe is not the cause of the fluid-like behaviour.

In conclusion, we find that neither the local strain rate nor the local rate of flow past the probe are strongly correlated to the observed effective viscosity. This suggests that source of fluidization is non-local: the strain rate in one location (in the shear band) governs the effective viscosity of the granular materials far from the shear band.

2.5 Conclusion

In this Chapter we have measured some of the macroscopic properties of a granular system excited by shear. We find that although this system has many of the properties of a liquid, it also exhibits some behaviours which are are inconsistent with those of a Newtonian fluid. Finally, our measurements of local flow and local viscosity are not strongly correlated, which suggests that local strain does not cause the liquid-like behaviour of our system.

By comparing the equilibrium depth of a low-density object rising in the grains to the equilibrium depth of that same object sinking in the grains, we have demonstrated that our granular liquid does not exhibit a yield stress. We have also observed that the equilibrium depth can be predicted by Archimedes' rule.

In addition to examining the equilibrium behaviour of the floating probe, we have found that a moving probe experiences viscous drag. We have determined the viscosity of our granular liquid by measuring the vertical position of a sinking object as a function of time. We find that the viscosity of the liquid is inversely proportional to the disk rotation rate and that increasing the filling height of the beads in the container increases the viscosity.

The viscosity of the system can also be measured with a rheometer or by dragging a probe laterally through the grains. Reddy et. al. [60] recently performed the latter measurement by observing the force required to drag a rod through grains excited by shear in a Couette cell. Unlike in our experiment, they find that the velocity of the rod scales exponentially with the force on the rod. However, the motion of their probe is parallel or anti-parallel to the flow in the system, while in our experiment the

motion of the probe is perpendicular to the flow. In addition, the probes in these experiments are much smaller than the sinking objects in our experiments, so it is perhaps not unsurprising that different behaviour is observed.

We have observed two unliquid-like behaviours in our granular system: although the viscosity of a real liquid is independent of the diameter and the mass of the sinking object, we find that the viscosity of our granular system varies with the mass and diameter of the probe. Our observations suggest that the way the viscosity depends on the probe mass and radius can be described by a power law: $\eta \propto R^4 M^{-2}$. The viscosity is inversely proportional to the pressure exerted by the probe.

An additional unliquid-like characteristic of our granular medium is that the viscosity experienced by a rising probe is slightly smaller than the viscosity experienced by a sinking probe. Perhaps this occurs because the grains have more difficulty rearranging when they are compressed by a sinking probe than when they dilate under a rising probe.

Finally, we have endeavoured to develop a deeper understanding of the fluidization mechanism by observing the local flow rate in the grains using a rheometer. We have demonstrated that the viscosity not determined by the local flow rate.

In this Chapter we have explored some of the bulk properties of our granular liquid. However, we still don't have a *microscopic* understanding of why our system has many of the characteristics of a fluid. One way to investigate the microscopic behaviour of the grains is suggested by the observation that a floating probe does not sit statically at the equilibrium depth, but instead fluctuates in a manner reminiscent of Brownian motion. We will explore the characteristics of these fluctuations in Chapter 3.

2.6 Appendix: Fitting the probe position as a function of time

Although the solution to Eq 2.3 is an exponential (Fig.2.11), plotting the velocity as a function of time suggests that the probe initially sinks more quickly than expected. This can be modelled by introducing a second exponential into the fit. This fit is useful for extracting the equilibrium depth, z_{eq}.

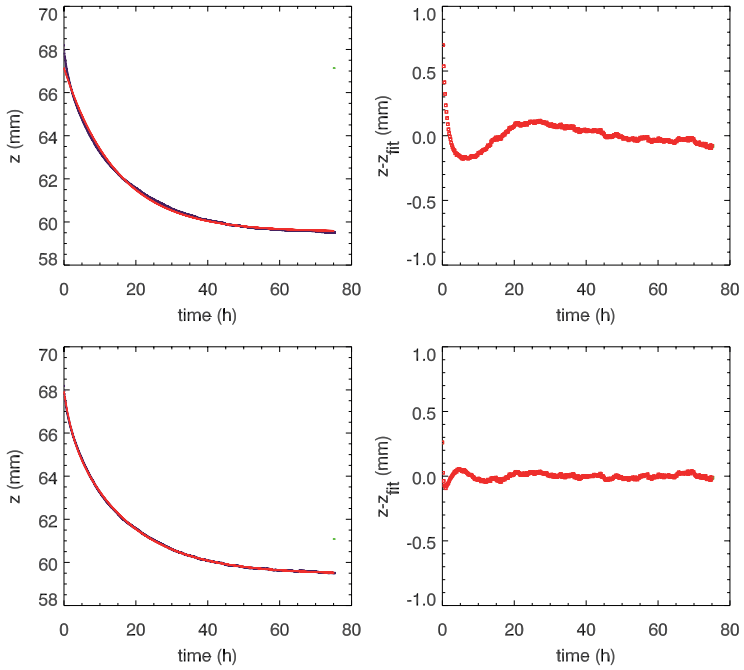

FIGURE 2.11: The fit to two exponentials (lower panels) describes the behaviour at early times better than the fit to one exponential (upper panels). The raw data and the fits are displayed in the left-hand panels and the residuals are plotted in the right-hand panels. ($H = 65$ mm, $\Omega = 0.1$, $M = 36$ g, $R = 25$ mm.

$$z(t) = a_1 e^{-k_1 t} + a_1 e^{-k_1 t} + z_{eq} \tag{2.8}$$

Chapter 3

Fluctuations in a granular liquid

3.1 Introduction

In the previous Chapter we found that shearing a container of glass beads with a spinning disk in the bottom of the vessel creates a system with many of the bulk characteristics of a regular liquid. Because the viscosity does not vary with the local precession speed of the grains, we proposed that *fluctuations* - and not *local flow* - are responsible for causing the liquid-like behaviour of the grains. The fluctuations in our granular liquid are also interesting because their presence suggests an analogy with the Brownian motion of particles in a real liquid. At the *macroscale* the properties of our granular system are liquid-like - sinking objects experience viscous drag and floating objects obey Archimedes' rule. Studying the fluctuations will allow us to determine if the system also behaves like a liquid at the *microscale*.

Because we hypothesize that the liquid-like behaviour of our sheared granular system is due to fluctuations, we will characterize these fluctuations in terms of the parameters (filling height, disk rotation speed, probe mass, probe radius, probe depth) which set the apparent viscosity of the material. The primary problem is therefore to understand what characterizes fluctuations in our granular system, while the secondary problem is to determine what role the fluctuations play in setting the bulk characteristics of the material.

We can probe the fluctuations in the grains by observing the position of a floating probe, which follows a trajectory, $z(t)$. If the probe motion is analagous to Brownian motion, then the distribution of the size of the displacements of the floating probe, $\Delta z(\Delta t)$, for a time interval, Δt, will have a Gaussian distribution. (Note, however, that a Gaussian distribution does not imply Brownian motion.) A second signature of Brownian motion is that the mean square displacement, $< \Delta z^2(\Delta t) >$, is proportional to Δt. The mean square displacement and the distribution of the probe

displacements are therefore useful for determining if the fluctuations of the probe are Brownian - and liquid-like - in character.

Granular systems excited by shear [42] and vibration [61] have also been found to exhibit behaviours typical of glasses. On the macroscopic scale, glassy systems typically exhibit a yield stress and have bulk properties - such as the viscosity - which depend on the history of the system [62]. Our sheared granular liquid demonstrates no history-dependent properties and there is no yield stress, but because other granular systems exhibit glassy behaviour it is still instructive to inquire whether our system has any of the microscopic characteristics of a glass. At short length scales in a glass, the formation of particle "cages" causes the distributions of particle displacements to develop fat, non-Gaussian tails. In addition, fluctuations of particles in a glass may also be subdiffusive [35]. Examining both the distribution of the size of the displacements of the fluctuating probe and the mean square displacement curves will allow us to determine if the fluctuations are like those in a liquid or like those in a glass.

We have found that the distribution of $\Delta z(\Delta t)$ is Gaussian for a wide range of Δt, though for large Δt the distribution may narrow slightly. We have also found that the mean square displacement curves are diffusive or nearly-diffusive on short time scales at low filling heights (where there is flow at the surface of the grains), but that the probe motion becomes subdiffusive at larger filling heights (where there is very little flow at the surface). Interestingly, the presence of Gaussian PDFs *and* subdiffusive behaviour is characteristic of neither a glass nor a simple liquid!

Another surprising result is that the mean square displacement curves are suppressed and become more subdiffusive as the filling height, H, increases. However, the slopes of different parts of the mean square displacement curve are not modified by changing the mass of the probe or by moving the probe away from the equilibrium depth. Although the diffusive character of the mean square displacements is unchanged when the probe is away from equilibrium, we also find that the fluctuations are slightly smaller in amplitude compared to when the probe is floating. The variation of the amplitude of the fluctuations with the position of the probe is comparable to the variation of the viscosity with position.

One robust feature of the mean square displacement curves is the appearance of a plateau at long time scales. Although the motion of our probe is subdiffusive, the presence of a plateau suggests that the motion

of the probe is analogous to that of a random walker in a harmonic potential - a situation described by the Ornstein-Uhlenbeck theorem. Our floating probe is moving in a potential well given by the sum of the buoyant and gravitational forces acting on the probe. In concordance with the behaviour expected for a random walker in such a potential well, we find that the magnitudes of the plateaus in the mean square displacement curves are independent of the probe mass and proportional to the probe area.

Finally, the time scale at which the mean square displacement saturates and the plateau begins depends on filling height and disk rotation speed. We observe that the mean square displacement curves can be rescaled by the viscosity so that the beginnings of the plateaus overlap. This indicates that the characteristic time scales of the fluctuations and the viscosity are the same.

This Chapter – In order to characterize the fluctuations in our sheared granular system, we examine both the distribution of the size of the displacements of the fluctuating probe over different time intervals (Section 3.2.1) and the mean square displacement of the floating probe (Section 3.2.1). We use the mean square displacement and probability distribution function to study the relationship between the fluctuations and several experimental parameters - the filling height (H), disk rotation speed (Ω), probe mass (m), probe radius (r) and probe position, (z) (Section 3.3). Finally, we explore how the fluctuations are generated (Section 3.6).

3.2 Describing the fluctuations

Since the trajectory of the probe, $z_{raw}(t)$, away from z_{eq} is dominated by the sinking motion of the probe, $z_{sink}(t)$, probing the fluctuations is best accomplished when the probe is floating at or near the equilibrium depth. Away from equilibrium it is necessary to subtract off the decay envelope due to the viscous sinking process (Fig. 3.1). (Note that if the sinking envelope is slightly incorrect then distribution of probe displacements, $\Delta z = z(t + \Delta t) - z(t)$, will no longer be centred at 0 mm. This can be observed for distributions with large Δt in Fig. 3.2.) In addition, a characteristic oscillation, $z_{osc}(t)$, with typical amplitude of order 0.1 mm occurs at the disk rotation frequency. This oscillation is due to small misalignments between the spinning disk and the probe and can be filtered out.

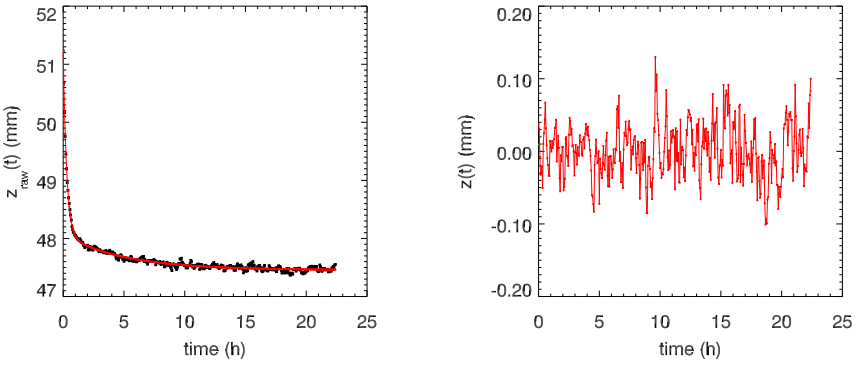

FIGURE 3.1: Analysis of a typical fluctuation data set. Left: probe position as a function of time with fit. Right: the fluctuations are given by the difference between probe position and fit.

The fluctuation signal is therefore given by:

$$z(t) = z_{raw}(t) - z_{osc}(t) - z_{sink}(t) \tag{3.1}$$

Once the fluctuations have been isolated from the raw signal, the probability distribution function, mean square displacement and power spectra can be computed. Details concerning how the fluctuations and mean square displacement curves are calculated are included in Section 3.5.

3.2.1 Parameterizing the fluctuations using the probability distribution function

One way of describing the fluctuations of the floating probe is with the probability distribution function (PDF) - the distribution of the displacements of the particle, $z(t + \Delta t) - z(t)$, for a given time step, Δt. Glassy behaviour is typified by PDFs which are non-Gaussian - the PDFs develop "fat tails" [35]. This is in contrast to a particle undergoing Brownian motion, for which the PDF is Gaussian. It is also worth noting that although the PDFs of Brownian particles are Gaussian, Gaussian PDFs do not imply that Brownian motion is occurring.

The distribution of $\Delta z(\Delta t)$ is plotted in Fig. 3.2. The distributions have been fitted to a Gaussian (on a linear scale), so any deviations from Gaussianity may be identified. The distributions are Gaussian at small

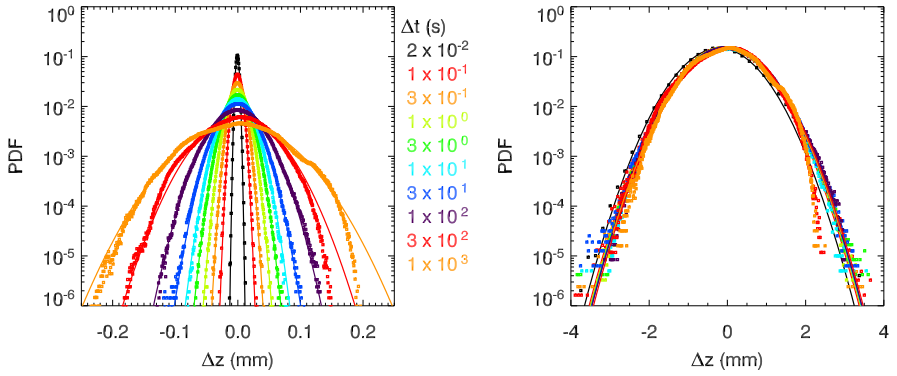

FIGURE 3.2: Left: Distribution of displacement sizes for different time steps ($\Delta z(\Delta t)$). The data are for a probe with $R = 25$ mm and $M = 30$ g floating in grains with filling height $H = 55$ mm and driven at $\Omega = 0.1$ rps. The data set is 11.6 h in duration and there are 0.02 s per data point. The PDF contains $6.7 \times 10^{-}4$ mm/bin. Right: the PDFs rescaled by their width and height. The resulting distributions are Gaussian and the only deviations from Gaussianity occur for $\Delta t \geq 300s$ where the distributions are slightly narrower than a Gaussian for large displacements.

times and sometimes become slightly narrower than Gaussian at larger times: we do not observe the broad tails typical of a glass.

3.2.2 Parameterizing the fluctuations using the mean square displacement

In order to determine whether the vertical fluctuations of the floating probe are Brownian - and therefore liquid-like in character - it is useful to calculate either the mean square displacement (MSD) or the Fourier transform of the trajectory of the floating probe.

For Brownian motion, the mean square displacement, $\langle|\Delta z(\Delta t)|^2\rangle$, scales linearly with Δt and inversely with the viscosity of the system (η) and the radius of the probe (r):

$$\langle|\Delta z(\Delta t)|^2\rangle = \frac{k_B T}{2\eta r}\Delta t \tag{3.2}$$

In a granular system, $k_B T$ does not correspond to a thermal temperature - but it could be interpreted as a parameter which describes the en-

ergy scale of the motion of the particles in the system. However, for subdiffusive behaviour (in which $|\Delta z(\Delta t)|^\alpha \propto \Delta t$, with $0 < \alpha < 2$) the units of $\frac{k_B T}{2\eta r}\Delta t$ are no longer consistent with the units of $< |\Delta z(\Delta t)|^\alpha >$. It is therefore not clear how to define a granular temperature for a subdiffusive system by determining $k_B T$ from a diffusion equation.

The mean square displacement curve is also useful for identifying glassy behaviour in a system. Unlike a simple liquid, which is diffusive for all time scales, the MSD curves for a glass are typically subdiffusive and exhibit different power-law behaviour at different time scales [35].

A typical mean square displacement curve for the fluctuating probe is given in Fig. 3.3. At short time scales (0.1 - 1000 s) the system is subdiffusive and does not exhibit a well-defined power law. At longer time scales there is a white noise plateau - this plateau is expected because the probe is "walking" in a potential well given by the gravitational force and the buoyant force on the probe. The plateau occurs at around 2×10^{-2} mm^2 - which is consistent with the size of the square of the largest fluctuations in $z(t)$ in Fig. 3.2.

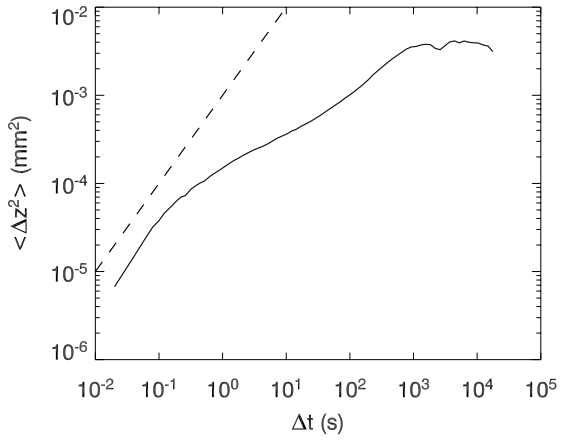

FIGURE 3.3: A typical mean square displacement curve for a system with $H = 55$ mm, $R = 25$ mm, $M = 30$ g, and $\Omega = 0.1$ rps. The dashed line indicates the power law prescribed by diffusive behaviour ($\langle|\Delta z(\Delta t)|^2\rangle \propto \Delta t$).

The mean square displacement is a valid measure of the probe motion in regimes where the distribution of the probe displacements is symmetric with a mean of 0 - if the PDFs are well-centred, then the mean square displacement indicates the variance of the PDF. However, if the peak of the distribution is shifted away from 0, then the mean square displacement no longer measures the variance of the distribution. The PDFs are therefore

useful for determining if the mean square displacement is a valid measure of the average displacement of the probe for a given time step. The PDFs are typically well-centred at short time scales (Fig. 3.2) and continue to be well-centred at long time scales if the system is well-equilibrated.

For experiments at low filling heights ($H < 60$ mm), the plateau in the MSD curve at long time steps extends over more than a decade (Fig. 3.3). However, since the PDFs are only weakly non-Gaussian, it is difficult to ascertain a correlation between the beginning of the plateau in the MSD curve and the appearance of non-Gaussian behaviour in the PDFS.

In the following Section (3.3), we will examine the effect of the filling height, H, disk rotation speed, Ω, probe mass, m, probe radius, r, and probe position, z, on the mean square displacement.

3.3 Tuning the fluctuations with experimental parameters

In the previous Section we demonstrated that the mean square displacement is a useful tool for describing the fluctuations in our granular liquid. Now we will use the mean square displacement to study how the fluctuations are influenced by experimental parameters such as the disk rotation rate, Ω, the filling height, H, the probe mass, m, the probe radius, r and the vertical position of the probe, z. We will also examine how the fluctuations and the viscosity (as measured in Chapter 2) are related. Finally, we will study how different features of the mean square displacement curve can be described with the Ornstein-Uhlenbeck theorem for a random walker in a potential well.

3.3.1 Tuning the fluctuations by changing the disk speed

In the previous Chapter, we found that the viscosity of our granular system scales inversely with the disk rotation rate, Ω. Since the mean square displacements of a probe particle in a liquid scale inversely with the viscosity (Eq. 3.2) and the viscosity is inversely proportional to Ω, we expect that the mean square displacement curves should scale with Ω.

We find that all regions of the mean square displacement curves scale with Ω at filling heights of $H = 50$ and $H = 55$ (Fig. 3.4). However, at larger filling heights the agreement at short time scales becomes poorer.

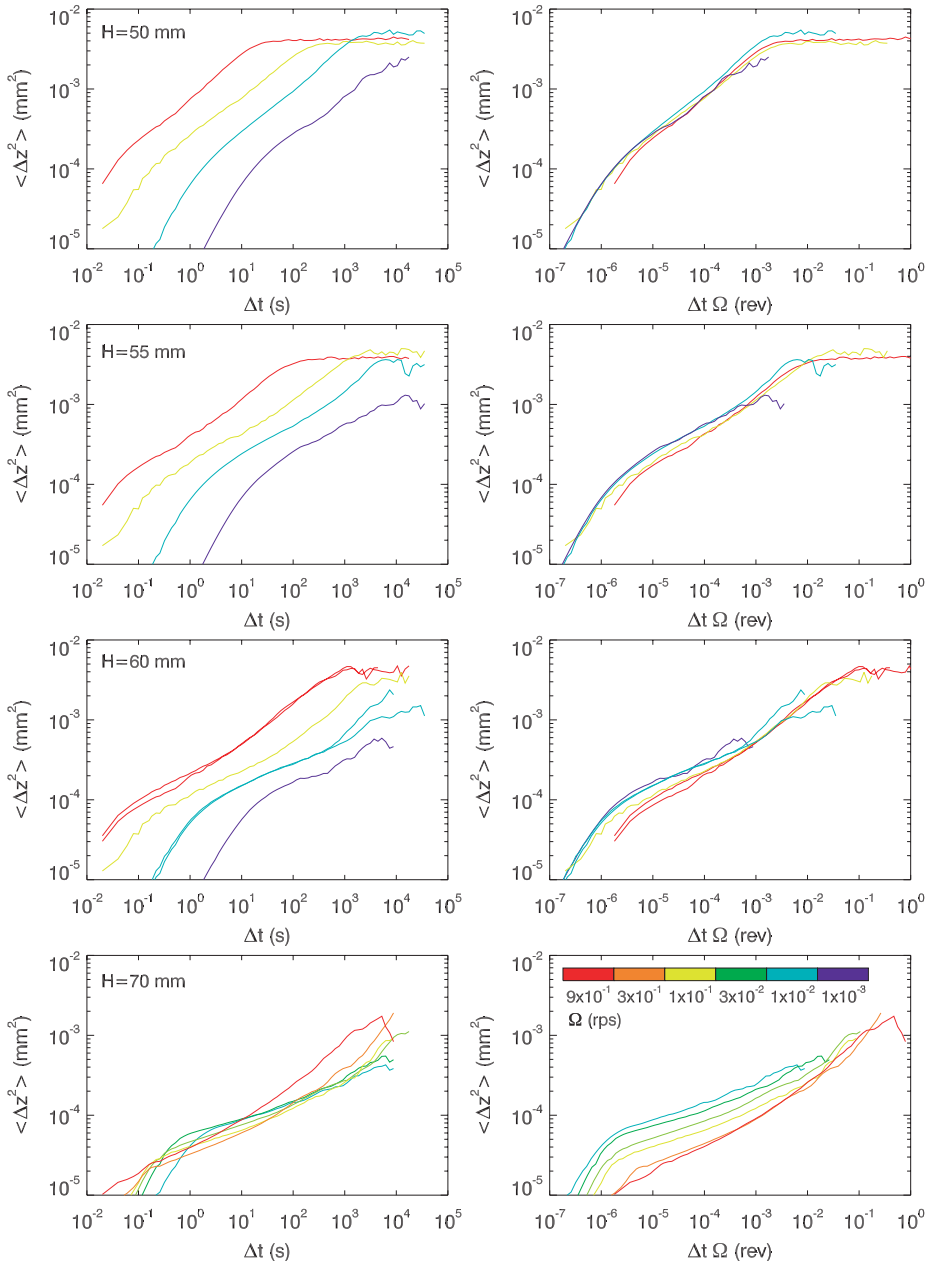

FIGURE 3.4: Mean square displacement curves for different disk rotation speeds. Top panels: $H = 50$ mm, $R = 25$ mm, $M = 56$ g. Middle panels: $H = 55$ mm, $R = 25$ mm, $M = 56$ g. Lower panels: $H = 60$ mm, $R = 25$ mm, $M = 36$ g. Bottom panels: $H = 70$ mm, $R = 25$ mm, $M = 36$ g.

3.3.2 Tuning the fluctuations by changing the filling height

The mean square displacement curves for systems with different filling heights are compared in Fig. 3.5. There are three main regions of the mean square displacement: a short time-step regime in which the fluctuations are diffusive; a longer time-step regime in which the fluctuations are subdiffusive; and, at very long time-steps, a plateau. For low filling heights ($H = 35, 40$ mm) the behaviour is diffusive or nearly diffusive for all time steps shorter than those on which the plateau is apparent. Subdiffusive behaviour begins to emerge at short time scales for systems with larger filling heights. The presence of diffusive behaviour at low filling heights appears to be related to the fact the a system with a filling height of $H < 45$ mm has a significant amount of flow at the surface - for low filling heights the shear bands extend to the surface.

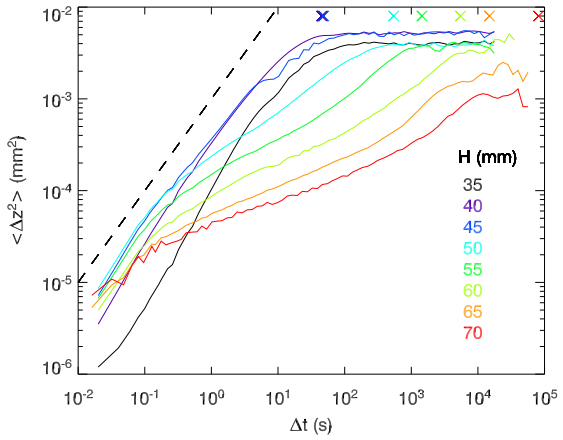

FIGURE 3.5: Mean square displacement curves for filling heights of $H = 35$ mm to $H = 70$ mm. The crosses ($\times$) above the curve correspond to the viscosity rescaled by a pressure, η/P_0, with $P_0 = 500$ N/m^2 . The dashed line indicates the power law prescribed by diffusive behaviour ($\langle|\Delta z(\Delta t)|^2\rangle \propto \Delta t$). ($M = 30$ g, $R = 25$ mm)

In order to compare the time scales of the fluctuations to the time scales of the viscosities, the viscosities can be rescaled by a pressure. The rescaled viscosities of the sinking probe ($R = 25$ mm, $M = 30$ g) are plotted above the mean square displacement curves for the fluctuations experienced by the same probe (Fig. 3.5). The viscosity is calculated as in Chapter 2 by determining the viscous drag force from the grain density, the probe position and the probe velocity. The indicated viscosity is the mean of the viscosity determined in the region between 1 and 3 mm above the equilibrium depth. For data sets which are well-equilibrated and do

not include the probe sinking outside of this region, a second measurement of the sinking motion is used to determine the viscosity.

In the diffusion equation (Eq 3.2) the mean square displacement is inversely proportional to the viscosity. It is therefore interesting to rescale the time-scale axis of the MSD curves by the *viscosity* observed for the floating probe.

In Fig. 3.6 the MSD curves are rescaled by the viscosities determined from the sinking probe trajectories. When the time scale axis of the MSD curves is rescaled by the viscosity, the regions just before the beginning of the plateau overlap. This suggests that the time scale of the viscosity matches the time scale of the plateau of the fluctuations.

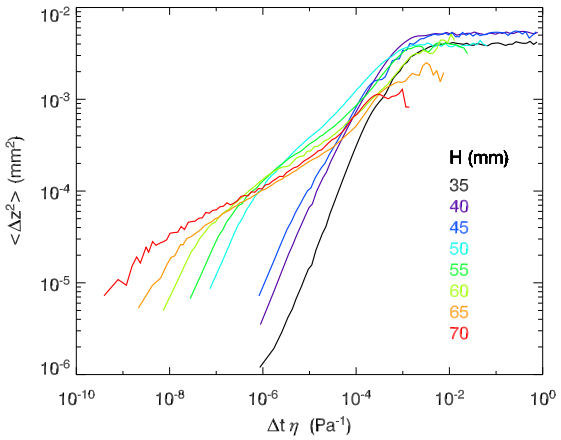

FIGURE 3.6: Mean square displacement curves for filling heights of $H = 45$ mm to $H = 70$ mm. The horizontal axis is rescaled by the viscosity. ($M = 30$ g, $R = 25$ mm)

Note that in the previous Section we found that rescaling the time axis of the MSD curves by the disk rotation speed caused the curves to overlap at longer time scales. Since the viscosity is inversely proportional to the disk rotation speed (Chapter 2, Fig. 2.7), rescaling the time axis by Ω is akin to rescaling by the inverse viscosity. Also note that when we rescaled the MSD curves by the disk rotation speed (Fig. 3.4), the curves at lower filling heights ($H \leq 60$) overlapped at all time scales, while at larger filling heights the overlap was stronger at longer time scales closer to the beginning of the plateau. Both these observations suggest that the time scale at which the plateau appears is important in determining the viscosity.

3.3.3 Tuning the fluctuations by changing the probe depth

There are two questions that can be examined by studying how the fluctuations depend on the probe depth. First, we enquire if the fluctuations change when the probe is moved away from the equilibrium position described by Archimedes' Rule. This allows us to determine if fluctuations in equilibrium are the same as fluctuations out of equilibrium. The second question we will explore concerns the observation that the hotter region of a material is the part closest to a heat source: since the spinning disk and shear band cause excitations in the system we might expect the system to undergo larger fluctuations closer to the spinning disk. We therefore examine how the fluctuations change as the probe is moved away from the excited particles in the shear band.

Profiling the fluctuations away from equilibrium can be accomplished at larger filling heights where the probe sinks slowly. The mean square displacements can be computed once the probe trajectory is subtracted off, as described in Section 2.6. One interesting feature of the distributions of $\Delta z(\Delta t)$ for the probe away from the equilibrium is that they are Gaussian (Fig. 3.7, Fig. 3.8). The Gaussian character indicates that away from the equilibrium predicted by Archimedes' Rule, the system behaves as though it is in a dissipative analog to thermodynamic equilibrium - a Non-Equilibrium Steady State.

The mean square displacement of different segments of the probe path as the probe rises or sinks towards equilibrium are plotted for $H = 70$ mm (Fig. 3.8) and $H = 60$ mm (Fig. 3.7). Comparing the PDFs of different segments of the probe fluctuations after the decay envelope is subtracted for $H = 70$ mm (Fig. 3.8) indicates that the fluctuations are slightly larger close to equilibrium than they are farther away - a result consistent with the mean square displacement curves (Fig. 3.8). However, at $H = 60$ mm (Fig. 3.7) the MSD curve for the region where the probe is above the equilibrium is slightly smaller in magnitude than the MSD curves for the equilibrated situations. In addition, the PDF for the probe above the equilibrium depth is not distinguishable from the PDFs for the equilibrated cases.

Interestingly, the different ways in which the fluctuations vary with the probe depth at $H = 60$ mm and $H = 70$ mm is consistent with the way the viscosity varies as a function of the probe depth (Section 2.4.2): the fluctuations increase in amplitude in regions where the viscosity is smaller. At

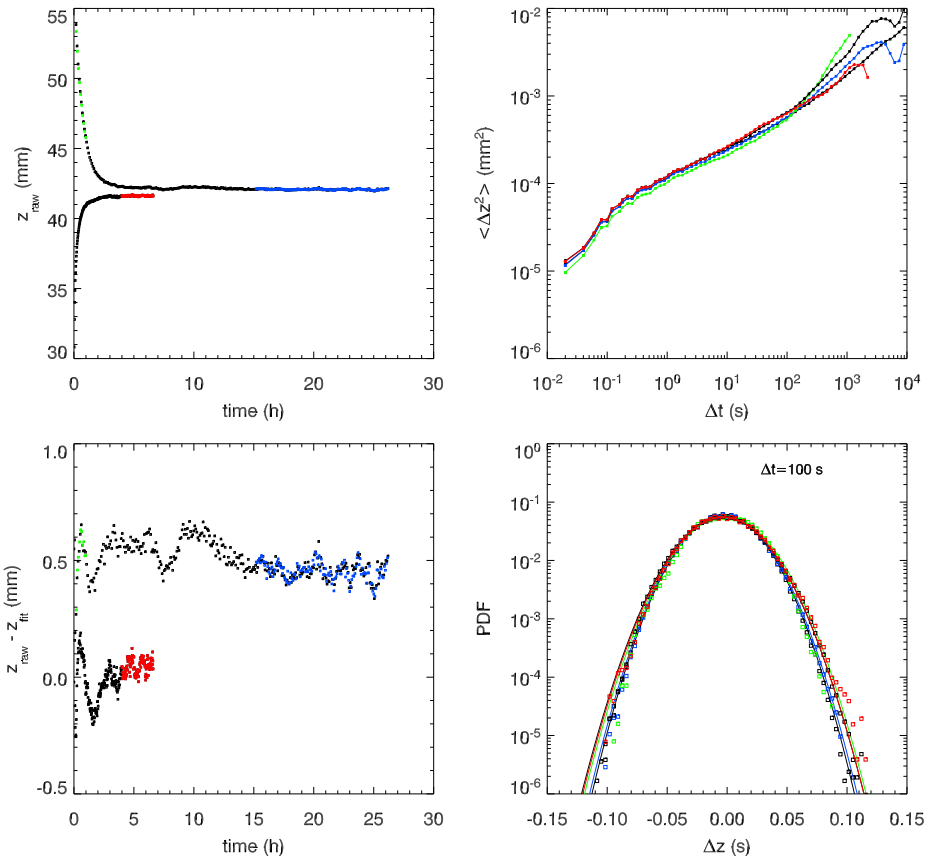

FIGURE 3.7: Top left panel: Probe position ($z_{raw}(t)$) for a sinking probe and rising probe experiment. $H = 60$ mm, $M = 76$ g, $R = 25$ mm, $\Omega = 0.1$ rps. Lower left panel: probe position data after the sinking (or rising) motion is subtracted ($z_{raw}(t) - z_{fit}(t)$). Top right panel: The mean square displacement curves for different probe depths - the colour corresponds to the segment of the raw data in the panel at the top left. Lower right panel: PDFs for each segment of the data set - the time step is 100 s.

$H = 60$ mm, the viscosity is nearly constant for all depths and the fluctuations do not vary in character away from equilibrium. However, at $H = 70$ mm, the viscosity is slightly larger above the equilibrium depth; the fluctuations there are smaller in amplitude than those close to equilibrium.

It is not at all obvious whether the fluctuations should be stronger

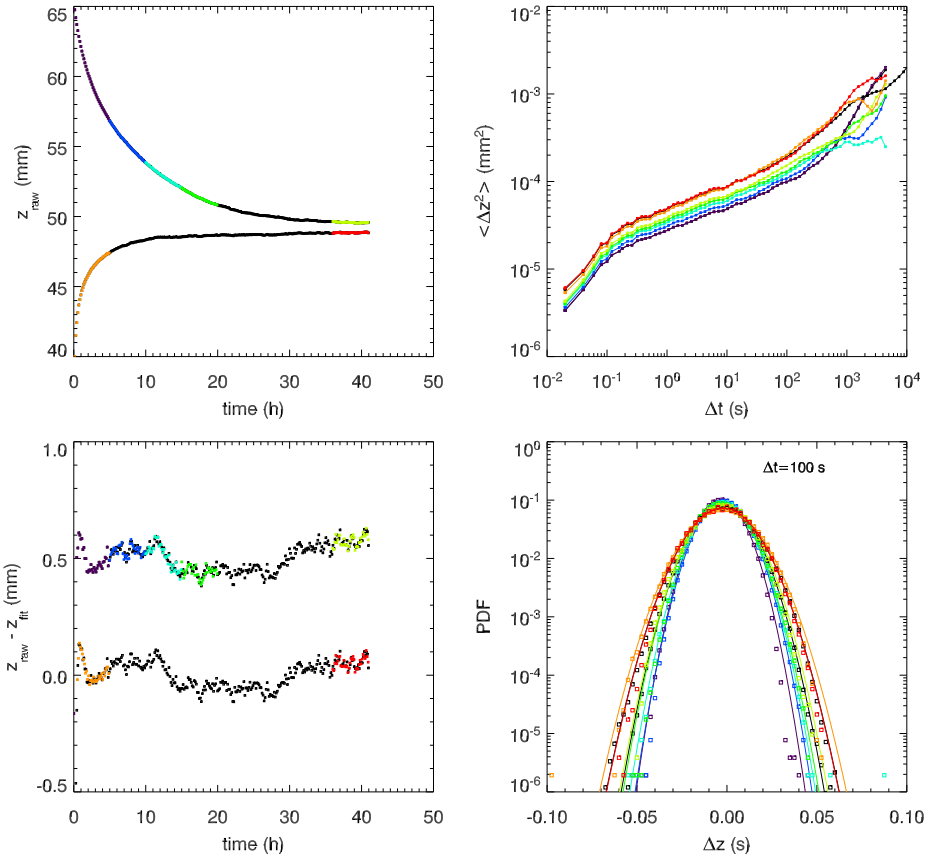

FIGURE 3.8: Top left panel: Probe position ($z_{raw}(t)$) for a sinking probe and rising probe experiment. $H = 70$ mm, $M = 85$ g, $R = 25$ mm, $\Omega = 0.1$ rps. Lower left panel: probe position data after the sinking (or rising) motion is subtracted ($z_{raw}(t) - z_{fit}(t)$). Top right panel: The mean square displacement curves for different probe depths - the colour corresponds to the segment of the raw data in the panel at the top left. Lower right panel: PDFs for each segment of the data set - the time step is 100 s.

closer to the region where they are generated. Examining the fluctuations of probes at different depths in the system indicates that for $H = 60$ mm the fluctuations barely change with probe depth (Fig. 3.7), while at $H = 70$ mm, the fluctuations vary by a factor of 2 over a range of 20 mm. In Section 3.3.4 we show that varying the equilibrium depth by changing the

mass of the probe does not change the MSD curves (Fig. 3.9). It is therefore reasonable to conclude that, at least for $H = 55$ mm and $H = 60$ mm, the fluctuations do not vary vertically within the system.

3.3.4 Tuning the fluctuations by changing the probe mass

Predictions about the effect of the probe mass and diameter can be made by considering the Ornstein-Uhlenbeck theorem, which describes the behaviour of a random walker in a potential well [63]. The motion of a random walker in a potential well is Brownian on short time scales, but has the characteristics of white noise on long time scales. Although the motion of the probe in this experiment is not Brownian (the scaling exponent α in $|\Delta z(\Delta t)|^\alpha \propto \Delta t$ is not 2), the mean square displacement curves exhibit a plateau, and so it is interesting to inquire if the characteristics of this plateau are consistent with the behaviour prescribed by the Ornstein-Uhlenbeck theorem.

The potential well occupied by the floating probe has the form $U = -\frac{1}{2}\rho g r^2 \pi (z - z_{eq})^2$, where z_{eq} is the equilibrium depth predicted by Archimedes' Rule. The width of the potential well is therefore determined entirely by the probe radius - varying the mass of the probe changes z_{eq} and simply shifts the potential up and down. According to the Ornstein-Uhlenbeck theorem, the vertical position of the plateau for a random walker in a quadratic potential ($U = -\frac{1}{2}kx^2$) is $k_B T/k$. Since the effective elastic constant, $k = \pi \rho g r^2$, is independent of the probe mass, the vertical position of the plateau in the mean square displacement curves should also be independent of the probe mass. This result is precisely what is observed for $H = 60$ mm and $H = 50$ mm, (Fig. 3.9).

Because probes of different mass float at different equilibrium depths, changing the probe mass also provides a way to explore how the magnitude of the fluctuations varies within the system. An additional corollary of the observation that the plateau position does not depend on the probe mass is that the fluctuations in the system do not vary substantially throughout the bulk.

According to the diffusion equation (Eq. 3.2), the mean square displacement curves should rescale with the viscosity . However, unlike a real liquid, the viscosity of our granular liquid depends on the mass of the probe. Since the viscosity of our granular liquid depends on the probe mass, the point at which the plateau begins should scale with the probe

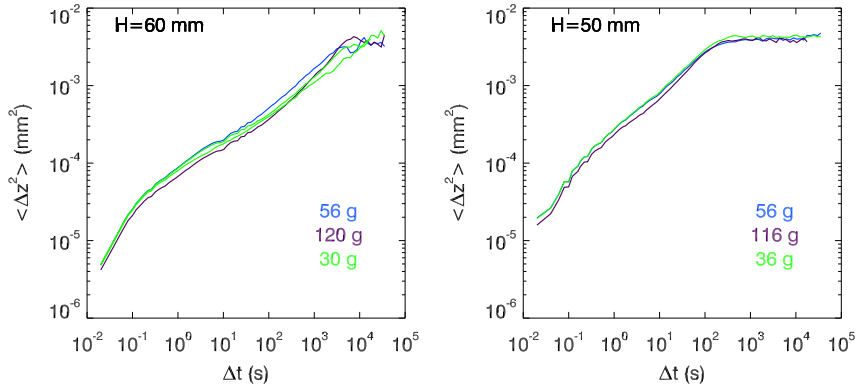

FIGURE 3.9: Mean square displacement curves for probes with different masses ($H = 80$, $R = 25$ mm). Purple and blue: $M = 36$g. Green and light green: $M = 56$g. Orange: $M = 96$g.

mass. Unfortunately, confirming or refuting this hypothesis is experimentally difficult because observing the fluctuations of the probe at equilibrium requires that the probe is light enough to float - and this restricts the range of available probe masses (the 50 mm diameter probe can have masses between 36 and 120 g).

At $H = 60$ mm (Fig. 3.9) the starting points of the plateaus are not distinguishable from each other and at $H = 50$ there is no systematic dependence of the turn-off position on the probe mass. Since the MSD curves are not significantly changed by tuning the mass of the probe, the fluctuations experienced by the probe do not appear to be affected by the mass of the probe.

3.3.5 Tuning the fluctuations by changing the probe radius

For a random walker in a potential well the vertical position of the plateaus in the MSD curves is given by $k_BT/(\rho g \pi r^2)$. It is therefore instructive to examine how the MSD curves scale with the probe radii. Since we observed in the previous section that tuning the probe depth by changing the probe mass does not change the vertical position of the plateau, we infer that the noise in the system (k_BT) does not vary substantially throughout the bulk. The position of the plateau should therefore be expected to scale with the surface area of the probe.

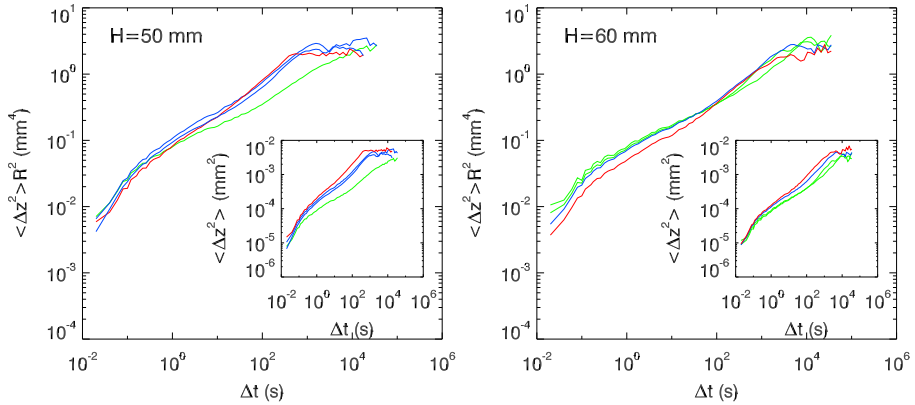

FIGURE 3.10: Mean square displacement curves for different probe diameters rescaled by $R/40$ mm. ($R = 20$ mm (red), $R = 25$ mm (blue) and $R = 30$ mm (green)). Insets: the original mean square displacement curves.

The MSD curves for probe diameters of $40, 50$ and 60 mm are given in Fig. 3.10. Only a small range of probe sizes are available because measuring the fluctuations requires that the probe is light enough to float. At both $H = 55$ mm and $H = 60$ mm, the smaller probe has the higher plateau and scaling the plateau position by the probe area causes the plateaus to overlap. The plateaus are very noisy and so it is not easy to distinguish what the best scaling law should be, however, the scaling behaviour observed is consistent with the prediction that the position of the plateau should scale inversely with the probe area.

3.3.6 Tuning the fluctuations by changing the particle size

As might be expected, increasing the size of the particles in the system increases the size of the fluctuations experienced by the floating probe (Fig. 3.11). Increasing the size of the beads also shifts the vertical position of the plateau upwards and shifts the start of the plateau to the left . The vertical position of the plateau also appears to scale with the bead volume, although this relationship is difficult to determine because only a small range of bead diameters can be studied.

The plateau in the fluctuations is proportional to the volume of a single bead - and is therefore also proportional to the mass of a single bead. This is consistent with the Ornstein-Uhlenbeck theorem where the position of

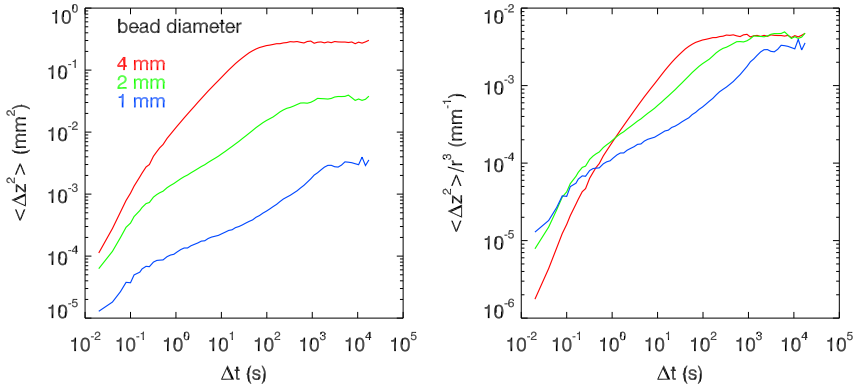

FIGURE 3.11: Left panel: $< \Delta z^2 >$ for beads of different diameters. ($H = 60$ mm, $R = 25$ mm, $M = 56$ mm, $\Omega = 0.1$ rps) Right panel: The plateau position is proportional to the volume of a single bead.

the plateau is $k_B T/(\rho g \pi r^2)$ and the temperature, T, (given by kinetic theory) is proportional to the mass of a single particle.

3.3.7 Moving the probe away from the centre of the cell

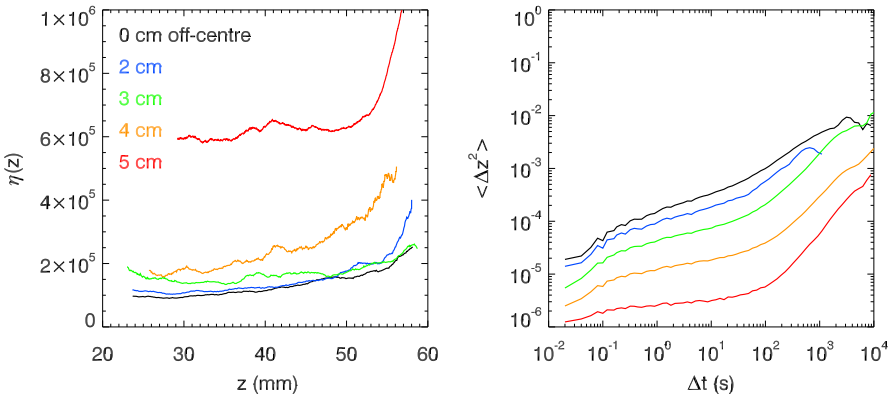

FIGURE 3.12: Left panel: viscosity measured with a probe different distances from the centre of the container ($R = 20$ mm, $M = 214$ g, $\Omega = 0.1$). Right panel: mean square displacement curves for probes floating at different distances from the centre of the container ($R = 20$ mm, $M = 36$ g, $\Omega = 0.1$).

As reported in the previous Chapter (2.4.3), moving the probe away

from the centre of the cell corresponds to an increase in the viscosity of the system. It is therefore interesting to examine the fluctuations of a probe floating off-centre (Fig. 3.12). At short time steps, the MSD curve of the off-centre probe is shifted downwards. However, the plateau for both the centred and off-centre probe is achieved at the same mean square displacement.

3.4 Conclusion

In this Chapter we have characterized the fluctuations of a probe floating in a fluidized granular system. We have examined both the probability distribution functions and the mean square displacement curves of vertical fluctuations in the probe position over a range of time scales. In essentially all cases, we find that the PDFs are Gaussian, as would be expected for a Brownian diffusive system. However, the mean square displacement curves have a more complex shape which depends on the filling height.

There are several notable features of the mean square displacement curves. First, on short time scales the motion of the probe is nearly diffusive, but becomes subdiffusive on longer time scales - and becomes even *more* subdiffusive as the filling height increases. Second, the value of the mean square displacements saturates at long time scales. The appearance of this plateau is concomitant with the behavior of a simple random walker in a potential well, which can be described by the Ornstein-Uhlenbeck theorem. We find that the plateau values of the mean square displacement curves scale with the probe radius but are independent of the probe mass, suggesting that the potential well traversed by the probe is given by the buoyant and gravitational forces. Third, we have found that the time scales at which the plateaus begin are proportional to the viscosity of the system. This behaviour is apparent both in the case where the viscosity is varied by changing the disk rotation speed and in the case where the viscosity is varied by changing the filling height. That the time scale of the viscosity and the time scale of the fluctuations are the same suggests that fluctuations determine the viscosity of the system.

We have also examined how the fluctuations change with probe position: we have studied both the equilibrium behaviour of probes with different masses and the motion of sinking probes away from the equilibrium position. Our results suggest that the magnitude of the fluctuations

does not vary significantly throughout the system and also does not vary much when the probe is away from the equilibrium position.

Finally, by changing the surface properties of the spinning disk, we have determined that the fluctuations experienced by the probe are generated in the shear band and not at the surface of the disk where it contacts the grains (Section 3.6).

Studying the motion of a probe floating in our granular liquid has offered insight into the character of the fluctuations in the system. However, a floating probe can only sample the collective motion of many beads - and not the motion of single particles. One way to investigate the microscopic behavior of single grains is to use a 3D scanner in which the particles are immersed in an index-matched fluid containing a fluorescent dye [64]. This makes it possible to track each particle and to assess whether their *individual* motion is Brownian.

3.5 Appendix: Describing the motion of the probe

The trajectory of the probe, $z_{raw}(t)$, is the sum of three terms: the nearly-exponential decay as the probe approaches the equilibrium depth, $z_{sink}(t)$; a spurious oscillation at the disk rotation frequency caused by misalignment of the probe relative to the disk, $z_{osc}(t)$; and the intrinsic granular fluctuations we wish to probe, $z(t)$ (Fig. 3.13a).

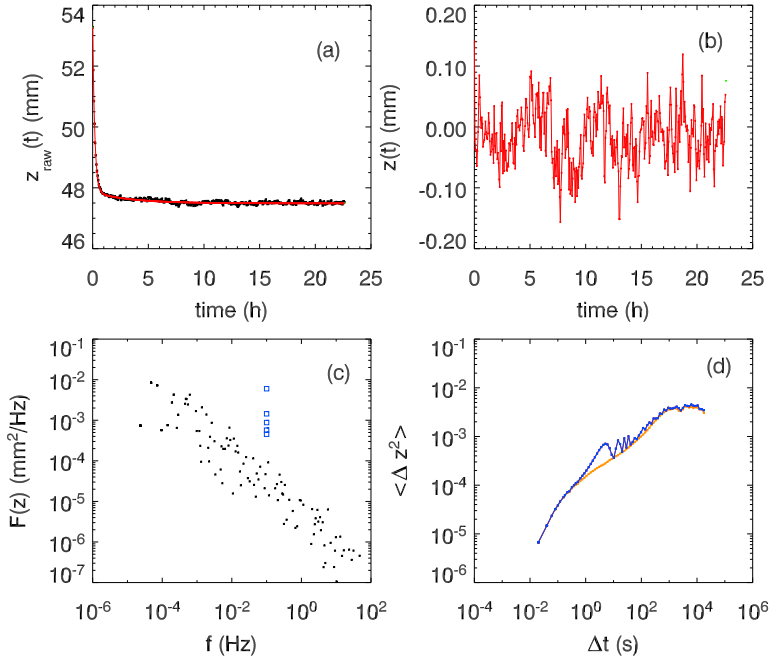

FIGURE 3.13: Analysis of a typical fluctuation data set. (a) probe position as a function of time data with fit. (b) the fluctuations given by the difference between probe position and fit. (Note the oscillatory component at the driving frequency which is due to misalignment of the probe and disk is not subtracted here. The amplitude of this oscillation is small enough that it cannot be observed in the raw signal.) (c) Power spectrum ($F(z)$) of probe position as function of time. The peak at the driving frequency (0.1 Hz) is denoted with blue squares. (d) Mean-square displacement. Blue: data treated before the decay envelope and the oscillatory component at 0.1 Hz is removed. Orange: decay envelope and oscillatory component subtracted from the data.

To exclude the sinking motion of the probe, we fit the trajectory to

sum of two exponentials (see Section 2.6). The resulting fluctuation signal is given in Fig. 3.13b. Analysis of the power spectrum, $F(z)$, indicates that there is a substantial contribution at the disk rotation frequency (Fig. 3.13c). This oscillation is caused by slight misalignment of the bottom of the probe with respect to the spinning disk. For systems in which the motor is coupled to the disk with a rubber band, the band serves as a sort of filter and the peak at the driving frequency is eliminated. However, in the directly-driven system, this oscillation makes a significant contribution over a very narrow frequency band. We filter out this oscillation by computing the FFT of the data set, removing the peak at the driving frequency and transforming back to position space by performing an inverse FFT. Once the oscillation is removed we compute the PDFs and mean square displacement curves (Fig. 3.13d).

3.6 Appendix: What causes the fluctuations?

It is now evident that fluctuations in the grains play a significant role in determining the liquid-like character of the system. But where and how are the fluctuations produced? There are several possible sources of fluctuations beside flow in the shear band. These include grain motion near the spinning disk, spurious oscillations caused by the (micro)stepper motor, misalignment of the probe relative to the disk and residual flow near the probe. In the following Sections we demonstrate that these processes have only a weak effect on the fluctuations. We conclude that the liquid-like behaviour of our granular fluid results primarily from fluctuations generated in the shear band.

3.6.1 The effect of the disk surface on the fluctuations

The rotating disk driving the beads has a dimpled surface so that the disk does not slip against the beads. To probe whether the disk surface affects the fluctuations we cover the dimples with smooth paper and attach a paper bar across the diameter of the disk to drive the grains. The bar has a height of 2 mm and a width of about 7 mm. (If the dimples are covered only with smooth paper, the beads will slip at the interface between the grains and the disk.)

The power spectra for fluctuations of the probe in grains excited by

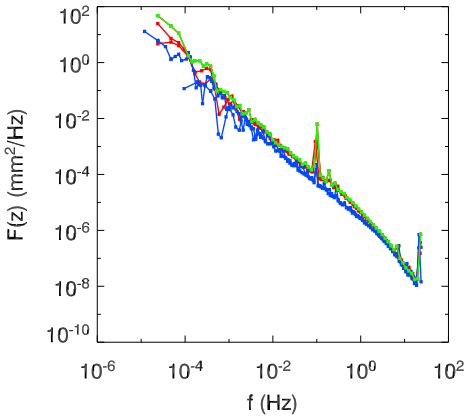

FIGURE 3.14: Changing the surface of the spinning disk does not modify the power spectra of the fluctuations. Blue: regular dimpled disk, green: paper on the surface of the spinning disk, red: paper and bar on spinning disk. ($H = 60$ mm, $R = 25$ mm, $M = 56$ g, $\Omega = 0.1$ rps. Note that the peak at the driving frequency has not been filtered out.)

disks with different surfaces are compared in Fig. 3.14. There is no significant difference between the fluctuations for different driving mechanisms. Furthermore, MRI data [16], along with rheological measurements of the local flow (Section 2.4.3), indicate that the flow speed next to the disk is similar to the disk speed. These observations suggest that the fluctuations are not generated at or near the surface of the disk.

3.6.2 The effect of the driving mechanism on the fluctuations

Another possible source of spurious fluctuations are vibrations produced by the (micro)stepper motor. In an early version of the experiment, the disk and motor were coupled by means of a flexible band. A subsequent iteration of the setup utilized a much stiffer band. Finally, the experiment was modified so that the motor was attached directly to the disk. The power spectra and MSD curves for experiments with different driving mechanisms are plotted in Fig. 3.15.

We find that the older (stretchier) band appears to absorb energy at a characteristic frequency which is slightly higher than the driving frequency. In addition, the overall magnitude of the fluctuations is slightly damped relative to the other driving mechanisms. No systematic difference between directly-driven, and stiff-belt driven experiments can be seen. We conclude that spurious vibrations from the motor do not affect significantly the fluctuations.

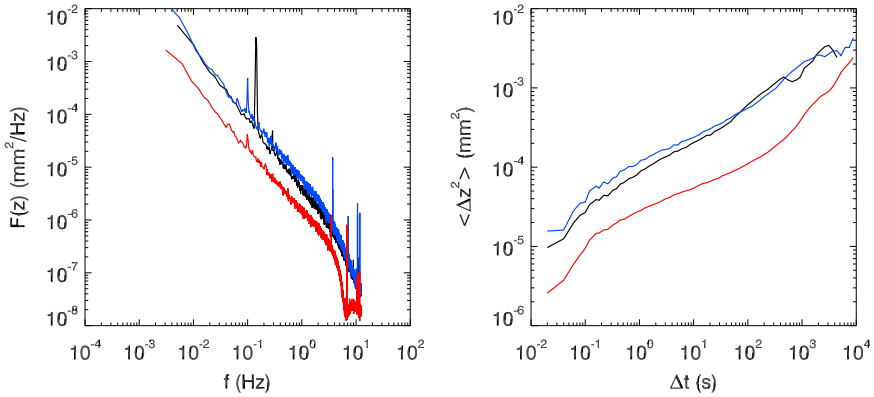

FIGURE 3.15: Effect of the driving mechanism on the fluctuation power spectra, $F(z)$ (left) and the mean square displacement curve (right). ($H = 60$ mm, $R = 25$ mm, $M = 56$ g). Black: motor drives the disk directly. Blue: the disk is driven by the motor via a newer (less elastic) band. Red: the disk is driven by the motor via an older (more elastic) band.

3.6.3 The effect of probe rotation on the fluctuations

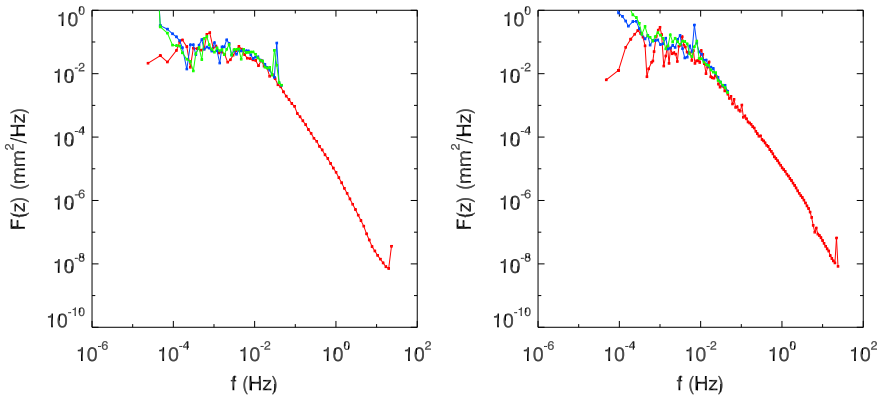

FIGURE 3.16: The fluctuation power spectra for runs where the probe is allowed to rotate freely (blue, green) and where the rotation is prevented (red). Left panel: $H = 40$ mm. Right panel: $H = 45$ mm. ($R = 25$ mm, $M = 36$ g, $\Omega = 0.1$ rps).

Because the probe is cylindrical, it is free to rotate in the grains: it is possible that this motion could affect the fluctuations or promote fluidiza-

tion. In order to examine what happens to the fluctuations when rotational motion of the probe is inhibited, we attach a "wing" to the barrel of the probe which slides against the mount as the probe ascends or descends. Inhibiting the rotational motion of the probe does not lead to any changes in the power spectra (Fig. 3.16), aside from reducing the magnitude of the peak around the driving frequency. The rotational motion of the probe is clearly not exciting fluctuations in the grains. Note that experimental runs in which the probe is permitted to rotate freely exhibit a peak below the rotation speed of the disk; this peak is shifted further for the $H = 45$ mm data than for the $H = 40$ mm data 3.16, which suggests that at low filling heights the peak corresponds to the local flow speed of the beads.

3.6.4 The effect of tilting the probe on the fluctuations

The probe can be adjusted so that the bottom of the cylinder is as parallel as possible to the spinning disk in the bottom of the container. This is accomplished by allowing the probe to rotate on top of the spinning disk and adjusting the mount until the amplitude of the periodic displacement is minimized. This allows the amplitude of the oscillation to be reduced to 0.05 mm. Nevertheless, the raw probe position, $z_{raw}(t)$, always includes a oscillatory component at the same frequency as the disk rotation.

To test whether probe misalignment changes the fluctuations, the probe can be deliberately misaligned. We tilt the probe slightly so that there is a 0.9 mm different between the height of one side of the probe ($R = 25$ mm) and compare the mean square displacements to the regular calibrated system (Fig 3.17). The misalignment of the spinning disk and the probe bottom does not appear to provoke fluidization in the system or to otherwise change the characteristic mean square displacement curves.

3.6.5 The influence of bead surface properties on the fluctuations

The humidity and the age of the beads appears to have a small effect on the characteristic fluctuations (Fig. 3.18). The age of the beads may affect the surface roughness because older beads which have been sheared for a long time can become smoother due to abrasive contact with other beads. This may explain why the power spectrum for the new beads has a slightly

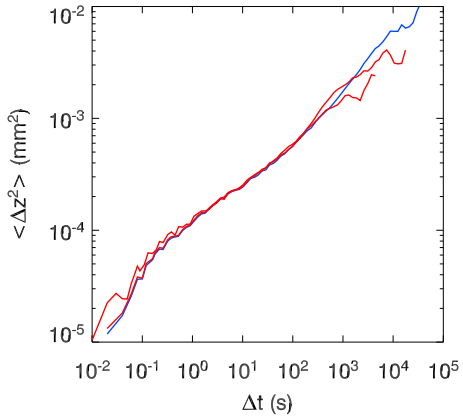

FIGURE 3.17: MSD curves for runs where the probe is not tilted (blue) and where the probe is tilted so that the top of the cylinder is horizontally displaced 0.9 mm (red). The data is from direct-drive experiments and the peak at the driving frequency is removed by filtering. ($R = 25$ mm, $M = 76$ g, $\Omega = 0.1$ rps)

larger amplitude than the power spectra for the older (and presumably smoother) beads.

During the experiments described in this Chapter, the humidity is controlled by placing the system inside a plastic tent while dry air flows in from the air-bearing. The humidity can be increased by removing the plastic tent and exposing the system to room-temperature conditions.

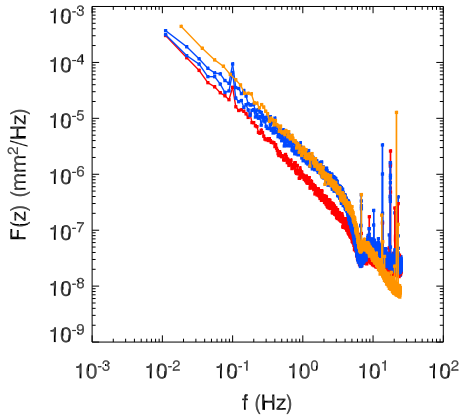

FIGURE 3.18: Fluctuation power spectra for systems with different humidity and bead properties. Blue: old humid beads. Red: old dry beads. Orange: new humid beads. ($H = 60$ mm, $R = 25$ mm, $M = 36$ g, $\Omega = 0.1$ rps)

Chapter 4

Oscillatory shear in a granular system

In Chapters 2 and 3 we examined a liquid-like granular system created by continuous shear in a split-bottom cell. One of the surprising features of this experiment is that the viscosity scales inversely with the disk rotation speed, even at very low rotation rates: there is no transition to a regime which exhibits a yield stress. In other words, the trajectory of a probe sinking in the system depends only on the total amount of strain applied by the disk: the probe will traverse the same path if the disk makes one revolution very slowly or one revolution very quickly.

In this Chapter, we excite the grains by repeatedly rotating the disk through an angle, A, rapidly reversing the direction of the disk and then rotating back through the same angle: the rotation rate, Ω, periodically changes sign, but stays constant in magnitude. The total amount of strain per unit time is therefore the same as in the continuously driven system, so the two systems might be expected to behave in a similar way. However, when the direction of shear is reversed, the grains in the system excited by oscillatory shear begin to exhibit different behaviour: unlike a continuously sheared system, which dilates rapidly until a steady state is reached [16], grains driven by *oscillatory* shear undergo slow compaction [65]. Moreover, it seems possible that for small driving amplitudes much of the grain motion becomes reversible, and the forward and backward rotation of the disk no longer has a fluidizing effect. The nature of the state created by oscillatory shear is not understood: does it have the properties of a liquid, like the continuously sheared system, or does it have the properties of a solid, like the stationary system?

In this Chapter we explore the characteristics of our oscillatory-shear driven system using three different techniques: first, we examine the evolution of the density by measuring the position of a plate resting on the surface of the grains; second, we examine the motion of floating and sinking probes; and, finally, we profile the local flow with a rheometer.

We find that when the disk reverses direction the grains compact rapidly

before beginning to dilate again as further strain is applied. In addition, we observe that the steady-state density of the grains decreases as the driving amplitude increases, and that at large driving amplitudes the density approaches that of a continuously sheared system. Unlike in the continuously sheared system, we find that the speed of a heavy object sinking in grains driven by oscillatory shear decreases as the probe becomes submerged in the grains: the velocity of the probe scales inversely with the time elapsed since the probe began sinking and algebraically approaches a final velocity, v_f. As in continuously sheared systems, this final velocity scales with the disk speed, Ω. We also find that while v_f is independent of the driving amplitude for $A > 1$ rev, the probe speed becomes proportional to the driving amplitude for $A < 0.5$ rev. Finally, measurements of the local strain performed with a rheometer indicate that at small driving amplitudes the ratio of the strain *near the surface* to the strain applied by the disk is much larger than for continuous driving. Meanwhile, the ratio of the strain *near the disk* to the applied strain is much smaller than for continuous driving.

4.1 Apparatus

In the following experiments we utilize the same apparatus as in Chapters 2 and 3; however, instead of rotating the disk continuously, we will now excite the grains by *oscillating* the disk. During early experiments with oscillatory driving, the disk was driven by a 5718L-01S stepper motor from Lin Engineering. This motor has a maximum resolution of 51200 steps per revolution and can exert torques of 1.5 Nm when operating at 1.0 rps. However, oscillatory shear causes the system to compact and this means that the amount of torque required to rotate the disk increases as the experiment progresses. Eventually the motor is no longer able to comply and the disk stops moving. This problem occurs for small oscillation amplitudes ($A < 0.01$ rev). In order to avert this problem, the stepper motor was replaced by an Applied Motion V0250-214-B-000 Q-series motor with a position feedback system. This motor has a resolution of 8192 steps per revolution and can exert a maximum torque of 1.7 Nm; this torque is not much more than that exerted by the Lin Engineering motor, however, the position feedback sensor enables the torque to be increased when required.

The use of a motor with a position feedback system also allows the position of the oscillating disk to be tracked. A rheometer probe can then be used to simultaneously measure the local strain in the system: the strain measured by the rheometer can therefore be determined as a function of the strain applied by the disk. We drive the system at speeds of 0.01 to 0.5 rps with an acceleration of 1 rev/s^2 between reversals. A feedback loop is used to determine the amount of current supplied to the motor; the parameters in the feedback loop are selected to optimize the response of the motor in the driving regime [1].

4.2 Probing dilation and compaction

In order to probe fluctuations in the bulk density of the split-bottom system, the sinking probe apparatus (Fig 2.1) can be modified by removing the cylindrical probe and replacing it with a flat plate (Fig.4.1). The radius of the plate (7.5 cm) is slightly less than the radius of the split-bottom cell so that the plate is free to move in the vertical direction. The mass of the plate is 14.0 g; the total mass of the probe barrel and plate is 33.2 g.

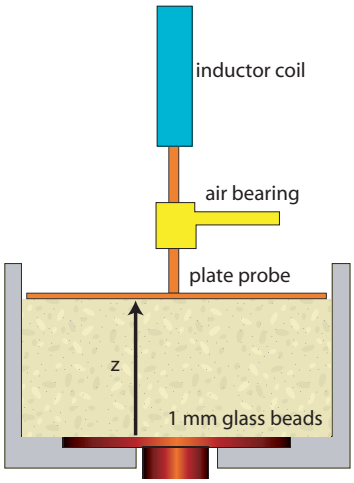

FIGURE 4.1: Apparatus for measuring dilation and compaction of the entire system. The cylindrical probe (Fig.2.1) is replaced by a flat plate which is slightly smaller than the split-bottom cell. The plate probe is free to move vertically in the air-bearing and the position of the probe is determined using an inductor coil. The disk is oscillated with amplitude A at a speed of Ω rps.

[1] The Applied Motion Quicktuner feedback loop parameters which optimize how quickly and smoothly the driving speed is achieved: Stiffness: 3420, Damping: 4207, Inertia: 237.

The grains in the split-bottom cell are initially prepared by stirring the system with a rod and flattening the surface with a plate. The probe plate is then placed on the surface and the position of the plate is measured with an inductor coil as the disk is driven. The effect of different preparation schemes is discussed in Sec. 4.2.3.

4.2.1 Short time-scale behaviour

We begin by examining the behaviour of the grains on the time scale of a few oscillations. The grains initially dilate as they are excited by the rotating disk (Fig.4.2a,d). Then, when the disk reverses direction, the system undergoes a short period of rapid compaction before beginning to dilate again as more shear is applied. If the oscillation angle is very small (Fig.4.2a), then the rate at which the system contracts is very similar to the rate at which the system dilates, and the probe motion appears almost sinusoidal. However, as the oscillation amplitude becomes larger, it is clear that the compaction that occurs when the disk reverses is much more rapid than the subsequent dilation (Fig.4.2d).

The amount of strain applied from the point where the reversal occurs to the point where the system begins to dilate again depends on the oscillation amplitude. For $A = 0.0059$ rev, the strain applied while the system is compacting is about half the total oscillation amplitude, or 0.003 rev. For $A = 1$ rev, the strain applied during compaction is about 0.035 rev. At the radius of the disk, a strain of $A = 0.035$ rev corresponds to a displacement of 1 mm - or one grain diameter. In earlier work on oscillatory shear in a Couette cell Toiya *et. al.* [65] found that the displacement of the oscillating cylinder during compaction corresponded to a displacement of about 0.5 grain diameters.

4.2.2 Long time-scale behaviour

Although the short-timescale behaviour exhibits both a compaction phase and a dilation phase, we find that over the course of many oscillations, the system undergoes compaction (Fig 4.2b,d). There are two existing descriptions of compaction processes in granular systems, the “Chicago" model [3, 66] and the Kohlrausch-Williams-Watts model [66]. The former

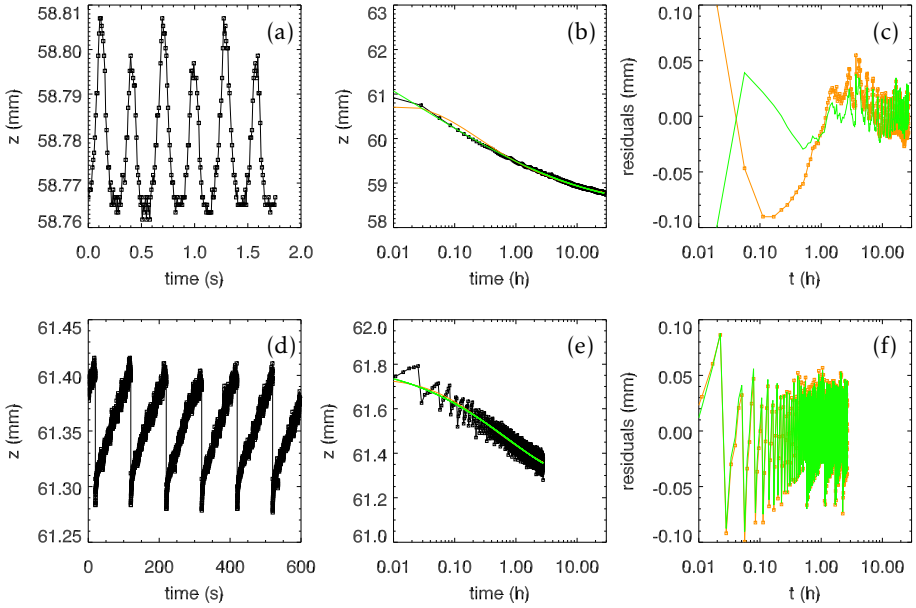

FIGURE 4.2: The evolution of the height of the grains in the container on long and short time scales for $A = 0.0059$ rev, $\Omega = 0.02$ rps (upper panels) and $A = 1.0$ rev, $\Omega = 0.1$ rps (lower panels). Panels (a), (d): position of the plate probe during the last six oscillations of the disk. Panels (b), (e): the KKW model (green) and the logarithmic Chicago model (orange) are both good descriptions of the long-timescale compaction. Panels (c), (f): the residuals of the fits to the Chicago and KWW models.

has a logarithmic form:

$$\rho(t) = \rho_{eq} - \frac{\rho_0 - \rho_{eq}}{(1 + B\ ln(1 + t/\tau))} \ . \tag{4.1}$$

Meanwhile, the KWW model contains a stretched exponential:

$$\rho(t) = \rho_{eq} - (\rho_0 - \rho_{eq}) e^{(-t/\tau)^{\beta}} \ . \tag{4.2}$$

The height of the grains in the container as a function of time can be described using the both the KWW or the Chicago fit, both of which seem to work equally well (Fig 4.2b,c,e,f).

4.2.3 Role of grain preparation

As we have just demonstrated, the height of a column of grains excited with oscillatory shear can be described by a logarithmic relaxation; however, the rate and amount of compaction depend on how the grains are prepared. Stirring the system with a rod produces an initial state which is less dense than if the system is prepared with continuous shear: the initial height of systems prepared by stirring is larger than the initial height of systems prepared with only shear (Fig. 4.3). It is also apparent that a system which begins with a lower density will compact more quickly than a system which beings with a higher density.

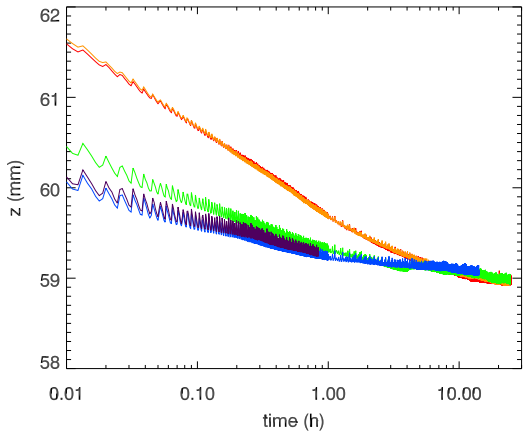

FIGURE 4.3: The effect of different preparation methods on the compaction process for $A = 0.059$ rev, $\Omega = 0.1$ rps. Preparation by shear: 100 rev, 0.1 rps (blue, purple); 300 rev, 0.3 rps (green). Preparation by stirring and shear: 300 rev, 0.3 rps (red, orange).

4.2.4 The final density and the oscillation amplitude

When the grains are driven with oscillatory shear for many hours, the system eventually reaches a state in which the amount of compaction produced by reversing the disk direction is nearly equal to the dilation achieved with the subsequent shear; the subsequent long time-scale compaction becomes very slow with respect to the duration of the experiment. The density of the system in this final state depends strongly on the oscillation amplitude: a smaller oscillation amplitude produces a denser state than a larger oscillation amplitude. The trajectories of the plate probe for the final five oscillations, as well as the final density of the grains are

plotted in Fig.4.4. The final densities are determined from the probe positions at the end of each 12 hour experiment. For large oscillation amplitudes, the density of the system approaches the density of the continuously sheared system (Chapter 2).

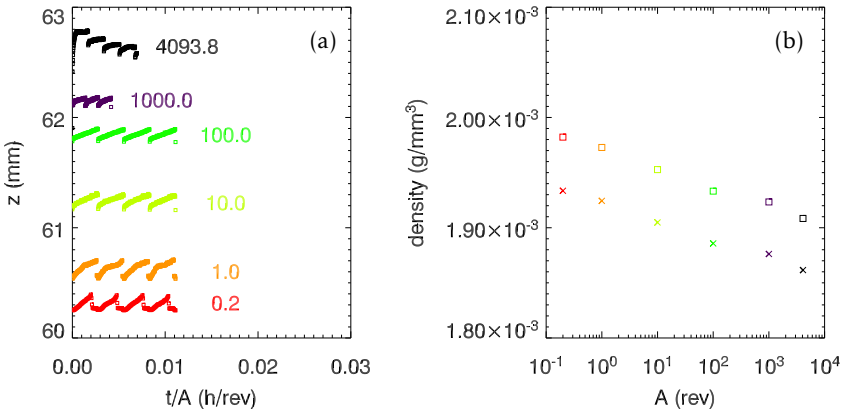

FIGURE 4.4: Left: Trajectories of the plate probe for the last five oscillations in systems generated with different oscillation amplitudes. The oscillation amplitudes (in revolutions) are indicated next to the trajectories. $\Omega = 0.2$ rps for the two experiments with the largest amplitude oscillations and 0.1 rps for the remainder. Right: final density. The squares indicate the minimal density on dilation while the crosses indicate the maximal density on compaction.

4.3 Describing the motion of a heavy sinking probe

In Chapter 2 we characterized the liquid-like behaviour of a granular system excited with continuous shear by studying the motion of a cylindrical probe sinking in the grains. We found that the continuously sheared system exhibited liquid-like behaviour and that the velocity of the probe was proportional to the sum of the gravitational and buoyant forces acting on the probe. In the following Section, we will use this same technique to examine the behaviour of grains excited by oscillatory shear.

Surprisingly, the motion of a heavy sinking probe in grains driven by oscillatory shear is not very liquid-like. A heavy probe, which would sink

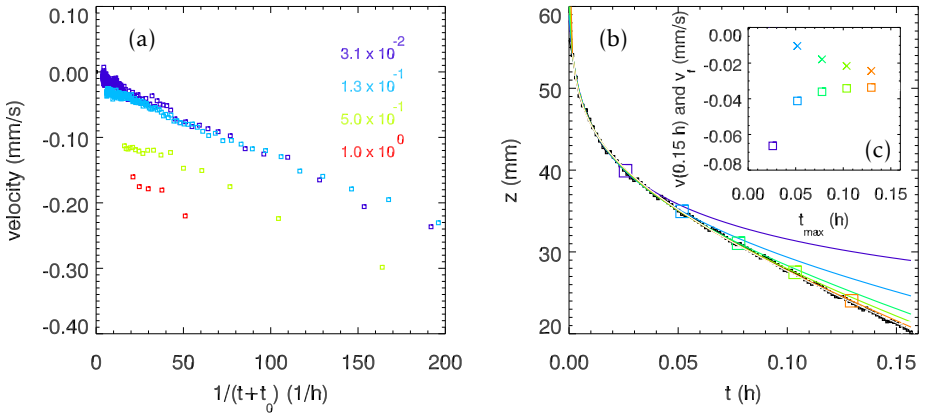

FIGURE 4.5: (a) Probe trajectory as a function of the inverse time for different driving amplitudes (as labelled in revs). (b) Modeling the trajectory of the sinking probe (black) with Eq. 4.3. In order to check that the value of v_f converges, the fit is performed over successively longer segments of data. The end points of each fit (t_{max}) are marked with large squares and different colours denote the fit obtained for each subset of the trajectory. (c) The fitted values of v_f ($\times$) and v at $t = 0.15$ h ($\square$) converge as the data set lengthens. ($M = 146$ g, $\Omega = 0.03$ rps, $A = 0.2$ rev.)

at a constant velocity in the liquid-like continuously sheared system, has a much different trajectory in the oscilation-driven system. The probe sinks very rapidly for approximately 2 cm, then slows and gradually approaches a constant velocity (Fig. 4.5b).

Initially, the velocity of the probe scales with the inverse time, which means the position of the probe scales with $ln(t)$ (Fig 4.5a). This form is similar to that of the compaction process, where the density of the packing also scales with $ln(t)$. The probe eventually reaches a regime in which the liquid-like behaviour of the grains is restored and the velocity of the heavy sinking probe approaches a constant. The trajectory of the probe is described by:

$$v = v_f + \frac{k}{t + t_0}. \tag{4.3}$$

Note that the parameter v_f is always smaller in magnitude than the velocity of the probe extracted by the fit over the last portion of an experiment with a duration of t_{max}. In other words, $v(t_{max}) < v(\infty)$. In order to check that the values of v_f are robust, the fit can be applied to progres-

sively longer segments of the data: the resulting values of v_f converge as the duration of the data segments increases (Fig. 4.5.c).

4.3.1 Annealing time

Once the initial preparatory stirring and shear have been performed, the oscillatory driving begins and the grains immediately start to compact. The grains can also be prepared with *additional* oscillatory shear ("annealing") in order to examine how the density of the system affects the velocity of the probe. Examining the trajectories of sinking probes after the system has been annealed indicates that the probe moves more slowly once the beads have been compacted: the density of the grains plays a role in how quickly a heavy probe can initially sink into the system (Fig. 4.6). However, the final velocity of the probe, v_f, is not correlated to the preparation protocol, which suggests that v_f is a well-defined parameter which characterizes the motion of the probe in the grains (Fig. 4.6b). The fit in Eq. 4.3 also yields similar values of k (Fig. 4.6c) for each of the different annealing times. There is not clear relationship between t_0 and the annealing time (Fig. 4.6d).

For experiments in which there is a lengthy period of oscillatory compaction before the probe is placed in the grains, the probe initially has a much smaller velocity than if the probe starts sinking as soon as the oscillatory shear begins. The fit to Eq. 4.3 yields similar values of v_f and similar values of k for each of the different annealing times (Fig. 4.6b,c). There is not clear relationship between t_0 and the annealing time (Fig. 4.6d).

The observation that probes initially sink more slowly when the system has been annealed for long times suggests that the viscosity of the system increases as it becomes more compact. MRI measurements in continuously sheared systems offer other insights into the way the local density evolves over time. The work of Sakaie *et. al.* [17] indicates that continuous shear causes dilation in the shear band and that this dilated region gradually expands upwards and downwards away from the shear band as more strain is applied. Perhaps a similar *compaction* front propagates upwards from the shear band in our oscillated system. This may explain why the probe slows as it advances deeper into the grains, as well as why the initial speed depends on preparation protocol, and why the final speed appears to be independent of the preparation protocol.

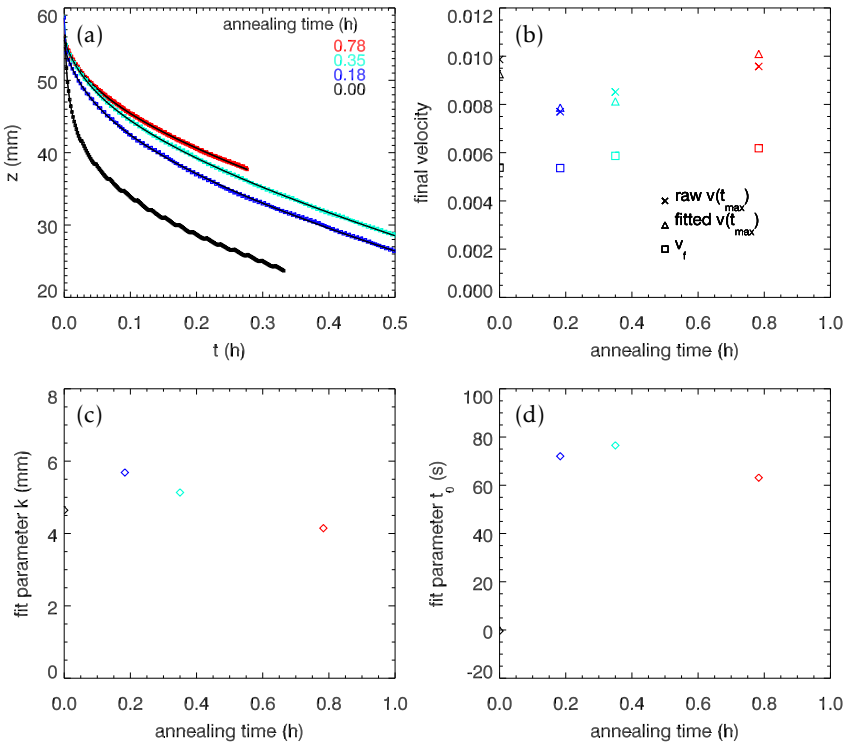

FIGURE 4.6: (a) Probe position as a function of time for different annealing times. (b) The velocity at the end of the probe trajectory from both the fit and the raw data, as well as the value of the fit parameter v_f (the velocity as $t \to \infty$). (c) The value of the fit parameter k for different annealing times. (d) The value of the fit parameter t_0 for different annealing times. ($M = 146$ g, $R = 15$ mm, $\Omega = 0.02$ rps, $A = 0.0625$ rev.)

4.4 The effect of A and Ω on the sinking speed of a heavy probe

When the beads are excited by oscillating the disk, the final speed (v_f) of an object in the grains depends on both the driving speed (Ω) and the driving amplitude (A). Just as for the continuously sheared system (Chapter 2), we can examine how Ω and A affect the speed at which the probe sinks. In the following experiments, the system is prepared by stirring the grains with a rod and rotating the disk 10 times.

4.4.1 The sinking speed of a heavy probe is proportional to Ω

When the beads are excited by oscillating the disk, the final sinking speed of a heavy probe scales with the disk speed: $v_f \propto \Omega$ (Fig. 4.7). This scaling law is valid for all the driving amplitudes we examined. In addition, this same scaling law applies to the situation where the disk is driven continuously (Chapter 2), which indicates that the behaviour of the system depends primarily on the applied *strain* and not on the *strain rate*: the reversal process does not introduce an additional time scale into the system.

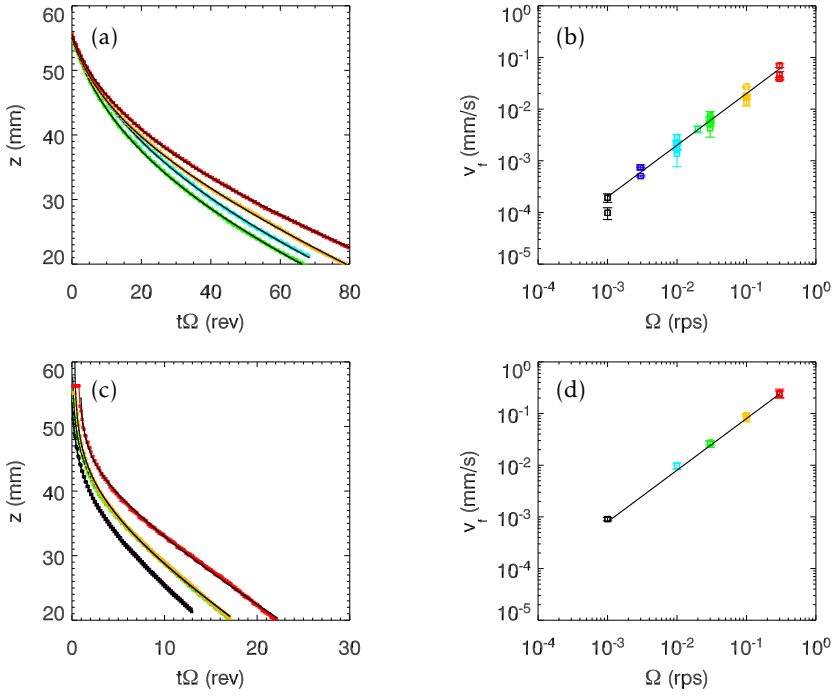

FIGURE 4.7: For a driving amplitude of 0.059 rev (upper panels) or 0.2 rev (lower panels), the sinking speed of a heavy probe is proportional to Ω. (a), (c) Probe trajectories rescaled by Ω. Black lines indicate fits to Eq. 4.3; the colour of the raw data denotes the value of Ω as plotted in panels (b) and (d). (b), (d) The sinking speed, v_f, as a function of Ω. (Probe $R = 15$ mm, $M = 146$ g.)

4.4.2 The sinking speed of the probe is proportional to A at small amplitudes

We have also examined the effect of the oscillation amplitude on the motion of a sinking probe. We find that for $A < 0.5$ rev, the sinking speed of the probe is proportional to the driving amplitude, while above $A = 1$ rev the value of v_f approaches the speed of a probe sinking in a *continuously* sheared system (Fig. 4.8b). Note that the maximum value of A at which this experiment can be performed is limited by the total strain which can be applied before the sinking probe becomes submerged: is not feasible to do sinking experiments for very large amplitudes because the probe will have sunk below the surface before the disk can reverse direction. Finally, note that the error bars on the values of v_f at very small driving amplitudes are large because the probe has typically not yet reached the regime in which the probe velocity is constant (Fig. 4.8a).

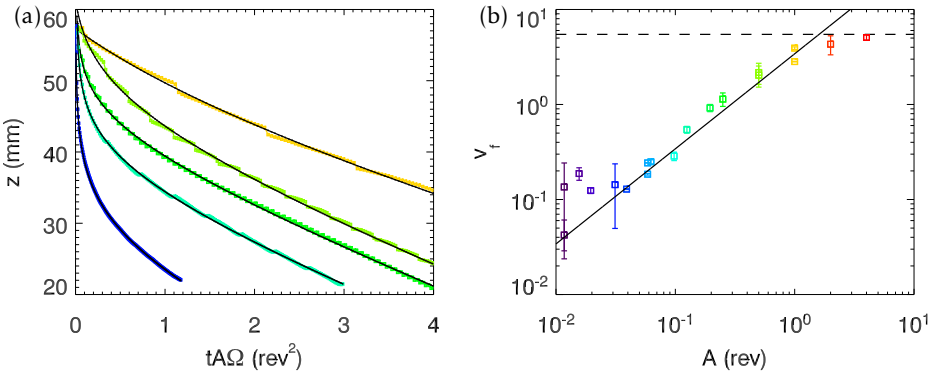

FIGURE 4.8: (a) Probe trajectories scaled by the driving amplitude, A, and the driving speed, Ω. Black lines indicate the fit to Eq. 4.3. The colour of the raw data denotes the value of Ω as plotted in (b). (b) The sinking speed of the probe, v_f, as a function of driving amplitude. The speed of a probe sinking in continuously sheared grains is indicated by the dashed line.

The linear relationship between the probe speed and A at small amplitudes is somewhat surprising: in the continuously sheared system the probe velocity is proportional to the disk speed and we infer that the probe displacement is proportional to the strain applied by the disk. However,

when the disk is oscillated at small amplitudes, the final speed of of the probe is proportional to $A\Omega$: the displacement of the probe per cycle scales as A^2. A possible explanation for the appearance of this scaling behaviour is that the motion of particles becomes nearly reversible at small oscillation amplitudes. The dominant linear component of the strain is therefore eliminated because the particles undergo very little azimuthal motion after the completion of one oscillation cycle. Because the motion is symmetric, the excitations in the system must therefore be dominated by a component which is higher-order in A. The next symmetric component is A^2, so it is this term which determines the probe displacement at small oscillation amplitudes.

4.5 Angular response under oscillatory driving

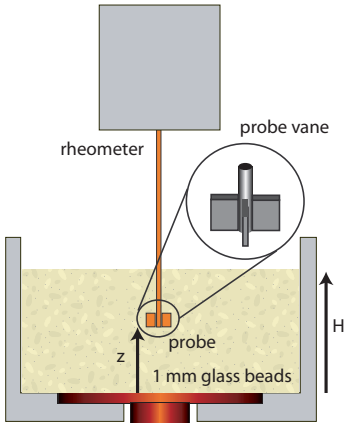

FIGURE 4.9: Apparatus for measuring local flow in grains driven by oscillatory shear. The vertical position of the probe (z) can be adjusted by moving the rheometer on a vertical stage. The disk is oscillated with amplitude A at a speed of Ω rps.

The flow of grains excited by oscillatory shear can also be investigated using a rheometer (Fig.4.9). In the following Section we examine the effect of Ω, A and z on the local flow in the grains. A probe consisting of four square blades which are mutually perpendicular to each other is attached to the rheometer tool; the tool is then aligned along the rotational axis of the oscillating disk and passively indicates the angular position of the probe. The vertical position of the probe can be varied by means of a moving stage, so the flow in the system can be profiled as a function of the distance from the bottom of the container (z).

The following experiments utilize vanes in which the dimensions of the blades are 3×3 and 10×10 mm^2. Previous observations of the flow in continuously sheared systems indicate that the local flow measurements are the same for 3×3, 5×5 and 10×10 mm^2 vanes (Chapter 2).

4.5.1 The effect of Ω on the rheometer trajectory

We find that the trajectory of the rheometer probe is independent of the disk rotation rate: the probe position as function of time ($\theta_R(t)$) depends only on the strain applied by the disk ($0 \leq \theta_D(t) \leq A$) (Fig 4.10). This same scaling behaviour is also observed in continuously sheared grains (Chapter 2). In addition, we find that the inertia of the probe is unimportant: when the disk reverses direction, the probe also reverses direction and the phase of the disk and the probe are the same. Finally, there is no systematic evidence of ageing in the system: the response of the grains at the beginning of the measurement is the same as the response at the end of each 10 minute run.

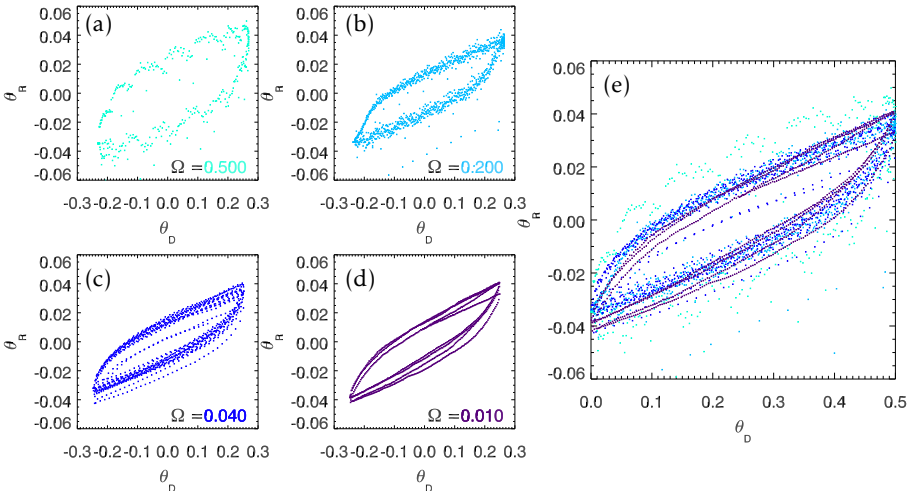

FIGURE 4.10: (a - d) Probe trajectories (θ_R) as a function of the disk position (θ_D) for different Ω (indicated on the plots). (e) Probe trajectories for different Ω are the same, indicating that the probe trajectory is independent of the strain rate. (3×3 mm^2 vane, $A = 0.5$ rev, $z = 20$ mm).

4.5.2 The effect of A on the rheometer trajectory

We have also examined how the motion of the rheometer probe depends on the angular trajectory of the disk (Fig 4.11). When the disk reverses, the grains initially revolve quickly and then slow as more strain is applied. This is similar to the way in which the volume of the system evolves: when the disk reverses there is a period of rapid contraction before the grains begin to dilate again (Section 4.2). Note that the trajectory of the probe does not simply rescale with A: in the moments after the disk reverses, the strain measured by the probe is the same for all driving amplitudes (Fig.4.11). Once a larger amount of strain has been applied, the system reaches a regime where the strain measured by the probe is related linearly to the strain applied by the disk.

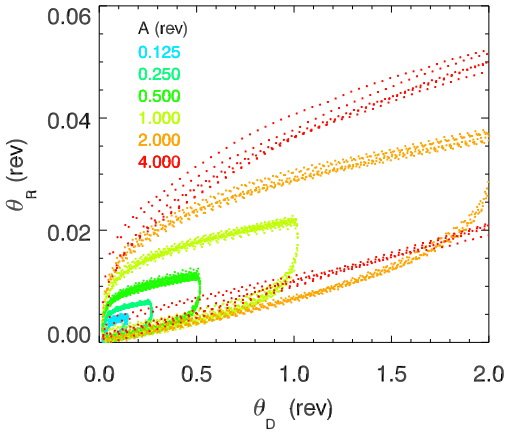

FIGURE 4.11: Angular position of the rheometer probe, θ_R, as a function of the angular position of the disk, θ_D. Colour denotes the different driving amplitudes, as indicated on the plot. ($10\times10\,\mathrm{mm}^2$ vane, $z = 20$ mm.)

4.5.3 The effect of z on the rheometer trajectory

The strain measured by the probe also varies with the vertical position of the probe (z). In Fig. 4.12, the ratio of the rheometer amplitude to the disk amplitude (A_R/A) is given as a function of z for different probe sizes and driving amplitudes. For large driving amplitudes the ratio of the strain at the surface to the driving amplitude (A_R/A) is smaller than for small driving amplitudes; as the driving amplitude increases, the ratio A_R/A approaches the ratio of the surface flow speed to the disk speed in a continuously driven system (Chapter 2). However, closer to the disk ($z = 20$ mm), A_R/A is bigger at large A than at small A. This behaviour

suggests that a certain amount of strain needs to be applied before the dome-like region co-moving with the disk can form. This is consistent with MRI measurements of flow in a split-bottom cell [16, 17].

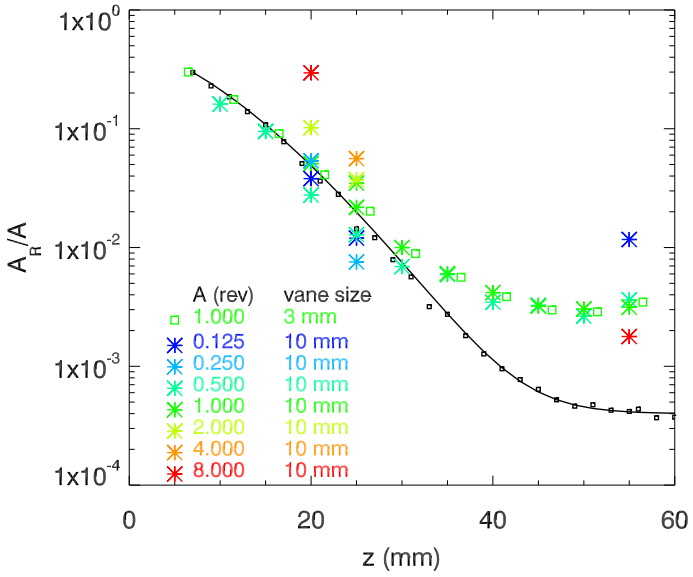

FIGURE 4.12: The ratio of the rheometer amplitude (θ_R) to the disk amplitude (A) as a function of the probe position, z. For large driving amplitudes, θ_R/A is smaller than for small driving amplitudes, while closer to the disk ($z = 20$ mm) θ_R/A is larger at large A than at small A. The ratio of the local flow speed to the speed of the disk for the continuously sheared system is plotted in black.

4.6 Conclusion

We have examined the behaviour of grains in a split-bottom cell excited by oscillatory shear. We find that oscillatory driving promotes compaction and that smaller driving amplitudes produce a denser final state than larger driving amplitudes. Both the "Chicago" model and the KWW model describe the compaction dynamics.

The motion of a cylindrical probe sinking in the system is more complicated than that of a simple liquid; the probe moves more rapidly at the surface and then slows and approaches a constant velocity regime approx-

imately 2 cm below the surface. The probe velocity scales inversely with the elapsed time and the trajectory can be described by an equation of the form $v = v_f + k/(t+t_0)$. The time scale of this behaviour is similar to that of the density during compaction; however, it is not clear what microscopic grain behaviours determine the probe dynamics. That the probe speed *decreases* closer to the disk - while the ratio of the local strain to the driving amplitude *increases* - suggests that the local strain rate is not important for determining the probe speed.

The region in which the probe velocity approaches a constant corresponds to the region where dome flow occurs in a continously sheared system. If the grains are prepared with oscillatory shear prior to the introduction of a heavy probe, the system will be denser and the initial motion of the probe slower than in a system prepared with no oscillatory shear or oscillatory shear of a shorter duration.

Like the continuously sheared system, we find that the velocity of a heavy sinking probe is proportional to the disk rotation speed, Ω. In addition, we find that for small amplitudes ($A < 0.5$ rev), the probe velocity is proportional to A; perhaps this driving amplitude corresponds to the onset of microscopically reversible grain motion in regions outside the shear band.

The question of whether there is a transition from liquid-like behaviour to solid-like behaviour at very small amplitudes is still open. However, with the use of an optical encoder it is possible to track the motion of the oscillating disk and ensure that torques sufficient to shear the grains are applied. It is therefore possible to investigate the behaviour of a system driven at very small amplitudes and to determine whether there is some critical *strain* below which the system begins to exhibit solid-like behaviour.

Chapter 5

Equipartition in a 2D granular gas

5.1 Introduction

Statistical mechanics is very good at describing ideal gases. But what happens if the particles in the system are large and densely packed and dissipate energy through collisions and friction? Many processes operate far from equilibrium and therefore cannot be described within the framework of classical thermodynamics and statistical mechanics [67]. One of the simplist non-equilibrium systems is the granular gas, composed of driven, colliding macroscopic particles [68]. Such a system differs from an ideal gas in two important ways: because collisions are inelastic, energy input is required to maintain a gaseous state; and the finite particle size causes steric effects in which free volume is not always accessible because the path to an empty region is blocked by other particles. Granular gases can exist in a non-equilibrium steady state (NESS) in which energy flows into the system from an injection mechanism and out of the system via dissipation. Studying granular gases allows us to examine the extent to which such a steady-state can be described using the techniques of conventional statistical mechanics.

While there has been a great deal of success describing dilute granular gases using a Chapman-Enskog expansion of the Boltzmann equation [69, 70], kinetic theory approaches break down as the density of the gas increases [68]. For example, experiments on granular gases have observed non-Gaussian velocity distributions [29–33], the absence of equipartitioned kinetic energy (or temperature) in mixtures of different particles [29, 71, 72], and the breakdown of molecular chaos due to velocity correlations [73]. These failures, together with simulations which observe strong correlations between translational and rotational velocities [74], raise the question of how such systems partition energy between rotational and translational modes. In this Chapter, we present an experiment which, remarkably, exhibits equipartition between rotational and translational modes.

In equilibrium systems, the macroscopic properties can be described by an equation of state (EOS). The temperature of such a thermodynamic system can be defined in several equivalent ways:

1. by the total kinetic energy per degree of freedom, $E = \frac{1}{2}k_B T$,
2. by the width of the velocity distributions
3. with the Fluctuation-Dissipation Theorem
4. by the derivative of the entropy with respect to temperature, dS/dT

It remains an open question whether these microscopic and macroscopic temperatures are also equivalent in systems which exhibit a non-equilibrium steady state (NESS) [75]. Simulations of sheared foams [76] and experiments on fluidized spheres [77] indicate that several such measures of the temperature are equivalent, however it is still an open question to what extent these measures depend on the dynamics of the system. Previous experiments on vigorously shaken spheres indicate that velocity distributions are non-Gaussian and energy is not partitioned equally between light and heavy particles [29,71]. Meanwhile, simulations of shaken particles in three dimensions suggest that the way energy is partitioned between rotational and translational modes depends on the tangential restitution coefficient [78, 79]. Finally, a third measure of the temperature can be obtained with the Fluctuation-Dissipation Theorem. The FDT has also been tested in toy models [75], which suggest that the correlation and response functions have different characteristic time scales, indicating that the FD temperature is ill-defined. However, experiments on a rachet [80] indicate that the correlation and response function have the same characteristic time scale, although the ratio of these two quantities was slightly larger than the temperature as determined from the kinetic energy.

To relate the macroscopic state variables (pressure, volume, energy) with the microscopic translational and rotational motion of individual particles, we perform experiments on a dense granular liquid composed of a single layer of bidisperse disks[1]. The particles float on an air hockey

[1]This apparatus was originally developed by Frederic Lechenault and James Puckett in the Complex Matter group of Karen Daniels at North Carolina State University. The experiments described in this Chapter were performed while I was a visiting researcher in Karen's group.

table and are driven by impulses from bumpers at the boundaries. We find that the velocity distributions are exponential in character and that they are remarkably unaffected by varying ϕ, changing friction and restitution coefficients, by introducing geometric order into the system or by switching from constant pressure to constant volume boundary conditions. The time-averaged energy of the system is a constant independent of the packing fraction and pressure, which suggests that the bumpers driving the system function in a manner analagous to a thermal bath. Because large injections of energy occur irregularly and are followed by rapid cooling, our system appears to experimentally realize the predictions of Ben-Naim *et. al* [81, 82] in which rare, high-energy injections produce a well-mixed steady state with broad velocity distributions.

As in prior experiments on a monodisperse system of vertically-vibrated spheres [83] we are able to identify a gas-like equation of state (EOS) with a van der Waals correction. This EOS suggests that thermodynamic-like descriptions are valid even for highly far-from-equilibrium systems. Finally, we test the utility of the Fluctuation-Dissipation Theorem by perturbing the area under the piston and observing the subsequent relaxation and fluctuations. We find that the the relaxation process and the correlation function are exponential in time and proportional to one another, suggesting that the FD Theorem is applicable to our system. However, values of the temperature obtained from Fluctuation-Dissipation measurements are ≈ 3 times smaller than temperatures obtained from measuring the kinetic energy of the system.

5.2 Apparatus

In this experiment, we measure both the translational and rotational trajectories of bidisperse particles floating in a single layer on an air table [84, 85]. The particles are made from standard plastic petri dishes and are driven on three sides by impulses from 36 electromagnetic bumpers (Fig. 5.1) which provide fixed-velocity impulses at a fixed firing rate. Along the $+y$ and $-y$ sides of the table the bumpers are triggered in pairs so that bumpers facing each other fire at the same time. The bumper pairs in the y direction and the bumpers along the $-x$ side of the table are triggered randomly with a pre-generated random sequence. Four pairs of bumpers are randomly fired every 0.1 s, and travel 1 cm into the granular pack;

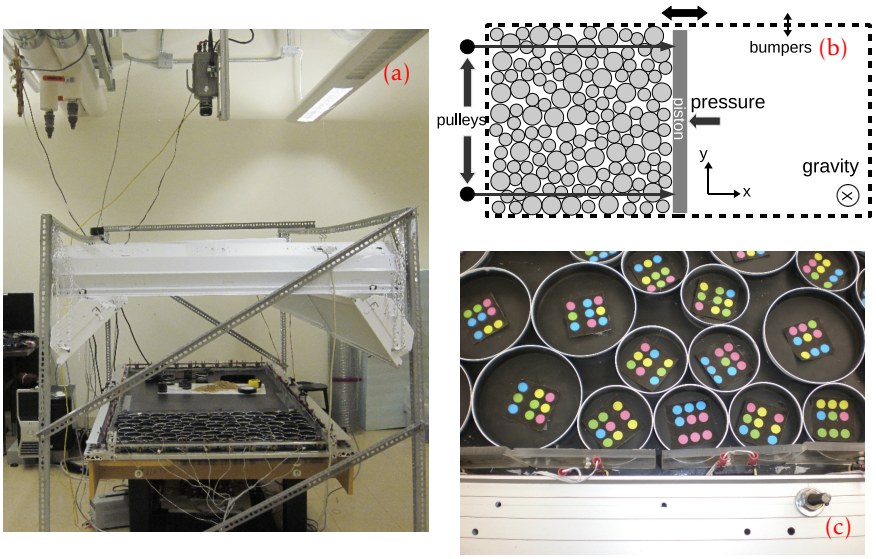

FIGURE 5.1: (a) The high speed camera is suspended above the air hockey table. (b) Schematic of the air hockey table, as seen from above. Bumpers fire from the boundaries in the $+x$, $+y$ and $-y$ directions. The piston can be fixed to create a constant volume (CV) system or left free, generating a constant pressure (CP) system. (c) The particles are tagged with a pattern of nine dots which allows the identity and orientation of each particle to be tracked. The plastic bumpers are visible along the edge of the table.

the total time over which the bumpers extend into the packing is approximately 0.1 s.

The system is constrained on the fourth side by a piston ($M = 439$ g) which also floats on the air table. The position of the piston can be fixed to create a constant volume system (CV), while a constant pressure system (CP) is produced by suspending masses on lines which run from the piston to pulleys on the opposite side of the table. The 2D "pressures" exerted on the system range from 0.01 N/m to 0.1N/m. (Note that pressures in this experiment are equivalent to twice the pressures reported in [85]. In addition, the piston used by Puckett *et. al.* has been modified by the addition of two arms at either end of the piston (Fig. 5.2) which prevent the device from rotating significantly.) We have primarily investigated amorphous packings in the range $0.61 < \phi < 0.79$, which corresponds to

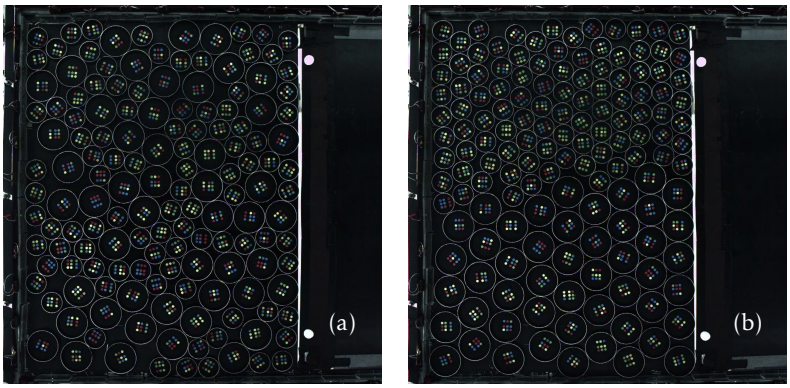

FIGURE 5.2: Particles on the air table, as seen from above. The particles can be distributed amorphously (a) or arranged in a hexagonally ordered state where the large particles are place on the $-y$ portion of the table and the small particles are placed on the $+y$ portion of the table (b). The position of the piston is tracked using the the white dots. The arms of the piston are visible in the right top and bottom of each image.

a system containing 147 to 186 particles. These densities which lie below the point at which the static jamming transition occurs [86, 87]. The upper limit on the density is set by random loose packing while the lower limit is set by the requirement that the particle density near the boundary must be high enough that firing bumpers will contact a particle. In addition to examining the behavior of amorphous packings, we have also studied hexagonally ordered packings in which the system was prepared with all of the small particles on the $+y$ side of the table and all of the large particles on the $-y$ side (Fig.5.2).

5.2.1 Particle properties and moments of inertia

The experiments described in this Chapter have been conducted on bidisperse particles to prevent the system from crystallizing and to allow us to study how energy is partitioned between different species. The particles are made from plastic petri dishes which are painted black and individually labelled by taping a square of paper marked with coloured dots to the centre of the particle. The large particles have radius $r_L = 41.8$ mm while for small particles $r_S = 27.9$ mm. We prepare the system so that the

area covered by large and small particles is equal. Since $(r_L/r_S)^2 = 2$, this requires $N_S = 2N_L$.

We can change the coefficients of friction and restitution by adding elastic bands to the circumference of the petri dishes. Because the sides of the particles slope inwards, the thickness of the rubber band does not significantly change the radius of the particles. For bare petri dish contacts, the coefficient of friction is $\mu = 0.5$ and coefficient of restitution is $\epsilon = 0.33 \pm 0.03$ [84]. The friction and restitution coefficients can be adjusted by stretching an elastic band around each of the particles so that the diameter remains unchanged; this results in $\mu' = 0.85$ and $\epsilon' = 0.51 \pm 0.07$ [84]. (All variables describing the banded particles are denoted with the prime.) The masses of the bare dishes are $m_L = 8.13 \pm 0.20$ g and $m_S = 3.52 \pm 0.12$ g. With the addition of rubber bands, the mass of the disks increases to $m'_{S,L} = m_{S,L} + 0.44$ g.

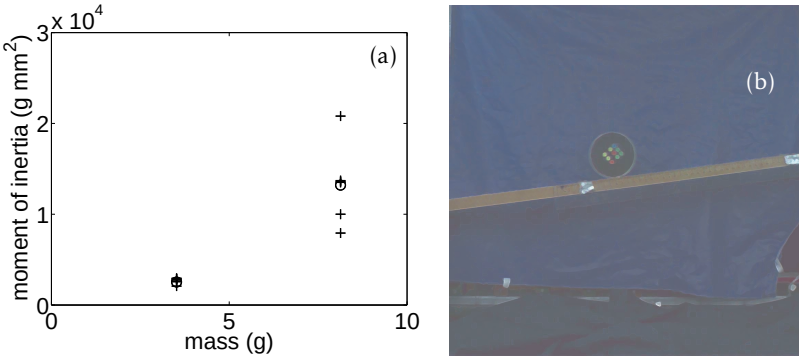

FIGURE 5.3: (a) Measured (+) and calculated (o) moments of inertia. (b) A sample frame from an experiment in which the particle rolls down an inclined plane.

The moments of inertia of the large and small particles can either be calculated from the geometry of the particles or by measuring the position and velocity of the particles as they roll down an incline (Fig.5.3b). The particles consist of a disk with a lip of height 13.5 mm, so the moment of inertia is given by the sum of the moment of the disk and the moment of a hollow cylinder. The material in the lip of the particle is slightly thicker than in the disk, so the upper limit on I can be determined by assuming the mass is entirely at the radius of the disk. $I_{max} = mr^2 = 2.7 \times 10^3$ g/mm^2 for the small particles and 1.4×10^4 g/mm^2

for the large. A lower limit on the moment of inertia can be obtained by assuming that the mass is uniformly distributed through the disk and cylinder. $I_{min} = 0.75mr^2 = 2.0 \times 10^3$ g/mm^2 for the small particles and $I_{min} = 0.7mr^2 = 1.0 \times 10^4$ g/mm^2 for the large. A more realistic value of I is obtained by a better approximation of the mass distribution which reflects the thicknesses of the plastic in the disk and the lip of the petri dish: $I = (0.8m)r^2 + (0.5)(0.2m)r^2 = 2.5 \times 10^3$ g/mm^2 for the small particles and $I = (0.75m)r^2 + (0.5)(0.25m)r^2 = 1.3 \times 10^4$ g/mm^2 for the large. When rubber bands are placed on the particles, the mass is added entirely at the particle radii so that the moments of inertia increase to $I'_S = 2.8 \times 10^3$ g mm^2 and $I'_L = 1.4 \times 10^4$ g mm^2.

The moments of inertia can also be measured experimentally by taping two particles back-to-back and allowing them to roll down an inclined plane. We film the motion with the same high speed camera used in the particle tracking experiments (Section 5.2.2) and use the particle trajectories to calculate the velocities. Since $mg\Delta h = \frac{1}{2}m\Delta v^2 + \frac{1}{2}\Delta\omega^2$, energy conservation can be invoked to determine the moment of inertia. The measured values of the moments of inertia for the small and large particles are indicated in Fig.5.3a. The experimentally measured values of I are $2.66 \pm 0.32 \times 10^3$ for the small particles and $1.33 \pm 0.44 \times 10^4$ for the large particle. These values are consistent with the values calculated from the particle geometry as described above.

5.2.2 Particle tracking

Each particle is tagged with a unique nine-dot pattern (Fig.5.1b) which allows the identity, position and angular orientation to be determined. We image the system using a Phantom V5.2 high speed camera and determine the translational (v_x, v_y) and rotational (ω) velocities from the trajectory of each individual particle. Uniquely tagging each particle eliminates error caused by confusing the identities of two particles [88].

One error in the measurement of particle velocities is caused by undersampling: a finite difference velocity measurement taken during a collision will be lower than the actual velocity because the path travelled by the particle is longer than the difference between the final and initial positions. The effect is particularly noticeable at high ϕ, where particles undergo the most frequent collisions.

We can test to see if the image acquisition rate is high enough by ex-

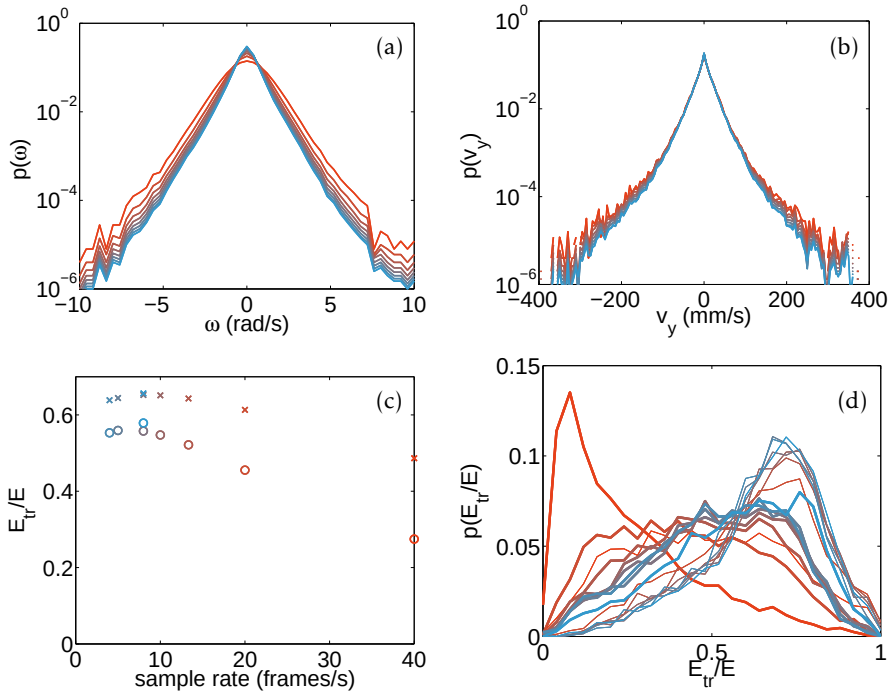

FIGURE 5.4: $\mathcal{P}(v_y)$ (a) and $\mathcal{P}(\omega)$ (b) distributions at different sample rates for the large particles. The line colour corresponds to the frame rate indicated in panel (c). (c) The the time-averaged ratio of translational energy to the total energy, $\langle E_{tr}/E \rangle$ converges for the small particles ($\times$) and large particles ($\circ$) at a sample rate of 10 frames/s. This frame rate maximizes the resolution of the velocity of fast particles while minimizing noise in the velocity of slow moving particles. The particle velocities are calculated using a finite difference method except for the points indicated by the square and $+$ which indicate that the velocities were calculated by taking the Fourier transform of the trajectories sample at 40 frames/s. (d) The distribution of $\langle E_{tr}/E \rangle$ converges at a sample rate of 10 frames/s. (The system is prepared at CV with 62 large particles and 124 small particles so that$\phi = 0.756$.)

amining the velocity distributions for a single experiment. The available position data can be undersampled at different rates to check to see if the sampling rate is high enough. At very high sample rates, the algorithm is more successful at resolving the velocities of very fast particles and the tails of the velocity distributions are wider than the tails at lower

sample rates (Fig.5.4a,b). However, at high sample rates, the position of a slow-moving particle in two subsequent frames does not change very much and the velocity is dominated by noise. The convergence of the velocity distributions can be additionally confirmed by examining the time-average value of the ratio of the translational energy to the total energy ($\langle E_{tr}/E \rangle$). (These quantities are defined and discussed more thoroughly in Section 5.6, however, it is helpful to examine the energy distributions here because the total energy of the system is less sensitive to fast-moving but infrequently observed particles which dominate the tails of the velocity distributions.) The distributions of $\langle E_{tr}/E \rangle$ converge at a sample rate of 10 frames/s (5.4c,d). The velocity distributions (Fig.5.4a,b) do narrow slightly when the sample rate is reduced from 40 frame/s to 4 frames/s, however the loss of resolution at high velocities does not influence the value of the average energies (Fig.5.4c,d).

The velocity resolution can also be improved by using a Fourier transform to take the derivative of the particle trajectories. The high frequency noise (above 5 Hz) is filtered out and a 5-point boxcar averaging scheme is employed to smooth the trajectories. This scheme produces the same results as the finite difference method (Fig.5.4c,d).

By tracking the positions and angular orientations of of undriven particles (Fig.5.5), we can calculate a lower bound on the translational velocity resolution (± 2 mm/s) and the rotational velocity resolution (± 0.4 rad/s). The width of these distributions is small compared to the mean rotational and translational speeds of a driven system (Fig.5.4).

A 40 Hz frame rate allows the motion of the particles to be filmed for 100 s. The duration of each experimental run is limited by the number of frames which can be stored on the camera (4096). Each measurement is taken after the system has equilibrated for 1 minute. Constant volume data sets consist of $1-4$ runs at a given ϕ, while constant pressure data sets consist of $1-4$ runs at a given pressure.

5.3 Velocity distributions

A simple comparison of the microscopic behaviour of our system with that of an ideal gas can be made by examining the velocity distributions of the particles. The velocities of particles in an ideal gas are random, so the velocity distributions are Gaussian with a variance equal to $k_B T/m$. How-

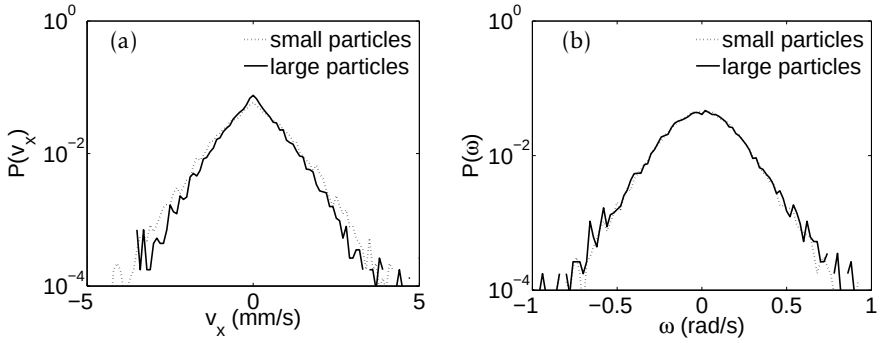

FIGURE 5.5: Distribution of measured translational velocities (a) and angular velocities (b) for a stationary system. The width of the distribution indicates the error in the velocity measurements (± 2 mm/s for the translational velocities and ± 0.4 rad/s for the rotational velocities). The width of theses distributions is small compared with the mean speeds of driven systems (Fig.5.4).

ever, we find that the translational velocity distributions of the particles ($\mathcal{P}(v_x)$ and $\mathcal{P}(v_y)$) are approximately exponential in character. The distributions are also the same for both the large and small particles (Fig. 5.6a,b), which means that there cannot be equipartition of energy between the two species. Simulations of bidisperse particles [89] have also found that the velocity distributions for each of the large and small particles are the same, although the distributions found there had a more Gaussian shape. One reason that the velocity distributions for the large and small particles might be the same is that motion of the particles must necessarily be highly correlated because the system is very dense: the movement of a particle in a given direction obligates neighbouring particles to move in the same direction.

We have made two observations which suggest that the broader-than-exponential tails of the translational velocity distributions are due to high speed particles near the bumpers. First, we find that $\mathcal{P}(v_x)$ is asymmetric because the piston does not drive particles in the $-x$ direction (Fig. 5.6a). Secondly, if we restrict $\mathcal{P}(v_y)$ so that only particles more than $3r_L$ from the boundaries are included in the distribution, then a more exponential form is recovered (Fig. 5.6c). We conclude that the non-exponential tails arise from the highest-speed particles near the bumpers. Finally, the high velocity tails for the small particles are slightly wider than for the large

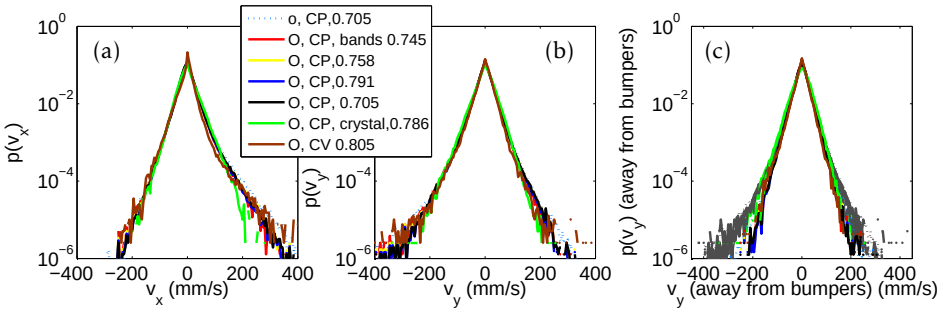

FIGURE 5.6: (a,b) Translational velocity distributions $\mathcal{P}(v_x)$ and $\mathcal{P}(v_y)$ for large particles (solid lines) and small particles (dashed lines). (c) $\mathcal{P}(v_y)$ for particles which are at least $3r_L$ from the bumpers. The distributions from (b) are plotted in the background in grey. The mean of the absolute value of the velocities are: $\langle|v_x|\rangle = 19.4 \pm 1.5$ mm/s, $\langle|v_y|\rangle = 19.9 \pm 1.5$ mm/s, and $\langle|v_y|$(for particles $> 3r_L$ away from bumpers)$\rangle = 19.3 \pm 2.0$ mm/s.

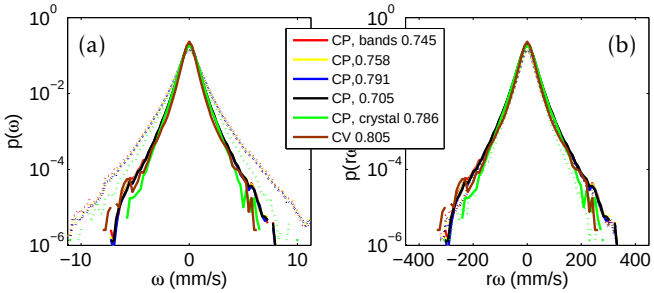

FIGURE 5.7: (a) $\mathcal{P}(\omega)$ for large particles (solid lines) and small particles (dashed lines) at different densities, boundary conditions (CP, CV) and with and without bands. (b) Distributions of the angular velocity rescaled with the particle radius, $\mathcal{P}(r\omega)$. The mean of the absolute value of $\langle|r\omega|\rangle = 20.9 \pm 1.6$ mm/s.

particles, which suggests that the small particles acquire a slightly larger velocity from the bumpers.

The angular velocity distributions $\mathcal{P}(\omega)$ are also approximately exponential, but unlike $\mathcal{P}(v)$, the behaviour of the large and small particles can be distinguished: $\mathcal{P}(\omega)$ is wider for the small particles than for the large (Fig. 5.7a). The angular velocity distributions for a hexagonally ordered system are slightly narrower than the distributions for the amorphous systems. The angular velocity distributions scale with the particle radius so

that $\mathcal{P}(r\omega)$ is the same for both large and small particles (Fig. 5.7b).

The shapes of all three $\mathcal{P}(v_x, v_y, \omega)$ distributions are surprisingly immune to changes in the system: switching from CP to CV boundary conditions, varying the packing fraction and tuning μ and ϵ by adding elastic bands leave velocity distributions unchanged. This suggests that geometric rather the kinematic constraints determine the motion of the particles.

5.4 Behaviour of particles in contact

We have already seen (in Sec 5.3) that the angular velocity distributions scale with the particle radii. This observation suggests that the particles have a preference for rolling contacts. Because the ensemble is dense, each particle has several neighbours which are either touching or nearly touching. Many of these neighbours are also themselves in contact which each other, which means that the system is frustrated: if two of three particles mutually in contact are rolling, the third particle must slide along at least one of the two particles. In this Section we will quantify the preference for rolling contacts and compare the dynamics of particles with different numbers of contacts.

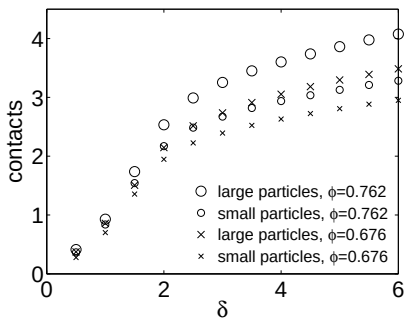

FIGURE 5.8: The number of contacts per particle enumerated as a function of δ, the contact sensitivity. The number of contacts increases more slowly for $\delta > 2$, indicating that the real contacts have been enumerated. Particles closer than $r_1 + r_2 + \delta$ are therefore considered to be touching. The two systems described in the plot are both CV and have different densities.

Because the image resolution is finite it is not possible to strictly determine if two particles are in contact or not. However, it is still possible to identify of pairs of particles which are at least known to be either touching *or* very nearly touching. This is accomplished by looking for neighbouring particles separated by a distance $(x_2 - x_1)^2 + (y_2 - y_1)^2 < (R_1 + R_2 + \delta)^2$. The parameter δ is a small number on the order of the resolution of the particle positions. The value of δ needs to be large enough that particles

in contact are not excluded from the count of touching or nearly touching pairs. The value of δ is selected by examining how the number of contacts changes as δ is modified (Fig.5.8).

The width of both the translational velocity and angular velocity distributions decreases slightly as the number of contacts per particle increases (Fig.5.9). Particles with two or more contacts are much more likely to be in frustrated configurations which require that at least some of the touching particles are sliding against each other. Since sliding contacts dissipate energy, particles with many contacts should be expected to have lower velocities.

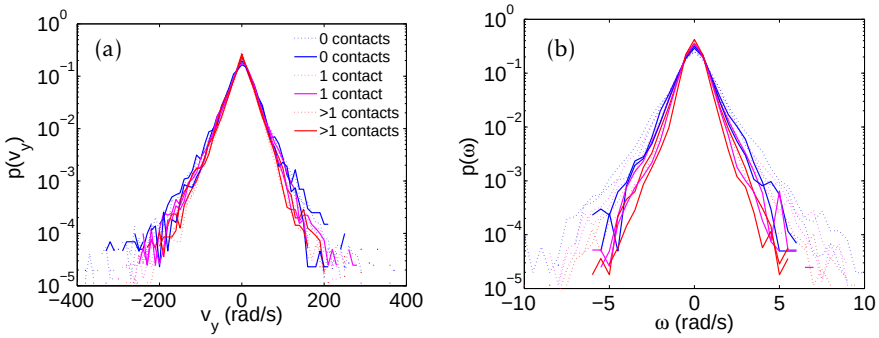

FIGURE 5.9: (a) Translational velocity (v_y) distributions for large particles (solid lines) and small particles (dashed lines). (b) Rotational velocity distributions for large and small particles. Particles which are touching more of their neighbours have narrower velocity distributions than those which are not in contact with other particles. (CV system, $\phi = 0.755$.)

The observation that the angular velocity distributions scale with the particle radii suggests that the particles prefer rolling contacts. The preference of the system for rolling contacts over sliding contacts can also be observed by examining the difference between the velocity components parallel to the disk surface at the point where two disks are in contact. We define the difference between the two velocities, Δ, as:

$$\Delta = |\vec{\omega_1} \times \hat{r} r_1 - \vec{\omega_2} \times \hat{r} r_2 + \vec{v_1} \times \hat{r} - \vec{v_2} \times \hat{r}| \tag{5.1}$$

The velocities of each of the two particles are $\vec{v_1}$ and $\vec{v_2}$, while the unit vector $\hat{r} = \vec{r_2} - \vec{r_1}$. The rotational velocities of each particle at the contact point are $\vec{\omega_1} \times \hat{r} r_1$ and$\vec{\omega_2} \times \hat{r} r_2$ while the translational contribution along

the direction parallel to the surface of each particle is $\vec{\omega_1} \times \hat{r} r_1$ and $\vec{\omega_2} \times \hat{r} r_2$. When the particles are rolling, the relative speed of the contact points of the two particles approaches 0; as the particles begin to slide, the relative speed of the contact points increases. The distribution of the values of Δ (Fig. 5.10) has a peak at 0 mm/s, indicating that the system prefers to minimize the difference between the velocities of the contact points of two particles which are touching each other: the system prefers rolling contacts.

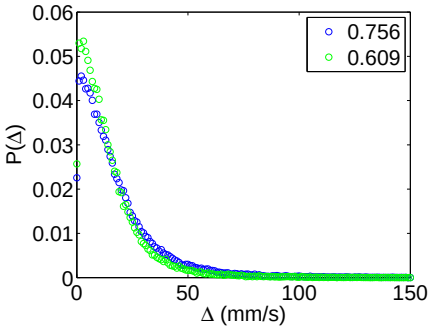

FIGURE 5.10: Probability distribution of the difference between the velocities of the contact points of two particles. The peak at 0 mm/s indicates that the particles prefer to have rolling contacts.

Sliding contacts dissipate more energy than rolling contacts because the coefficient of rolling friction is always lower than the coefficient of sliding friction. That sliding contacts dissipate much more energy than rolling contacts and that the system has a preference for rolling contacts over sliding contacts suggest that one of of the principles governing how the system determines the motion of the particles is that the rate at which energy is dissipated should be minimized.

5.5 Energy injection

Although two bumpers fire ten times every second, the amount of energy injected is irregular (Fig.5.11). This is likely because force chains linking particles in contact are able to distribute energy more efficiently than particles with few contacts, so the local geometry of the particles near the bumpers affects how energy is injected into the system. The energy is also rapidly dissipated, which suggests that energy is quickly transferred from a few fast particles to the slower particles. This behaviour suggests that our system realizes Ben-Naim *et. al.*'s prediction [81, 82] that a power-

ful injection mechanism produces a well-mixed steady state in which the particle velocities are broadly distributed. However, our velocity distributions are nearly exponential, whereas the velocity distributions in the simulations of Kang *et. al.* have power-law tails.

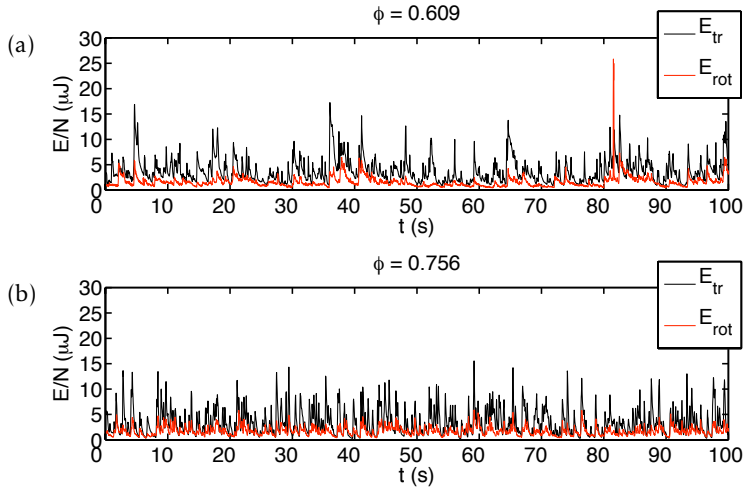

FIGURE 5.11: Average rotational and translational energy per particle as a function of time for a dense system (a) and a very dense system (b).

As indicated in Fig.5.11, the rotational energy is rarely significantly larger or smaller than the translational energy and spikes in the translational energy typically occur at the same time as spikes in the rotational energy. In the following Section, we will examine the way in which energy is partitioned between the translational and rotational modes.

5.6 Equipartition

The time average of total kinetic energy of the system, $\bar{E}$, is the sum of the translational ($\bar{E}_{\rm tr}$) and rotational ($\bar{E}_{\rm rot}$) energies of all the particles ($i = 1..N$) in the system:

$$E = \sum_i \frac{1}{2} m_i \langle v_{i,x}^2 \rangle + \sum_i \frac{1}{2} m_i \langle v_{i,y}^2 \rangle + \sum_i \frac{1}{2} I_i \langle \omega_i^2 \rangle. \tag{5.2}$$

The rms velocities, $\langle\cdot\rangle$, are averaged over time. In equilibrium thermal systems, equipartition requires that each degree of freedom has the same energy; however, no such requirement exists for non-equilibrium systems. As shown in Fig. 5.6, we observe that the large and small particles have the same $\mathcal{P}(v)$, indicating that translational energy is not partitioned equally between the two species. However, the system *does* partition the energy equally between the two translational and one rotational degree of freedom: as shown in Fig. 5.12, the average value of $\langle E_{\rm tr}/E\rangle$ is approximately $2/3$. This observation holds for both bare and banded particles and for both CP or CV boundary conditions, although the ratio $E_{\rm tr}/E$ decreases slightly with increasing ϕ (or P).

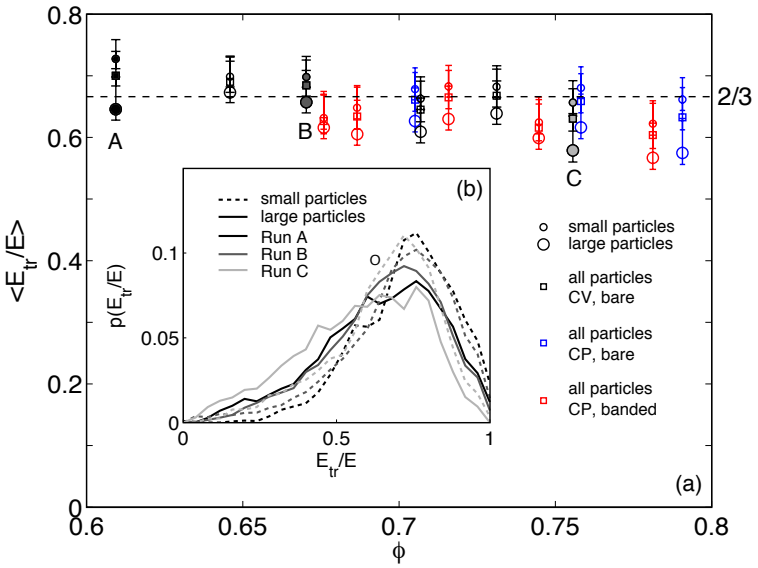

FIGURE 5.12: Time-averaged ratio of the translational kinetic energy to the total kinetic energy $\langle E_{\rm tr}/E\rangle$ averaged over 100 s. The ratio of translational energy to the total kinetic energy expected for a two-dimensional system is $2/3$ (dashed black line). Inset: Probability distribution of $\langle E_{\rm tr}/E\rangle$ at for three different densities at constant volume.

We have seen that the system requires that the translational velocity distributions for the large and small particles are the same (Fig.5.6) and that and that the system has a preference for rolling contacts which re-

quires that $\mathcal{P}(r_S\omega) = \mathcal{P}(r_L\omega)$ (Fig. 5.7b). However, many different pairs of $\mathcal{P}(\omega_S)$, $\mathcal{P}(\omega_L)$ can satisfy this requirement - the system is still not completely constrained. The missing constraint is provided by the equipartition of $\bar{E}_{\rm tr}$ and $\bar{E}_{\rm rot}$:

$$(N_S m_S + N_L m_L)\langle v_{x,y}^2\rangle = N_S I_S \langle\omega_S^2\rangle + N_L I_L \langle\omega_L^2\rangle. \tag{5.3}$$

The moment of inertia can be written as $I_i = \alpha_i m_i r_i^2$, where α is a coefficient indicating how the mass is distributed over the particles, with $\alpha_S = 0.97$, and $\alpha_L = 0.94$. Eq. 5.3 can be satisfied for any two values of α_L and α_S when $\mathcal{P}(r_S\omega) = \mathcal{P}(r_L\omega)$ and $\mathcal{P}(v_S) = \mathcal{P}(v_L)$. If the translational velocity distributions and the distributions of $r\omega$ are the same for both particles, then there is one degree of freedom left for the system to pick a pair of velocity distributions which will satisfy equipartition! Another way to think of this is to consider the angular velocity distributions, which have the form $e^{-a|\omega_L|/r_L}$ and $e^{-a|\omega_S|/r_S}$, where a is any constant. These functions satisfy the requirements for rolling contacts for any value of a selected by the ensemble. In other words, the system is able adjust the widths of the translational and rotational velocity distributions so that both the geometrical preference for rolling contacts and the energetic preference for equipartition can be satisfied.

The observation that $\langle E_{\rm tr}/E\rangle$ is systematically lower for the large particles than for the small follows from the observation that $\alpha_L < \alpha_S$. This is because there can only be equipartition of the rotational and translational energy in both the ensemble of large particles *and* the ensemble of small particles if $\alpha_L = \alpha_S$. If $\alpha_L \neq \alpha_S$, then there can be equipartition of the rotational and translational energy over the entire system, but not in both the ensemble of small particles and the ensemble of large particles.

5.7 Equation of state

In equilibrium statistical mechanics the temperature is proportional to the total kinetic energy of the system (Eq 5.2). One surprising observation is that although the total energy of the system fluctuates considerably over time, the average energy is a constant independent of the packing density (Fig. 5.13a). There is no obvious physical reason why the total energy of the system should be independent of the packing density and many other experiments on granular gases do observe that the velocity distributions

broaden or narrow as the packing density changes [29,30,32]. The average energy is also independent of whether the system is constant pressure or constant temperature. This observation, together with the fact that the average energy is independent of the packing fraction, suggest that the action of the bumpers is analogous to having our system immersed in a thermal bath, where the time-averaged total kinetic energy $\bar{E}$ is equivalent to $1.5K_BT$.

In 2D, the pressure exerted by the piston is given by a force per unit length, so that $P = F/L$ and PA has units of energy. Guided by work on vibrated granular crystals [83], we apply a van der Waals-like correction to account for the excluded area. The free area available to the particles is the area under the piston A, excluding the area occupied by the particles and the interstices which are too small to accommodate another particle. This excluded area is given by $A^* \equiv (N_S\pi r_S^2 + N_L\pi r_L^2)/\phi^*$, where ϕ^* is a maximum packing density. In an ideal gas $PA = E$, but dense systems are harder to compress because rearrangements can be more difficult to access. This effect introduces an additional factor of $(1 + \chi)$ in the EOS [90]. The compressibility factor χ is proportional to $1 + \epsilon$ (the restitution coefficient) and to the pair correlation function $g(r)$ evaluated at the particle radius. Including all three considerations, we examine the following EOS:

$$P(\bar{A} - A^*) = \bar{E}(1 + \chi). \tag{5.4}$$

In our experiment, we observe that $\bar{E}/N$ is fixed by the action of the bumpers (Fig. 5.13a). We therefore vary P and observe A. Fig. 5.13b shows Eq. 5.4 for both bare and banded particles, plotted on a per-particle basis for fixed N. There is a linear relationship between A and P and the intercept corresponds to the excluded area, A^*. For $P/N \lesssim 50$ mN/m, the fluctuations in the area under the piston are large and the system does not behave as though it is in a steady state on the time scale of the experiment. From a least-squares fit, we determine $\phi^* = 0.802 \pm 0.002$ and $\phi'^* = 0.804 \pm 0.010$ for the bare and banded particles respectively. For comparison, the local values of static random loose packing measured in an undriven system [84] are $\phi_{\mathrm{RLP}} = 0.81$ for both bare and banded particles [2]. Our measured ϕ^* are less dense than maximally dense static state and

[2]Note than in the experiments of Lechenault *et. al.* [84] the system was generated by placing the table at a 0.3° angle and allowing individual particles to slide down to the low end, creating the loosest possible packings. Because this protocol does not guarantee that the loosest possible stable packs are achieved, the values of ϕ_{RLP} are upper bounds.

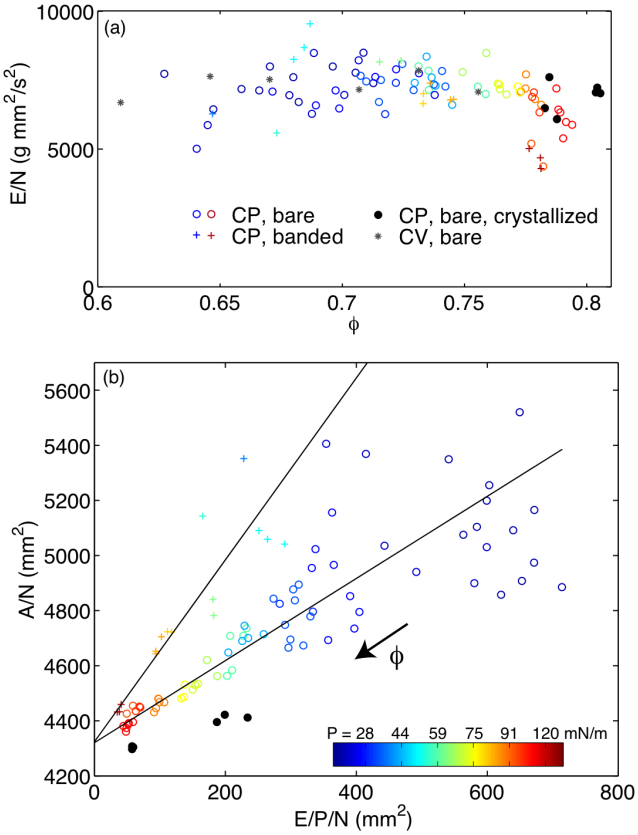

FIGURE 5.13: (a) Average energy per particle ($N = 147$) as a function of ϕ. The dots for CP systems indicate the mean energy and area for 25 s of data (ϕ for CV systems is constant). (b) Equation of state. The slope for the system with elastics is 3.7 ± 0.3, the slope for systems with bare particles is 1.54 ± 0.04 and the slope for crystallized bare particles is 0.72 ± 0.07. The pressure of the system is indicated by the symbol color.

correspond closely to the kinetically-determined value of ϕ_{RLP}. However, note that the values of ϕ_{RLP} reported in [84] are *local* values, whereas the values of ϕ^* which we measure in our experiments are *global* values. Meanwhile, in our hexagonally ordered system, $\phi^*_{\mathrm{cryst}} = 0.812 \pm 0.002$, which is much less dense than the hexagonally close packed value $\phi_{\mathrm{HCP}} = 0.91$. The value of ϕ^*_{cryst} is substantially less dense than ϕ_{HCP} because our sys-

tem is small and the packing efficiency along the boundary between the large and small particles and along the edge of the table near the bumpers is poor (Fig.5.2).

The slope of the equations of state plotted in Fig 5.13 correspond to $1+\chi$, where χ is the compressibility. For bare particles, $1+\chi = 1.54 \pm 0.04$, for banded particles $1 + \chi' = 3.7 \pm 0.3$, and for crystallized bare particles $1 + \chi_{\rm cryst} = 0.72 \pm 0.07$. It is somewhat surprising that χ is *constant* as a function of the packing fraction: at high packing fractions it is more difficult for particles to rearrange and access the free area because the routes to these regions are blocked by other particles. This means that at high packing fractions a substantial increase in the pressure produces a much smaller decrease in the area compared to when the pressure is increased in system at a lower packing fraction [90]. In consequence, χ should be larger for high packing fractions than for low. Note that measurements in shaken monodisperse spheres [83] indicate that χ does increase dramatically close to crystallization. This suggests that something about the bidisperse character of our system or the way it is driven causes efficient collective motion which allows the compressibility to remain constant, even at high packing fractions.

Including the energy of the piston in the equation of motion modifies the value of $1 + \chi$ by a small amount: the slope for the banded particles decreases from 3.7 to 3.3 and the slope for the unbanded particles changes from 1.54 to 1.25 when the piston is included in the total energy of the system. When the energy of the piston is included, the values of the intercepts are not significantly different from the values obtained when the piston is excluded ($\phi^* = 0.800 \pm 0.002$, $\phi'^* = 0.809 \pm 0.01$ and $\phi^*_{\rm cryst} = 0.813 \pm 0.002$).

5.8 Fluctuation-dissipation temperature

In addition to direct measurements of the total kinetic energy, the temperature of a conventional thermodynamic systems can also be obtained from the Fluctuation-Dissipation Theorem. The FDT relates temperature to the time scale of fluctuations and relaxations in the system. For example, in low Reynolds number liquids, the FDT is manifested in the form of the Einstein-Stokes equation, which relates the temperature to the diffusivity and the viscosity of the liquid [91].

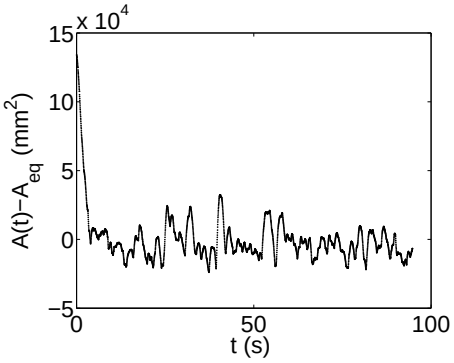

FIGURE 5.14: The evolution of the area under the piston for a sample FD experiment. At $t = 0$ the piston is released and begins relaxing rapidly towards the equilibrium value of the area. Near equilibrium the area under the piston undergoes substantial fluctuations.

We can also invoke the fluctuation-dissipation theorem to measure the temperature of our granular system. A perturbation with energy $\Delta(PV) = (1+\chi)(F/L)(A - A_{eq})$ can be generated by moving the piston away from equilibrium. When the piston is released it relaxes back to equilibrium with a characteristic time scale. The response function, $R(t) = (A(t) - A_{eq})$ is therefore given by the area under the piston at time t after the piston has been released. The correlation function, $C(t)$, quantifies the fluctuations in the piston position at equilibrium and is defined as $\langle (A(\tau + t) - A_{eq})(A(\tau) - A_{eq}))\rangle$. Finally, the FD "temperature" is given by the ratio of $C(t)$ to $R(t)$:

$$E_{FD} = (F/L)(1+\chi)\frac{\langle (A(T+t) - A_{eq})(A(T) - A_{eq}))\rangle}{A(t) - A_{eq}}. \qquad (5.5)$$

Prior to beginning an FD experiment, the piston is shifted in the $+x$ direction and fixed so that the system is at constant volume and the area of the system is larger than at equilibrium. The piston is fixed for one minute so that the system reaches a steady state. At the moment the piston is released the high speed camera begins recording the piston and particle positions (Fig.5.14).

In order to invoke the FD theorem, the change in the energy of the system must be linearly proportional to the perturbed quantity. Although we do not have enough measurements to conclusively demonstrate that the perturbation is in the linear response regime, the Equation of State developed in the previous section indicates that the energy scales linearly with the area under the piston, even at very high densities. That the perturbation in the energy is proportional to the change in the area under the

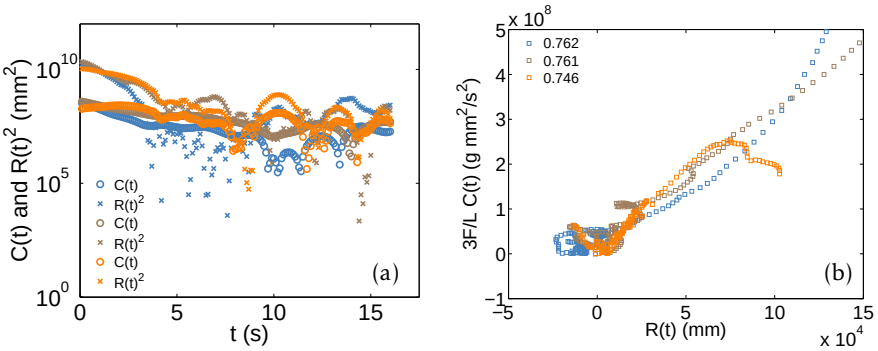

FIGURE 5.15: (a) $C(t)$ and $R(t)^2$ are both exponential in time. (b) $3F/LC(t)$ as a function of R(t) over the duration of the experiment. $(3F/L)C(t)/R(t)$ is linear and the slope indicates the FD temperature. The slope is ≈ 3 times smaller than the total kinetic energy, E of the system.

piston suggests that it is indeed reasonable to invoke the FD theorem in this system.

Like E, the FD temperature (Eq. 5.5) is the same for three systems at different pressures (Fig.5.15). However, the FD temperature that we measure is ≈ 3 times lower than E. There is not currently a theoretical framework with which to explain this discrepancy, however the fluctuations in the area under the piston are still of the same order of magnitude as temperature-like fluctuations would be in an ideal gas.

5.9 Conclusion

In order to examine how statistical mechanics might be adapted to describe granular systems, we have performed an experiment in which we track the translational and rotational motion of a dense system of bidisperse particles which float on an air table and are driven by electromagnetic bumpers. We find that the velocity distributions are approximately exponential and are independent of both packing fraction and particle properties. The translational velocity distributions are the same for both large and small particles, while the angular velocity distributions scale with the particle radius. Although energy is not partitioned equally between the large and small particles, we do observe equipartition between

the two translational and one rotational degree of freedom. Finally, we find that the system exhibits a van der Waals-like equation of state. These findings indicate that states *can* exhibit some properties of equilibrium statistical mechanics (such as equipartition of rotational and translational energy and Boyle's Law), they do not *necessarily* do so (the velocity distributions of the particles in our system are not Gaussian and energy is not partitioned equally between the large and small particles).

Comparisons with other experiments in different regimes provide some insight into which equilibrium properties are expressed in different granular fluids. In prior experiments and simulations on granular gases, translational velocity distributions are variously observed to have the form e^{-v^2} (dilute simulations [89,92]), $e^{-|v|^{1.5}}$ (horizontal quasi-2D vertical vibration experiments [29], vertical quasi-2D vertical vibration experiments [31], 3D vertical vibration experiments [32]), $e^{-|v|}$ (horizontal quasi-2D free cooling experiments [29] and quasi-2D vibration experiments in microgravity [30] and [33]). In our boundary-driven 2D system, we find that the velocity distributions are nearly exponential - and that the distributions become more exponential when fast particles near the bumpers are excluded. Our observations are consistent with those of Losert et. al. [29] who found that the velocity distribution of a driven granular gas possessed broader tails than for the same system in a freely cooling state; broad tails in the velocity distributions appear to be caused by driving the system in a non-uniform way so as to create an overabundance of very fast particles close to the energy source.

Because large bursts of energy are injected irregularly into our system, our experiment may realize the predictions of Ben-Naim *et. al* [81, 82] in which rare, high-energy injections produce a well-mixed steady state with broad velocity distributions. Although simulations of this driving mechanism find that the velocity distributions have power-law or stretched exponential tails (while we observed nearly-exponential tails), our system also exhibits a well-defined steady-state characterized by Boyle's law.

A second surprising observation we have made about the translational velocity distributions is that they are the same for both the large and the small particles. As a consequence, energy is not partitioned equally between the two particle species. Simulations [89] also indicate that energy is not partitioned equally between particles of different sizes. Moreover, other experiments on ensembles of particles made from different mate-

rials [29, 71, 72]) indicate that energy is not partitioned equally between particles with different properties. The absence of equipartition amongst particles with different restitution coefficients has been explained within the context of Chapman-Enskog expansions [93]. In addition, simulations [78,79] predict that the way energy is distributed between rotational and translational modes should depend on μ and ϵ; however, for the values used here, equipartition of $\bar{E}_{\rm tr}$ and $\bar{E}_{\rm rot}$ is not predicted.

Our observations of energy equipartition between the rotational and translational degrees of freedom are remarkable because equipartition is not observed in dilute granular gases with fully 3D motions [94]. The behaviour of the particles in our experiments suggest that energy equipartition may be a special property of rotationally symmetric particles in two dimensions: in a dense 2D system it is easier for a particle to move in a given direction if the neighbouring particles also move in the same direction with the same velocity. This restriction means that the translational velocity distributions for both the large and small particles need to be the same. Consequently, there cannot be equipartition of energy between the large and small particles. Meanwhile, in dense systems of circular or spherical particles, rotational motion is primarily restricted by friction. That $\mathcal{P}(r\omega)$ is the same for both the large and small particles suggests that there is a strong preference for rolling contacts, which is corroborated by quantifying the preference for rolling and sliding contacts using the rolling parameter, q. Our analysis suggests that once the preference for rolling contacts is fulfilled, the system is still not completely constrained and so the equipartition rule is used to select how energy is distributed amongst each spatial degree of freedom.

Finally, we have performed experiments which allow us to measure a temperature using the Fluctuation-Dissipation Theorem. Both the correlation function and the response function are exponential in time, which suggests that the ensemble behaves like a thermodynamic system. However, the temperature obtained from the FD measurement is 3 times smaller than the kinetic energy of the system. There is currently no known theoretical framework with which to explain this discrepancy. Because our results indicate that the correlation function and response function are somewhat temperature-like, further experiments to explore how the FD temperature depends on the pressure and particle properties are warranted.

Bibliography

[1] H. M. Jaeger, S. R. Nagel, and R. P. Behringer. Granular solids, liquids, and gases. *Rev. Mod. Phys.*, 68:1259, 1996.

[2] Y. Forterre and O. Pouliquen. Flows of dense granular media. *Annual Review of Fluid Mechanics*, 40:1, 2008.

[3] J. B. Knight, C. G. Fandrich, C.N. Lau, H. M. Jaeger, and S. R. Nagel. Density relaxation in a vibrated granular material. *Phys. Rev. E*, 51:3957, 1995.

[4] P. Umbanhowar and M. van Hecke. Force dynamics in weakly vibrated granular packings. *Phys. Rev. E*, 72:030301, 2005.

[5] O. Dauchot, G. Marty, and G. Biroli. Dynamical heterogeneity close to the jamming transition in a sheared granular material. *Phys. Rev. Lett.*, 95:265701, 2005.

[6] A.S. Keys, A.R. Abate, S.C. Glotzer, and D.J. Durian. Measurement of growing dynamical length scales and prediction of the jamming transition in a granular material. *Nature Physics*, 3:260, 2007.

[7] R.M. Nedderman. *Statics and Kinematics of Granular Materials.* Cambridge Univ. Press, Cambridge, UK, 1992.

[8] I. Goldhirsch. Rapid granular flows. *Annu. Rev. Fluid Mech.*, 35:267, 2003.

[9] P. Jop, Y. Forterre, and O. Pouliquen. A constitutive law for dense granular flows. *Nature*, 441:727, 2006.

[10] D.M. Mueth, G.F. Debregeas, G.S. Karczmar, P.J. Eng, S.R. Nagel, and H.M. Jaeger. Signatures of granular microstructure in dense shear flows. *Nature*, 406:385, 2000.

[11] C. T. Veje, D. W. Howell, and R. P. Behringer. Kinematics of a two-dimensional granular couette experiment at the transition to shearing. *Phys. Rev. E*, 59:739, 1999.

[12] J.A. Dijksman and M. van Hecke. Granular flows in split-bottom geometries. *Soft Matter*, 6:2901, 2010.

[13] D. Fenistein and M. van Hecke. Universal and wide shear zones in granular bulk flow. *Nature*, 425:256, 2003.

[14] D. Fenistein, J.-W. van de Meent, and M. van Hecke. Universal and wide shear zones in granular bulk flow. *Phys. Rev. Lett.*, 92:094301, 2004.

[15] D. Fenistein, J.-W. van de Meent, and Martin van Hecke. Core precession and global modes in granular bulk flow. *Phys. Rev. Lett.*, 96:118001, 2006.

[16] X. Cheng, J.B. Lechman, A. Fernandez-Barbero, G.S. Grest, H.M. Jaeger, G.S. Karczmar, M.E. Mobius, and S.R. Nagel. Three-dimensional shear in granular flow. *Phys. Rev. Lett.*, 96:038001, 2006.

[17] K. Sakaie, D. Fenistein, T. J. Carroll, M. van Hecke, and P. Umbanhowar. M.r. imaging of reynolds dilatancy in the bulk of smooth granular flows. *Europhys. Lett.*, 84:49902, 2008.

[18] M. Depken, J. B. Lechman, M. van Hecke, W. van Saarloos, and G. S. Grest. Stresses in smooth flows of dense granular media. *Europhys. Lett.*, 78(5):58001, 2007.

[19] A. Ries, D.E. Wolf, and T. Unger. Shear zones in granular media: Three-dimensional contact dynamics simulation. *Phys. Rev. E*, 76:051301, 2007.

[20] S. Luding. The effect of friction on wide shear bands. *Particulate Science and Technology*, 26:42, 2008.

[21] J. Török, T. Unger, J. Kertész, and D. E. Wolf. Shear zones in granular materials: Optimization in a self-organized random potential. *Phys. Rev. E*, 75:011305, 2007.

[22] M. Depken, W. van Saarloos, and M. van Hecke. Continuum approach to wide shear zones in quasistatic granular matter. *Phys. Rev. E*, 73:031302, 2006.

[23] G. Koval, J.-N. Roux, A Corfdir, and F. Chevoir. Annular shear of cohesionless granular materials: From the inertial to quasistatic regime. *Phys. Rev. E*, 79:021306, 2009.

[24] C.M. Gourlay and A.K. Dahle. Dilatant shear bands in solidifying metals. *Nature*, 445:70, 2007.

[25] O. Pouliquen and R. Gutfraind. Stress fluctuations and shear zones in quasistatic granular chute flows. *Phys. Rev. E*, 53:552, 1996.

[26] A.J. Kabla and T.J. Senden. Dilatancy in slow granular flows. *Phys. Rev. Lett.*, 102:228301, 2009.

[27] A. Baldassarri, A. Barrat, G. D'Anna, V Loreto, P Mayor, and A. Puglisi. What is the temperature of a granular medium? *J. Phys.: Condens. Matter*, 17:S2405, 2005.

[28] T. S. Majmudar and R. P. Behringer. Contact force measurements and stress-induced anisotropy in granular materials. *Nature*, 435:1079, 2005.

[29] W. Losert, D.G.W. Cooper, J. Delour, A. Kudrolli, and J.P. Gollub. Velocity statistics in excited granular media. *Chaos*, 9:682, 1999.

[30] É. Falcon, R. Wunenburger, P. Évesque, S. Fauve, C. Chabot, Y. Garrabos, and D. Beysens. Cluster Formation in a Granular Medium Fluidized by Vibrations in Low Gravity. *Phys. Rev. Lett.*, 83:440, 1999.

[31] F. Rouyer and N. Menon. Velocity Fluctuations in a Homogeneous 2D Granular Gas in Steady State. *Phys. Rev. Lett.*, 85:3676, 2000.

[32] K. Wang, H.-Q.and Feitosa and N. Menon. Particle kinematics in a dilute, three-dimensional, vibration-fluidized granular medium. *Phys. Rev. E*, 80:4, 2009.

[33] M. Hou, R. Liu, G. Zhai, Z. Sun, K. Lu, Y. Garrabos, and P. Evesque. Velocity Distribution of Vibration-driven Granular Gas in Knudsen Regime in Microgravity. *Microgravity Sci. Tech.*, 20:73, 2008.

[34] M. E. Möbius, G. Katgert, and M. van Hecke. Relaxation and flow in linearly sheared two-dimensional foams. *Europhys. Lett.*, 90:44003, 2010.

[35] E. Weeks and D. Weitz. Properties of Cage Rearrangements Observed near the Colloidal Glass Transition. *Phys. Rev. Lett.*, 89:095704, 2002.

[36] P. M. Reis, R. A. Ingale, and M. D. Shattuck. Caging dynamics in a granular fluid. *Phys. Rev. Lett.*, 98:188301, 2007.

[37] G. D'Anna, P. Mayor, A. Barrat, V. Loreto, and F. Nori. Observing brownian motion in vibration-fluidized granular matter. *Nature*, 424:909, 2003.

[38] A Sarracino, D Villamaina, G Costantini, and A Puglisi. Granular Brownian motion. *J. Stat. Mech. Theor. Exp.*, 2010:P04013, 2010.

[39] F. Lechenault, R. Candelier, O. Dauchot, J.-P. Bouchaud, and G. Biroli. Super-diffusion around the rigidity transition: Lévy and the Lilliputians. *Soft Matter*, 6:3059, 2010.

[40] F. Lechenault, O. Dauchot, G. Biroli, and J. P. Bouchaud. Critical scaling and heterogeneous superdiffusion across the jamming/rigidity transition of a granular glass. *Europhys. Lett.*, 83:46003, 2008.

[41] G. A. Caballero-Robledo and E. Clément. Rheology of a sonofluidized granular packing. *Eur. Phys. J. E*, 30:395, 2009.

[42] R. Candelier and O. Dauchot. Creep Motion of an Intruder within a Granular Glass Close to Jamming. *Phys. Rev. Lett.*, 103:128001, 2009.

[43] O Zik, J Stavans, and Y Rabin. Mobility of a Sphere in Vibrated Granular Media. *Europhys. Lett.*, 17:315, 1992.

[44] G. Caballero, J. Lanuza, and E. Clement. Compaction and mobility in randomly agitated granular assemblies. In S.Luding and H.Herrmann, editors, *Powders & Grains 2005*. Balkema, 2005.

[45] J. Geng and R. Behringer. Slow drag in two-dimensional granular media. *Phys. Rev. E*, 71:011302, 2005.

[46] G Hill, S Yeung, and S. A. Koehler. Scaling vertical drag forces in granular media. *Europhys. Lett.*, 72:137, 2005.

[47] H.M. Jaeger, S.R. Nagel, and R.P. Behringer. Granular solids, liquids, and gases. *Rev. Mod. Phys.*, 68:1259, 1996.

[48] GDR MiDi. On dense granular flows. *Eur. Phys. J. E*, 1:341, 2004.

[49] R.R. Hartley and R.P. Behringer. Logarithmic rate dependence of force networks in sheared granular materials. *Nature*, 421:928, 2003.

[50] T. Unger, J. Török, J. Kertész, and D. E. Wolf. Shear band formation in granular media as a variational problem. *Phys. Rev. Lett.*, 92:214301, 2004.

[51] T. S. Komatsu, S. Inagaki, N. Nakagawa, and S. Nasuno. Creep motion in a granular pile exhibiting steady surface flow. *Phys. Rev. Lett.*, 86:1757, 2001.

[52] L. Bocquet, W. Losert, D. Schalk, T. C. Lubensky, and J. P. Gollub. Granular shear flow dynamics and forces: Experiment and continuum theory. *Phys. Rev. E*, 65:011307, 2001.

[53] J. Crassous, J.-F. Metayer, P. Richard, and C. Laroche. Experimental study of a creeping granular flow at very low velocity. *J. Stat.*, P03009, 2008.

[54] R. Gutfraind and O. Pouliquen. Molecular dynamic simulations of quasi-static vertical chute flows. *Mech Materials*, 24:273, 1996.

[55] A. L. Bocquet, Colin and A. Ajdari. Kinetic theory of plastic flow in soft glassy materials. *Phys. Rev. Lett.*, 103:036001, 2009.

[56] J. Goyon, A. Colin, G. Ovarlez, A. Ajdari, and L. Bocquet. Spatial cooperativity in soft glassy flows. *Nature*, 454:84, 2008.

[57] A. Ries, D. E. Wolf, and T. Unger. Shear zones in granular media: Three-dimensional contact dynamics simulation. *Phys. Rev. E*, 76:051301, 2007.

[58] W.N. Man, A. Donev, F.H. Stillinger, M.T. Sullivan, W.B. Russel, D. Heeger, S. Inati, S. Torquato, and P.M. Chaikin. Experiments on random packings of ellipsoids. *Phys. Rev. Lett.*, 94:198001, 2005.

[59] D.A. Huerta, V. Sosa, M.C. Vargas, and J.C. Ruiz-Suárez. Archimedes' principle in fluidized granular systems. *Phys. Rev. E*, 72:031307, 2005.

[60] K. A. Reddy, Y. Forterre, and O. Pouliquen. Evidence of mechanically activated processes in slow granular flows. *Phys. Rev. Lett.*, 106(10):108301, 2011.

[61] E. Nowak, J. Knight, E. Ben-Naim, H. Jaeger, and S. Nagel. Density fluctuations in vibrated granular materials. *Phys. Rev. E*, 57:1971–1982, 1998.

[62] M. D. Ediger. Spatially heterogenous dynamics in supercooled liquids. *Molecules*, pages 99–128, 2000.

[63] G. E. Uhlenbeck and L. S. Ornstein. On the theory of the brownian motion. *Phys. Rev.*, 36:823, 1930.

[64] J.A. Dijksman, E. Wandersman, S. Slotterback, C.R. Berardi, W.D. Updegraff, M. van Hecke, and W. Losert. From frictional to viscous behavior: Three-dimensional imaging and rheology of gravitational suspensions. *Phys. Rev. E*, 82:060301, 2010.

[65] M. Toiya, J. Stambaugh, and W. Losert. Transient and Oscillatory Granular Shear Flow. *Phys. Rev. Lett.*, 93:088001, 2004.

[66] P. Richard, M. Nicodemi, R. Delannay, P. Ribière, and D. Bideau. Slow relaxation and compaction of granular systems. *Nature Materials*, 4:121, 2005.

[67] T. Hatano and S.-I. Sasa. Steady-State Thermodynamics of Langevin Systems. *Phys. Rev. Lett.*, 86:3463, 2001.

[68] I. Goldhirsch. Rapid granular flows. *Annu. Rev. Fluid Mech.*, 35:267, 2003.

[69] J. T. Jenkins and M.W. Richman. Kinetic theory for plane flows of a dense gas of identical, rough, inelastic, circular disks. *Physics of Fluids*, 28:3485, 1985.

[70] C.K.K. Lun. Kinetic theory for granular flow of dense, slightly inelastic, slightly rough spheres. *J. Fluid Mech.*, 233:539, 1991.

[71] K. Feitosa and N. Menon. Breakdown of Energy Equipartition in a 2D Binary Vibrated Granular Gas. *Phys. Rev. Lett.*, 88:198301, 2002.

[72] R. Wildman and D. Parker. Coexistence of Two Granular Temperatures in Binary Vibrofluidized Beds. *Phys. Rev. Lett.*, 88:064301, 2002.

[73] G. Baxter and J. Olafsen. Experimental Evidence for Molecular Chaos in Granular Gases. *Phys. Rev. Lett.*, 99:028001, 2007.

[74] N. Brilliantov, T. Pöschel, W. Kranz, and A. Zippelius. Translations and Rotations Are Correlated in Granular Gases. *Phys. Rev. Lett.*, 98:128001, 2007.

[75] Y. Shokef, G. Bunin, and D. Levine. Fluctuation-dissipation relations in driven dissipative systems. *Phys. Rev. E*, 73:046132, 2006.

[76] I. Ono, C. O'Hern, D. Durian, S. Langer, A. Liu, and S. Nagel. Effective Temperatures of a Driven System Near Jamming. *Phys. Rev. Lett.*, 89:095703, 2002.

[77] A.R. Abate and D.J. Durian. Effective Temperatures and Activated Dynamics for a Two-Dimensional Air-Driven Granular System on Two Approaches to Jamming. *Phys. Rev. Lett.*, 101:245701, 2008.

[78] S. McNamara and S. Luding. Energy nonequipartition in systems of inelastic, rough spheres. *Phys. Rev. E*, 58:2247, 1998.

[79] O. Herbst, R. Cafiero, A. Zippelius, Hans J. Herrmann, and S. Luding. A driven two-dimensional granular gas with Coulomb friction. *Physics of Fluids*, 17:107102, 2005.

[80] T. Harada and K. Yoshikawa. Fluctuation-response relation in a rocking ratchet. *Phys. Rev. E*, 69:031113, 2004.

[81] E. Ben-Naim and J. Machta. Stationary States and Energy Cascades in Inelastic Gases. *PRL*, 94:138001, 2005.

[82] W. Kang, J. Machta, and E. Ben-Naim. Granular gases under extreme driving. *Europhys. Lett.*, 91:34002, 2010.

[83] R.A. Ingale and M.D. Shattuck. First-order phase transition and the equation of state in a 2d granular fluid. in preparation.

[84] F. Lechenault and K.E. Daniels. Equilibration of granular subsystems. *Soft Matter*, 6:3074, 2010.

[85] J. Puckett, F. Lechenault, and K.E. Daniels. Local origins of volume fraction fluctuations in dense granular materials. *Phys. Rev. E*, 83:041301, 2011.

[86] A.J. Liu and S.R. Nagel. The jamming transition and the marginally jammed solid. *Annu. Rev. Condensed Matter Physics*, page 347, 2010.

[87] M. van Hecke. Jamming of Soft Particles: Geometry, Mechanics, Scaling and Isostaticity. *J. Phys.: Condens. Matter*, 22:33101, 2010.

[88] H.T. Xu, A.P. Reeves, and M.Y. Louge. Measurement Errors In The Mean And Fluctuation Velocities Of Spherical Grains From A Computer Analysis Of Digital Images. *Review Of Scientific Instruments*, 75:811, 2004.

[89] P. Melby, A. Prevost, D.A. Egolf, and J.S. Urbach. Depletion force in a bidisperse granular layer. *Phys. Rev. E*, 76:051307, 2007.

[90] S. Luding. Global equation of state of two-dimensional hard sphere systems. *Phys. Rev. E*, 63:042201, 2001.

[91] R. Kubo. The fluctuation-dissipation theorem. *Rep. Prog. Phys.*, 29:255, 1966.

[92] J. Brey and M. Ruiz-Montero. Velocity distribution of fluidized granular gases in the presence of gravity. *Phys. Rev. E*, 67:021307, 2003.

[93] V. Garzó and J. Dufty. Homogeneous cooling state for a granular mixture. *Phys. Rev. E*, 60:5706, 1999.

[94] K. Feitosa, H. Wang, and N. Menon. Rotational dynamics in a 2D vibrated granular gas. *(preprint)*, 2011.

Summary

Consider an enormous jar of marbles: the particles behave like a solid and support the weight of an object placed on top of them. However, if the container is tilted, the marbles pour out as if they were a liquid. But how much does the container need to be tilted before the particles will flow? This is a difficult problem because there are many particles in the container and they are *disordered*: unlike an ordered crystal, the behaviour of the entire system cannot be understood by examining the behaviour of only a few of the marbles.

The universe is full of disordered many-body systems: window glass, shaving foam and the rings of Saturn are all agglomerations of similar particles which interact with each other according to well-known physical laws. Granular materials are a special type of many-body system: rocks on a scree slope, sand, rice and coffee are all made up of hard particles which repel each other when they come into contact. As was the case with the marbles, the *collective* behaviour of these materials cannot be derived simply from a description of the interaction between two particles. Instead, the problem of describing the properties of many-body systems can often be approached with statistical mechanics, which utilizes a *statistical* description of the motion of large numbers of particles in order to calculate the bulk properties of the system.

Statistical mechanics is very good at describing ordinary gases: from a few logical assumptions about how the particles move it is possible to derive how the temperature, pressure and volume of a gas are related. But can we also use statistical mechanics to describe the behaviour of a jar of marbles? The differences between gas molecules and marbles are simple to understand: marbles lose energy when they collide or slide past one another, so unless energy is supplied, a collection of marbles will quickly come to rest. Meanwhile, colliding gas molecules conserve energy when they collide and they will continue to tumble around indefinitely. This difference has a crucial consequence: because ordinary statistical mechanics relies on energy conservation, it cannot be used to describe granular materials without modifications.

But are there circumstances where a marble can behave just like a big air molecule? Can a system made of glass beads behave like a real liquid or gas? By studying the properties of granular materials we hope to gain insights into the fundamental characteristics of disordered many-body systems.

In this Thesis we have examined two experimental granular many-body systems. The first system is a container of glass beads which are agitated by a disk which rotates in the bottom of the vessel. When the disk is stationary the grains behave like a solid, but when the disk begins rotating the grains behave collectively as though they are a liquid. In Chapter 2 we measure the position of a hollow cylindrical object as it sinks into the grains: if the probe is not too heavy it will float at the depth predicted by Archimedes' Rule. We also find that as the probe sinks, the net force on the probe is proportional to the velocity of the probe - the probe behaves as if it were sinking in a viscous liquid. The viscosity remains fairly uniform throughout the system, which indicates that the flow of grains near the probe is not the primary cause of the fluid-like behaviour of the system. However, we also find that the viscosity of our sheared granular system is inversely proportional to the square of the pressure exerted by the probe, whereas in a real liquid the viscosity is independent of the dimensions and mass of the sinking object.

But what causes the liquid-like behaviour of our sheared grains? In Chapter 3, we examine fluctuations in the trajectory of a floating probe. This measurement is essentially a much larger version of another experiment in which the motion of a grain of pollen in water is observed through a microscope. Einstein realized that the tiny jiggling motions of the pollen were due to collisions with water molecules. Moreover, he realized that it was possible to describe the size of the fluctuations of the pollen particle in terms of the temperature and viscosity of the liquid. The fluctuations of the hollow cylinder floating in our 1 mm grains are also similar to this Brownian motion: the mean square displacement of the probe at long times exhibits a plateau similar to that exhibited by the motion of random walk in a potential well. However, the fluctuations on shorter time scales are *subdiffusive*: the probe does not travel as far in the grains as it would in a real liquid. Moreover, the fluctuations become more subdiffusive in character as the height of the grains in the container is increased, which means that it is not possible to define a "temperature" for the system using

the fluctuations of the floating probe.

Since stationary grains behave like a solid and continuously sheared grains behave like a liquid, there must be a transition from liquid-like to solid-like behaviour as the disk rotates a small amount. In Chapter 4, we probe the behaviour of the grains when the disk is rotated back and forth. We find that when the disk reverses direction there is a brief period during which the grains rapidly compact before they begin to slowly dilate again. This process of expansion and dilation causes the system to compact in the same manner as a tapped or shaken granular system. We also find that the motion of a cylindrical probe sinking in the system is more complicated than that of a simple liquid; driving the grains by rotating the disk produces a system which is neither a liquid nor a solid.

Finally, in Chapter 5, we describe another experiment consisting of 150 petri dishes which float on an air hockey table just like air hockey pucks. The petri dishes are kicked by bumpers along the edge of the table and we use a high speed camera to track both the rotational and translational motion of the particles. We use a combination of large and small petri dishes so that we can test whether the petri dishes behave like a collection of large and small air molecules. Because we can measure the velocities of all the particles, we can compare the velocity distributions to those of the particles in a real gas. Unlike a real gas, the distributions of the translational velocity are the same for both large and small particles, which means that they have different "temperatures". Meanwhile, the distributions of the rotational velocities of the large and small particles grow with the inverse of the particle radii, indicating that the particles would rather roll against their neighbours than slide.

One important property of real gases is that the amount of energy contributed by motion in each of the three planes and around each rotational axis of the molecule is the same. Our petri dishes can move in two perpendicular directions and can rotate around the axis perpendicular to the air hockey table. Although many other experiments on granular systems indicate that the energy in each degree of freedom is *not* the same, we find that the petri dishes in our experiment are able to behave more like real air particles and divide their energies equally between each of the three degrees of freedom. We show that the system is able to do this *and* preserve the preference for rolling contacts because the motion is restricted to two dimensions. Finally, we are able to describe the pressure, the area

enclosed by the particles and the total energy of the particles using the van der Waals equation - the same equation that relates these properties in an ideal gas.

Both the behaviour of the petri dishes and the behaviour of the glass beads excited by a spinning disk illustrate the utility and the limitations of using statistical mechanics to describe granular systems. We have demonstrated that granular materials can have the bulk properties of a liquid or a gas. In addition, granular systems can exhibit fluctuations which are similar to the Brownian motion of particles in a real gas, even though the microscopic origins of the fluid-like behaviour are not the same as those in a real molecular fluid.

Samenvatting

Denk aan een grote pot met knikkers: de deeltjes gedragen zich als vaste stof en dragen het gewicht van een voorwerp als het erbovenop neergezet wordt. Evenwel, als de houder gekanteld is, gaan de knikkers stromen alsof ze een vloeistof zijn. Maar onder welke hoek moet de houder gekanteld worden voordat de knikkers vloeien? Deze vraag is moeilijk want er zijn heel veel deeltjes en ze zijn *wanordelijk*: in tegenstelling tot een geordend kristal, kan het gedrag van het hele systeem niet begrepen worden door alleen het gedrag van een paar van de knikkers te bekijken.

Het heelal staat vol van wanordelijke veeldeeltjessystemen: glas, scheerschuim en de ringen van Saturnus zijn alle agglomeraties van soortgelijke deeltjes die met elkaar wisselwerken op basis van bekende natuurkundige wetten. Granulaire materialen zijn een speciaal type van veeldeeltjessysteem: rotsen op een helling puin, zand, rijst en koffie zijn allemaal gemaakt van harde deeltjes die elkaar afstoten als ze in contact komen. Net als met de knikkers, kan het *collectieve* gedrag van deze materialen niet zomaar worden afgeleid uit een beschrijving van de interactie tussen twee deeltjes. In plaats hiervan kan het probleem van de beschrijving van de eigenschappen van een veeldeeltjessysteem vaak worden benaderd met statistische fysica: die maakt gebruik van een *statistische* beschrijving van de beweging van grote aantallen deeltjes om de globale eigenschappen van het systeem te berekenen.

Statistische fysica is erg goed in het beschrijven van gewone gassen: van een paar logische aannames over hoe de deeltjes bewegen, wordt afgeleid hoe de temperatuur, druk en volume van een gas gerelateerd zijn. Maar kunnen we ook gebruik maken van statistische fysica om het gedrag van een pot knikkers te beschrijven? De verschillen tussen gasmoleculen en knikkers zijn eenvoudig te begrijpen: knikkers verliezen energie als ze met elkaar botsen of langs elkaar schuiven, dus tenzij energie wordt toegevoegd, komt een verzameling knikkers snel tot rust. Bij botsende gasmoleculen geldt echter energiebehoud en de moleculen zullen dan ook oneindig lang rond blijven stuiteren. Dit verschil heeft een essentieel gevolg: omdat de gewone statistische fysica is gebaseerd op energiebehoud

kan zij niet zonder wijziging gebruikt worden om granulaire stoffen te beschrijven.

Maar zijn er omstandigheden waarin een knikker zich gedraagt net als een luchtmolecuul? Kan een systeem gemaakt van glazen kralen zich gedragen als een echte vloeistof of gas? Door het bestuderen van de eigenschappen van granulaire materialen hopen we inzicht te verwerven in de fundamentele kenmerken van wanordelijke veeldeeltjessystemen.

In dit proefschrift hebben we twee experimentele granulaire veeldeeltjessystemen onderzocht. Het eerste systeem is een bak gevuld met glazen kralen die zachtjes in beweging worden gebracht (gesheared) door een schijf die draait op de bodem van de bak. Als de schijf stilstaat, gedragen de korrels zich als vaste stof, maar als de schijf begint met draaien gedragen de korrels zich collectief alsof ze een vloeistof zijn. In Hoofdstuk 2 meten we de positie van een hol cilindervormig voorwerp terwijl het in de container zinkt: als de sonde niet te zwaar is, zal zij gaan drijven op de diepte die voorspeld wordt door de regel van Archimedes. We ontdekken ook dat de netto kracht op de sonde evenredig is aan de snelheid van de sonde — de sonde gedraagt zich alsof zij in een viskeuze vloeistof zinkt. Tenslotte blijft de viscositeit vrij uniform door het hele systeem; dit betekent dat de stroom van korrels in de buurt van de sonde niet de primaire oorzaak is van het vloeistof-achtige gedrag van het systeem. We ontdekken ook dat de viscositeit van ons geshearede granulaire systeem evenredig is met het kwadraat van de druk van de sonde, terwijl in een echte vloeistof de viscositeit onafhankelijk is van de afmetingen en massa van het zinkende voorwerp.

Maar wat is de oorzaak van het vloeistof-achtige gedrag van onze geshearede korrels? In Hoofdstuk 3 onderzoeken we fluctuaties in de positie van een drijvende sonde. Deze meting is in wezen een veel grotere versie van een experiment van Brown, waarin de beweging van een stuifmeelkorreltje in water wordt waargenomen door een microscoop. Einstein realiseerde zich dat de kleine dansbewegingen van de pollen waren te wijten aan botsingen met watermoleculen. Bovendien besefte hij dat het mogelijk was om de grootte van de fluctuaties van het stuifmeelkorrel te beschrijven in termen van de temperatuur en de viscositeit van de vloeistof. De schommelingen van de holle cilinder die in onze 1 mm grote korrels drijft lijken ook op deze Brownse beweging: de gemiddelde kwadratische verplaatsing van de sonde na lange tijden vertoont een plateau soortgelijk aan

die tentoongespreid door een toevalsbeweging in een potentiaalput. Echter, de schommelingen op kortere tijdschalen zijn *subdiffusief*: de sonde reist niet zo ver in de korrels als wanneer hij in een echte vloeistof zou reizen. Bovendien krijgen de fluctuaties een meer subdiffusief karakter als de hoogte van de laag korrels in de container wordt vergroot, wat betekent dat het niet mogelijk is om een "temperatuur" van het systeem te definiëren door de fluctuaties van de de drijvende sonde.

Aangezien stilstaande korrels zich gedragen als een vaste stof en continu geshearede korrels zich als een vloeistof gedragen, moet er een overgang van vloeibaar-achtig tot vast-achtig gedrag zijn als de schijf een klein beetje draait. In Hoofdstuk 4 onderzoeken we het gedrag van de korrels als de schijf heen en weer wordt geroteerd. Wij ontdekken dat als de schijf van draairichting verandert, er een korte periode is waarin de korrels snel dichter op elkaar pakken (compactie) voordat ze beginnen met langzaamaan weer losser te pakken. Dit proces van expansie en dilatie zorgt ervoor dat het systeem compacteert op dezelfde wijze als in een granulair systeem dat geschud wordt of waarop getikt wordt. We ontdekken ook dat de beweging van een cilinder die in dit systeem zinkt complexer is dan in een eenvoudige vloeistof: het aandrijven van de korrels door het draaien van de schijf produceert een systeem dat noch vloeistof noch vaste stof is.

In Hoofdstuk 5 tenslotte, beschrijven we een ander experiment, bestaande uit 150 petrischalen die op een luchtkussentafel drijven. De petrischalen worden aangedreven door zuigers die langs de rand van de tafel gemonteerd zijn en we gebruiken een hogesnelheidscamera om zowel de rotatie- als de translatiebeweging van de deeltjes te berekenen. We gebruiken een combinatie van grote en kleine petrischaaltjes, zodat we kunnen kijken of de petrischalen zich gedragen als een verzameling van grote en kleine luchtmoleculen. Aangezien we de snelheden van alle deeltjes kunnen meten, kunnen we hun snelheidsverdeling vergelijken met de snelheidsverdeling van de deeltjes in een echt gas. In tegenstelling tot in een echt gas, zijn de verdelingen van de translatiesnelheid hetzelfde voor zowel grote als kleine petrischaaltjes, wat betekent dat zij verschillende "temperaturen" hebben. Ondertussen groeien de verdelingen van de rotatiesnelheden van de grote en kleine deeltjes met de inverse van de straal van de deeltjes, wat aangeeft dat de deeltjes liever willen rollen langs hun buren dan schuiven.

Een belangrijke eigenschap van echte gassen is dat de hoeveelheid

energie die wordt bijgedragen door beweging in elk van de drie mogelijke richtingen en rond elke rotatie-as van het molecuul hetzelfde is. Onze petrischalen kunnen in twee loodrechte richtingen bewegen en en kunnen draaien rond de as loodrecht op de luchtkussentafel. Hoewel vele andere experimenten met granulaire systemen aangeven dat de energie niet hetzelfde is voor elke vrijheidsgraad, ontdekken we dat het gedrag van de petrischalen in ons experiment meer op het gedrag van luchtdeeltjes lijkt; ze verdelen hun energie gelijkelijk tussen elk van de drie vrijheidsgraden. We laten zien dat het systeem in staat is om dit te doen *en tegelijkertijd* de voorkeur voor rollende contacten te behouden; we laten ook zien dat dit gebeurt omdat de beweging beperkt is tot twee dimensies. Ten slotte kunnen we de druk, het gebied omsloten door de deeltjes en de totale energie van de deeltjes beschrijven met behulp van de Van der Waals vergelijking — dezelfde vergelijking die deze eigenschappen in een ideaal gas aan elkaar relateert.

Zowel het gedrag van de petrischalen als het gedrag van de door de draaiende schijf geagiteerde glaskogels illustreren het nut en de beperkingen van het gebruik van statistische fysica om granulaire systemen te beschrijven. We hebben aangetoond dat granulaire materialen de eigenschappen van een vloeistof of een gas kunnen hebben. Bovendien kunnen granulaire systemen fluctuaties vertonen die vergelijkbaar zijn met de Brownse beweging van deeltjes in een echt gas, ook al is de microscopische oorsprong van het vloeistof-achtig gedrag niet hetzelfde is als die in een echte moleculaire vloeistof.

Hulp met vertaling: Gijs Katgert

Publication List

[1] *Fluctuations in an agitated granular fluid*,
Kiri Nichol, Martin van Hecke (in preparation).

[2] *Equipartition of rotational and translational energy in a dense granular gas*,
Kiri Nichol, Karen E. Daniels (in preparation).

[3] *Flow-Induced Agitations Create a Granular Fluid*,
Phys. Rev. Lett. 104, 078302 (2010),
Kiri Nichol, Alexey Zanin, Renaud Bastien, Elie Wandersman
and Martin van Hecke.

[4] *The Coefficient of Restitution for Bouncing Nanoparticles*,
Phys. Rev. B. 81, 195422 (2010) A. I. Ayesh, S. A. Brown,
A. Awasthi, S. C. Hendy, P. Y. Convers, and K. Nichol.

[5] *Range straggling of low energy ^{8}Li+ in thin metallic films using β-NMR*,
Physica B: Condensed Matter, Volume 326, Issues 1-4,
February 2003, 205-208,
T. R. Beals, R. F. Kiefl, W. A. MacFarlane, K. M. Nichol, G. D. Morris,
C. D. P. Levy, S. R. Kreitzman, R. Poutissou, S. Daviel,
R. A. Baartman and K. H. Chow.

Curriculum Vitae

I was born on June 4, 1981 in Calgary, Alberta, Canada. After completing my secondary schooling at Sir Winston Churchill High School, I moved to Vancouver and began studies at the University of British Columbia. I spent summers working in the Structured Surface Physics Lab at UBC, the β-NMR Group at TRIUMF and the Subatomic Physics Group at the University of Regina. My Honours Thesis, *Local currents on novel lattice geometries under the Hubbard Model*, was completed under the supervision of Dr. Mona Berciu and I received a B.Sc. in Honours Physics with a minor in English Literature in 2004.

I moved to McMaster University in Hamilton, Ontario for an M.Sc. in condensed matter theory. My thesis, *Relaxation of a two-level system coupled to a fullerene molecule*, was completed in 2006. I subsequently spent a year travelling and working as a "Pre-Doc" in Simon Brown's Nanoscale Devices group at the University of Canterbury in Christchurch, New Zealand.

In 2007, I began a Ph.D. in the Granular & Disordered Media group of Martin van Hecke. During my Ph.D. I worked as a teaching assistant for courses in Labview and Statistical Mechanics. I also attended schools in Enschede, Leuven (Belgium) and Cargese (France) and I had the opportunity to present my research at meetings of the American Physical Society (2008, 2010, 2011), the Canadian Association of Physicists (2010) and the Gordon conferences on Granular Materials (2008, 2010). Part of my Ph.D. research was conducted in the group of Karen Daniels at North Carolina State University.

Acknowledgements

> "If we do not live where we work and when we work, we are wasting our lives and our work too." — Wendell Berry

The scientific content of my thesis owes much to conversations with Brian Tighe, Elie Wandersman and Karen Daniels and I would like to thank them for the thoughtful comments they have shared with me over the course of the last four years. I would like to further thank my fellow promovendi, Joshua Dijksman, Gijs Katgert, Alex Siemens and Geert Wortel, for sharing their scientific enthusiasm, their technical expertise and the gezelligheid in the lab. I would also like to thank Jeroen Mesman for building my experimental setup, Fred Kranenburg for keeping the computers running and Danielle Duijn for making all the forms manageable.

During the last year of my PhD I spent three months visiting the lab of Karen Daniels at NC State. My time there was extremely productive and enjoyable and I would like to thank Karen, James Puckett, Eli Owens, Adam Keith, Carlos Ortiz and Frederic Lechenault for their generous technical assistance and hospitality.

I would also like to thank the other members of my group in Leiden for their thoughtful contributions to group meetings and seminars. I am particularly indebted to Brian Tighe, for teaching me all about random walkers in potential wells, and Silke Henkes, for sharing many wonderful late-night discussions.

Finally, I would like to take the formal opportunity to acknowledge the support of my friends from Leiden, Canterbury, McMaster and UBC. I would also like to acknowledge the influence of a few people who encouraged me as I embarked on my PhD: my undergraduate supervisor, Mona Berciu, my friend and officemate, Laura Filion and postdocs Rastko Sknepnek and Jurij Smakov. I would like to thank my parents for having high expectations of me and for giving me a lot of freedom to define my own high expectations. And I would like to thank my teachers, Mrs Martin (Grade 7 & 8 Science) and Mr Wereley (Grade 11 & 12 Physics), to whom I dedicate this thesis.